

Chapter 5

Strain Effects

5.1 Introduction

The strain-optic effect is commercially exploited in both optical physical sensors and telecommunication components. In particular, silica based platforms are widely extolled for such applications as silica demonstrates mechanical strength and a low thermal sensitivity, compared with other optical platforms such as polymers [112].

The applications of optical physical sensors are extensive [113], [21], [114], ranging from large scale structural health monitoring of bridges, oil rigs, skyscrapers etc, to small scale monitoring of micro electromechanical devices [115] [116]. A recent trend for large scale structural health monitoring is the fabrication of smart structures from composite materials, such as glass fibre [117] and carbon fibre [118]. These composites integrate fibre Bragg grating waveguides into a planar structure. The work reported in this chapter examines, for the first time, the strain response of UV written Bragg gratings in a composite silica-on-silicon platform. As with smart structures, the developed devices have the potential to map stress profiles in a plane, whilst exhibiting the benefits of a silica based platform. The theoretical understanding developed in this chapter shall be further extended in Chapter 6 where thin silica membranes are investigated for 'small scale' physical sensor applications.

Strain actuation of Bragg gratings is also commercially implemented in the telecommunication industry. Bragg grating filters combine the advantages of a narrow bandwidth, low crosstalk, and the option of a flat-top passband. They are both ef-

fective filters and can display significant levels of mechanical actuation [119] [120] [121]. The silica-on-silicon platform used in this work are an appropriate platform for Bragg grating actuation as it is an established composite platform for optical telecommunication components.

This chapter is structured such to firstly give an overview of continuum mechanics, examining strain in an arbitrary body. From this understanding the theoretical response of a Bragg grating subject to strain shall be formulated. The grating response of two bending geometries and a lateral compression geometry shall be examined and their potential application for physical and telecomm devices investigated.

5.2 Continuum Mechanics

This section is intended to refresh the reader with the theory and notation of continuum mechanics, which relates to the physical properties of the bulk material. In continuum mechanics we have infinite material boundary conditions meaning we do not concern ourselves with the complications of edge effects.

Stress and strain are the prerequisite to analyse structurally the silica-on-silicon chip. So firstly the stress tensor will be introduced, followed by the strain tensor. Finally the relationship between stress and strain will be developed.

5.2.1 The Stress Tensor

Stress is defined as a distributed force on an internal or external area of a body. The forces involved to induce stress are either externally applied and/or a result of temperature change.

To illustrate the concept of stress consider a point P within a general solid body, as in Figure 5.1. The body has a set of external forces \mathbf{F} which act upon it. To expose point P an arbitrary slice through the body would need to be made which intersects P . The orientation of the slice is arbitrary but for convenience we shall consider it to be the slice that is normal to the x_1 axis. Now, the forces on P can be resolved into three axial components, illustrated in Figure 5.2. Stress is a point

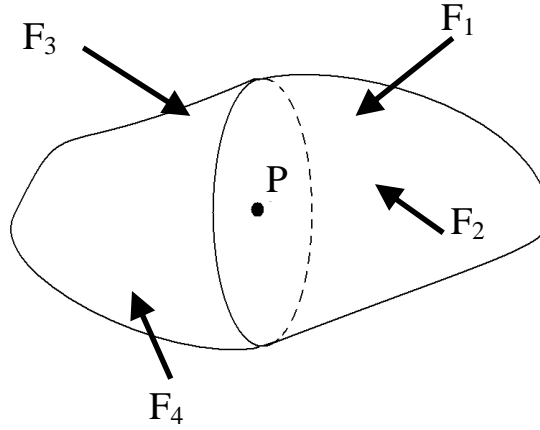


Figure 5.1: Continuous body with external forces applied

function, so we shall reduce the area considered to be infinitesimally small.

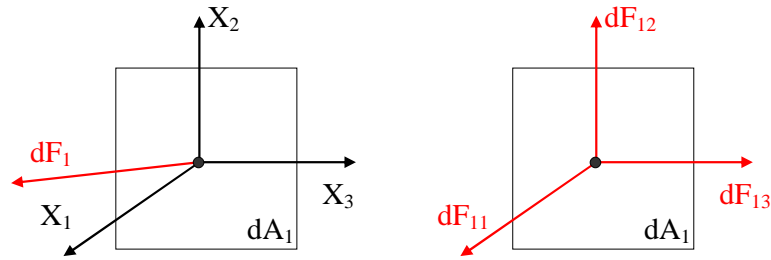


Figure 5.2: Considering stress on a point

The stress in the x_1 direction can be formulated as [122]

$$\sigma_{11} = \frac{dF_{11}}{dA_1} \quad (5.1)$$

As this stress is normal to the area it is labelled as the normal stress. Stresses also arise from the tangential forces. As these forces are parallel to the area considered they are a rubbing (sliding) force, which is labelled as shear and formulated as [122]

$$\tau_{ij} = \frac{dF_{ij}}{dA_i} \quad (5.2)$$

It is apparent that an infinite variety of conditions, corresponding to an infinite number of slice areas exist for any given finite point in a body. Fortunately, we

do not need to formulate them all! As a coordinate transform action can be undertaken only three principle coordinates are required. For simplicity the surfaces chosen shall be perpendicular to each other, meaning the stress can be written in a matrix form. To illustrate the tensor nature of stress present at point P in the continuous body, a cubic element will be considered, as illustrated in Figure 5.3

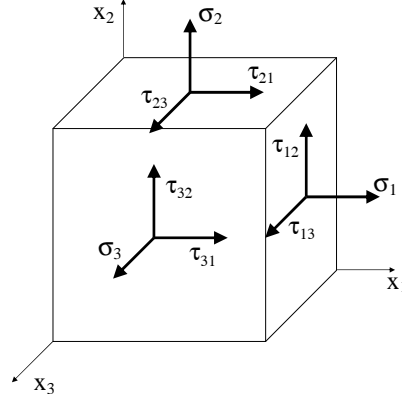


Figure 5.3: An infinitesimal cubic element located within a continuous body undergoing nine components of stress

Now, a stress vector \mathbf{T}_1 can be considered acting on the plane normal to the \mathbf{x}_1 direction. For simplification we shall use the contracted notation $\sigma_{ii} = \sigma_i$

$$\mathbf{T}_i = \sigma_1 \cdot \mathbf{x}_1 + \tau_{12} \cdot \mathbf{x}_2 + \tau_{13} \cdot \mathbf{x}_3 \quad (5.3)$$

The stress vector \mathbf{T}_1 is the ratio of force acting on a surface. Expanding this idea for a volume wrapped around a point illustrated in Figure 5.3 the stress tensor of that volume is defined by nine stress components acting on the three surfaces of the cube, making up three stress vectors.

$$\sigma_{ij} = \begin{bmatrix} \sigma_1 & \tau_{12} & \tau_{13} \\ \tau_{21} & \sigma_2 & \tau_{23} \\ \tau_{31} & \tau_{32} & \sigma_3 \end{bmatrix} \quad (5.4)$$

5.2.2 The Strain Tensor

The application of stress to a body in equilibrium causes it to undergo deformation and/or motion. The measure of deformation is labelled strain, ϵ . As with stress two types of strain exist, normal and shear. Normal strain is the ratio of length change, δu , of the stressed element in a direction parallel to the normal stress, formulated as [122]

$$\epsilon_i = \frac{\partial \mathbf{u}_i}{\partial \mathbf{x}_i} \quad (5.5)$$

Shear strain is a measure of the distortion of the stressed element, formulated as [122]

$$\epsilon_{ij} = \epsilon_{ji} = \frac{1}{2} \left(\frac{\partial \mathbf{u}_i}{\partial \mathbf{x}_j} + \frac{\partial \mathbf{u}_j}{\partial \mathbf{x}_i} \right) \quad (5.6)$$

A three-dimensional body undergoing normal and shear strain as a result of external force is illustrated in Figures 5.4 (a) and (b) respectively.

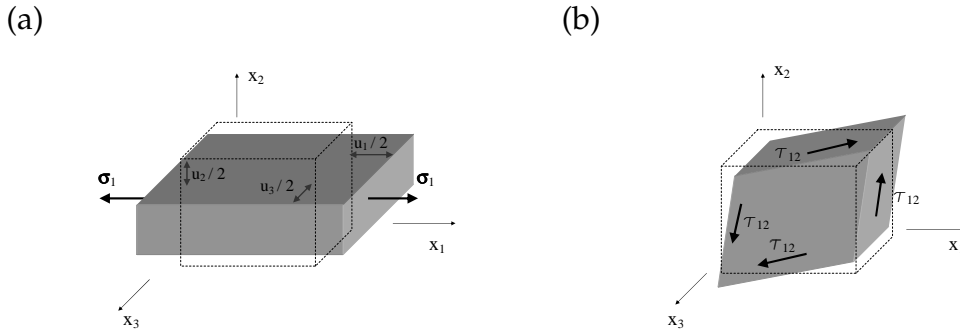


Figure 5.4: (a) Normal strain as a result of normal stress and (b) Shear strain as a result of shear stress

Figure 5.4 (a) depicts that a tensile stress in the \mathbf{x}_1 direction results in a tensile strain in the \mathbf{x}_1 direction. In addition to this there is a compressive strain in the \mathbf{x}_2 and \mathbf{x}_3 directions respectively. The ratio of strains normal \mathbf{x}_i and perpendicular \mathbf{x}_j to the applied force is labelled the Poisson ratio, ν_{ij} , expressed as

$$\nu_{ij} = -\frac{\epsilon_j}{\epsilon_i} \quad (5.7)$$

There exists an interrelation between stress and strain that is dependent upon the type of material examined.

5.2.3 Stress and Strain Relationships

Bodies of different material but of the same dimensions and under the same forces usually deform differently. For treatment in this thesis we shall consider the stress to strain relationship in the elastic region, which can be thought of as 'memory' during deformation, such that when the stress is removed the body returns to its original shape prior to the applied stress. Considering this on a microscopic scale the bonds are stretching but do not break or make new bonds. In this elastic regime stress and strain can be related, by Hooke's law, which states the stress tensor is linearly proportional to the strain tensor, formulated as¹

$$\epsilon_{ij} = -s_{ijkl}\sigma_{kl} \quad (5.8)$$

s_{ijkl} is known as the elastic compliance tensor [106] and is required to be a fourth rank tensor of $3^4=81$ elements. However, as a result of the shear stress and shear strain definitions (namely $\sigma_{ij}=\sigma_{ji}$ and $\epsilon_{ij}=\epsilon_{ji}$) this reduces to a tensor of only 36 elements [106]. With this symmetry it is custom to contract the notation, such that $\sigma_{11}=\sigma_1$, $\sigma_{22}=\sigma_2$, $\sigma_{33}=\sigma_3$, $\sigma_{12}=\sigma_4$, $\sigma_{13}=\sigma_5$, $\sigma_{23}=\sigma_6$ and similarly for ϵ . The corresponding compliance tensor is thus contracted to s_{mn} , containing $6^2=36$ elements.

The devices considered in this thesis form a silica-on-silicon composite, with silica and silicon individually having different compliance tensors, which need to be married together to gain an understanding of the mechanical properties of the whole device.

5.3 Mechanical Properties of Silica-on-Silicon

Silica-on-silicon is an example of a composite, as it forms a single bulk composing of two separate materials that are not blended. As the silica and silicon form

¹Note that the sign convention in Equation 5.8 arise due to the way Pockels defines stress and strain. Compressive stress is considered positive and compressive strain is considered negative.

layered sheets it is categorised as a laminate composite [123]. To understand the mechanical behaviour of the laminate we must firstly define the mechanical properties of its composing parts.

5.3.1 Mechanical Properties of Silicon

The structure and mechanical properties of silicon is well documented due to its importance in the semiconductor industry and widespread use in Microelectromechanical systems (MEMS). As a result of its crystal properties, silicon is mechanically anisotropic and silicon wafers are classified in terms of their crystallographic orientation [124]. The silicon wafers used in this work are p-type (111) wafers², the crystallographic orientation of which is illustrated in Figure 5.5. The (111) silicon wafer is considered the most useful for mechanical devices, especially for MEMS applications, as the mechanical properties of the wafer in the transverse plane are equal. This means that these devices will be least sensitive to their orientation allowing greater fabrication tolerance.

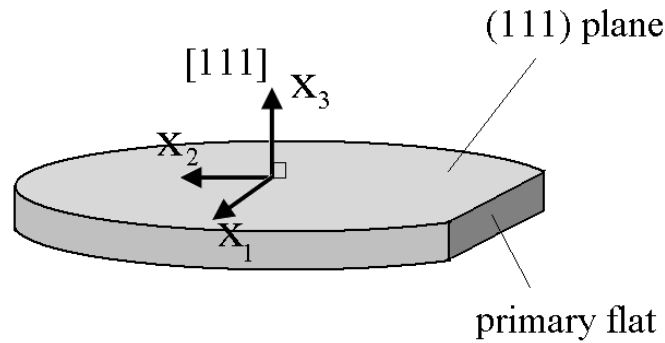


Figure 5.5: Schematic of silicon crystal planes with respect to the wafer geometry

The mechanical properties of silicon vary as a result of its inherent anisotropy. The compliance tensor of silicon is [126].

²(111) is Miller index notation [125] for a plane perpendicular to the [111] crystallographic vector

$$s_{i,j} = \begin{pmatrix} s_{11} & s_{12} & s_{12} & 0 & 0 & 0 \\ s_{12} & s_{11} & s_{12} & 0 & 0 & 0 \\ s_{12} & s_{12} & s_{11} & 0 & 0 & 0 \\ 0 & 0 & 0 & s_{44} & 0 & 0 \\ 0 & 0 & 0 & 0 & s_{44} & 0 \\ 0 & 0 & 0 & 0 & 0 & s_{44} \end{pmatrix} \quad (5.9)$$

where s_{11} , s_{12} and s_{44} are 7.68×10^{-12} , -2.14×10^{-12} and $12.6 \times 10^{-12} \text{ Pa}^{-1}$ respectively [127].

Although silicon is an anisotropic medium it is sometimes convenient to think of it as an isotropic one. For linear, homogenous, isotropic materials, Hooke's law (Equation 5.8) is simply that the normal strain is directly proportional to the normal stress, given by.

$$\epsilon_i = \frac{1}{E} [\sigma_i - \nu(\sigma_j + \sigma_k)] \quad (5.10)$$

where the material constants E and ν are named the Young's modulus and Poisson ratio. These constants are elements of the compliance tensor that give useful information. The Young's modulus quantifies how much a material will strain along the axis of a given stress, formulated as

$$E_i = \frac{\sigma_i}{\epsilon_i} = \frac{1}{s_{ii}} \quad (5.11)$$

The Poisson's ratio gives information of a materials strain perpendicular to the applied stress (along x_i dimension), formulated as

$$\nu_{ij} = -\frac{\epsilon_j}{\epsilon_i} = -\frac{s_{ij}}{s_{ii}} \quad (5.12)$$

For silicon, Young's modulus can vary from 130.2 GPa to 187.5 GPa and Poisson's ratio can vary from 0.064 to 0.361. For silicon (111), Young's modulus is transversely isotropic at 168.9 GPa and 117.3 GPa perpendicular to the (111) plane. Poisson's ratio has a constant value of 0.262 for directions parallel to the (111) plane and 0.182 for directions perpendicular to it. It must be noted that these moduli need to be interpreted into effective moduli when considering a laminate silica-on-silicon

structure. Such a laminate is conventionally described in the literature as forming a composite beam.

5.3.2 Effective Moduli

The silica-on-silicon laminate has silica and silicon constituent parts, as illustrated in Figure 5.6. It shall be assumed that the deposited silica layers and thermally grown silicon oxide have the same mechanical properties i.e., $E_A = E_C$. It can be seen that the laminate has directionality due to its layered nature and that transversely the composite beam is isotropic, i.e. the Young's modulus is $E_1 = E_2 \neq E_3$ and the Poisson ratio is $\nu_{12} = \nu_{21}$, $\nu_{13} = \nu_{23}$ and $\nu_{31} = \nu_{32}$.

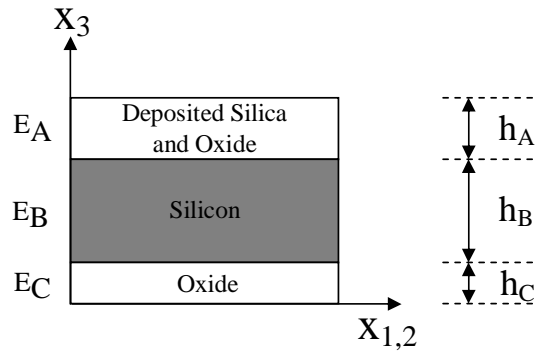


Figure 5.6: The constituent parts in a silica-on-silicon wafer

The effective moduli can be calculated by assuming good adhesion between the silica and silicon layers. Making this assumption for strains parallel to the layers (along the x_1 and x_2 dimensions) must be equal for both silica and silicon, as illustrated in Figure 5.7 (a).

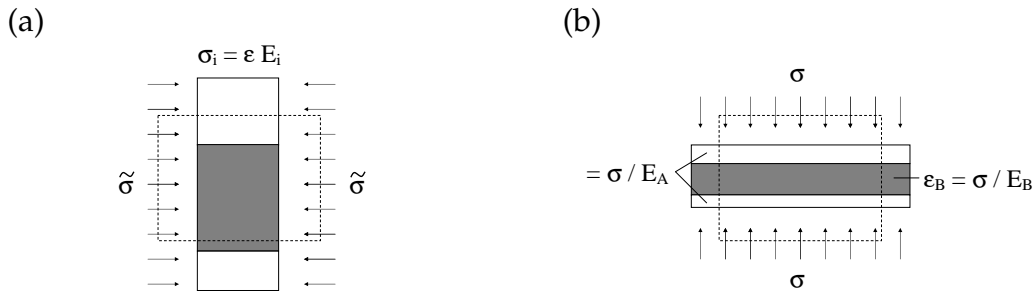


Figure 5.7: A conceptual schematic of the composite laminate under (a) parallel and (b) series deformation

As the silicon and silica have different Young's moduli, each material in this parallel deformation will have a different associated stress. Considering an effective (average) parallel stress $\tilde{\sigma}_{1,2}$, on the device and constant strain, one can infer an effective Young's modulus $E_{1,2}$, formulated as [128]

$$\begin{aligned}\tilde{\sigma}_{1,2} &= E_{1,2}\epsilon_{1,2} \\ \Rightarrow E_{1,2}h\epsilon_{1,2} &= \left(\frac{h_A + h_C}{E_A} + \frac{h_B}{E_B}\right)\epsilon_{1,2} \\ \Rightarrow E_{1,2} &= \frac{1}{h}\left(\frac{h_A + h_C}{E_A} + \frac{h_B}{E_B}\right)\end{aligned}\tag{5.13}$$

where the values of h correspond to the thickness along the x_3 dimension, as previously illustrated in Figure 5.6. This is generally referred to as the rule of mixtures [123].

For lateral compression (strains along the x_3 dimension) the layers are in series, not parallel. Instead of assuming the strains are equal in the different materials we assume they are all different and experience the same stress, the laminate as a whole now experiences an effective strain, $\tilde{\epsilon}_3$, formulated as [123]

$$\begin{aligned}\sigma_3 &= E_3\tilde{\epsilon}_3 = E_3\frac{1}{h}\left(\frac{h_A + h_C}{E_A} + \frac{h_B}{E_B}\right) \\ \Rightarrow E_3 &= \frac{E_A E_B h}{E_A(h_A + h_C) + E_B h_B}\end{aligned}\tag{5.14}$$

Applying rules of mixtures and symmetry arguments the Poisson ratios ν_{ij} for the considered laminate can be analytically determined [123]. Now the mechanical properties of the silica-on-silicon has been outlined we need to understand the effect stress/strain has on a Bragg grating.

5.4 A Bragg Grating's Response to Strain

A Bragg grating's response to strain arises due to both a change in the effective refractive index and pitch of the grating [21] [114], this can be written mathematically as

$$\Delta\lambda_i = 2\left(\Lambda_i\Delta n_i + n_i\Delta\Lambda_i\right) \quad (5.15)$$

The first term in Equation 5.15 relates the effective index change with strain, ϵ , and is dominated by the photoelastic effect. Physical change in core height and width will also change the effective index. However, the contribution of this, in our devices, has been calculated to be negligible. The second term in Equation 5.15 relates to the physical length change of the grating, corresponding to a fractional change in pitch. This section shall address effects in both photoelasticity and fractional change in pitch.

5.4.1 Photoelastic Effects

Photoelasticity deals with the artificial birefringence in a solid under the application of a mechanical stress/strain, quantitatively studied by Neumann in 1841 [106]. To conceptualise the effect we shall consider an ellipsoid whose shape represents the relative refractive indices observed when a ray of light traverses the respective axes of the medium, illustrated in Figure 5.8.

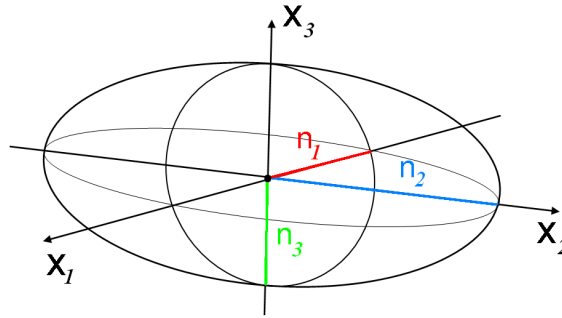


Figure 5.8: A schematic of an indicatrix

The fancy name of this construct is an indicatrix and is represented analytically by the ellipsoidal expression

$$\left(\frac{x_1}{n_1}\right)^2 + \left(\frac{x_2}{n_2}\right)^2 + \left(\frac{x_3}{n_3}\right)^2 = 1 \quad (5.16)$$

Simplifying the notation this can be written in terms of a tensor B_{ij} to give Equation 5.17, which can be stated more generally as Equation 5.18

$$B_{11}x_1^2 + B_{22}x_2^2 + B_{33}x_3^2 = 1 \quad (5.17)$$

$$\sum_{i,j=1}^3 B_{ij}x_ix_j = 1 \quad (5.18)$$

If a solid is stressed it is expected that the respective refractive indices n_1 , n_2 and n_3 shall change, meaning that the original indicatrix has also changed giving, another indicatrix tensor, B'_{ij} . The difference between these indicatrix tensors is

$$\Delta B_{ij} = B'_{ij} - B_{ij} \quad (5.19)$$

Introducing a theory of photoelasticity proposed by Pockels [106] this change in index as a result of stress/strain can be quantified. Pockels' theory is based on the following two postulates.

- I. Homogenous deformations will change the indicatrix.
- II. Within the elastic limit stress induces an optical change that can be represented as a linear function of nine stress components.

Considering Pockels' two postulates the change in indicatrix tensors can be stated as

$$\Delta B_{ij} = -q_{ijkl}\sigma_{kl} \quad (5.20)$$

The tensor q_{ijkl} has 81 elements called the stress-optical or piezo-optical coefficients. As previously introduced with stress and strain, contracted notation can be used for an anisotropic crystal due to symmetry arguments. Thus B reduces to single suffix notation and q reduces to a tensor of only 36 elements [106].

$$\Delta B_i = \sum_{j=1}^6 -q_{ij}\sigma_j \quad (5.21)$$

From the stress and strain relationship, Pockels assumes that the changes in B_{ij} are also linear functions of all nine components of the strain tensor. This gives the strain version of Equation 5.21 to be Equation 5.22

$$\Delta B_i = \sum_{i,j=1}^6 p_{ij} \epsilon_j \quad (5.22)$$

The change in indicatrix tensor can be approximated as

$$\begin{aligned} \Delta B_i = B'_i - B_i &= \frac{n_i^2 - n_i'^2}{n_i^2 n_i'^2} \\ &\cong \frac{(n_i - n_i')(n_i + n_i')}{n_i^4} \\ &\cong \frac{-\Delta n_i \cdot 2n_i}{n_i^4} = \frac{-2\Delta n_i}{n_i^3} \end{aligned} \quad (5.23)$$

Combining Equation 5.23 and Equation 5.22 and considering the thermal induced strain as a result of temperature variation, ΔT the change in index, as a result of strain, can be deduced to be

$$\begin{aligned} \Delta n_i &= \sum_{i,j=1}^6 \frac{\partial n_i}{\partial \epsilon_j} \epsilon_j + \frac{\partial n_i}{\partial T} \Delta T \\ &= -\frac{n_i^3}{2} \sum_{i,j=1}^6 p_{ij} \epsilon_j + \frac{\partial n_i}{\partial T} \Delta T \end{aligned} \quad (5.24)$$

The second factor that affects a grating's response to stress is fractional change in pitch as a result of mechanical effects, which shall now be formulated.

5.4.2 Mechanical Effects

Physical change in length as a result of strain will affect the grating's pitch and so affect the grating's Bragg condition. The following treatment shall consider the dependence pitch has on stress.

The definition of strain is the fractional change in an arbitrary length. Hence, the change in pitch $\Delta \Lambda$ can be expressed as

$$\Delta \Lambda_i = \Lambda_o \epsilon_i \quad (5.25)$$

Substituting Equation 5.24 into Equation 5.15 it can be stated that light polarised along the x_2 (TE) and x_3 (TM) directions is

$$\begin{aligned}\Delta\lambda_i &= 2\Lambda_i \left(-\frac{n_i^3}{2} \sum_{j=1}^6 p_{ij}\epsilon_j + \frac{\partial n_i}{\partial T} \Delta T + n_i\epsilon_i \right) \\ \frac{\Delta\lambda_i}{\lambda_i} &= -\frac{n_i^2}{2} \sum_{j=1}^6 p_{ij}\epsilon_j + \eta\Delta T + \epsilon_i\end{aligned}\quad (5.26)$$

where η is a thermal coefficient, brought about through the thermal strain (thermal expansion). This has been quantified in Chapter 3 to be typically $10 \text{ nm}^\circ\text{C}$. This is the most general formulation for the spectral response with respect to strain. The following subsection shall pin down this formulation for the specific case of silica based waveguides.

5.4.3 Optical Properties of Silica

Silica is an isotropic solid, and such the photoelastic tensors only consist of 2 elements. Considering fused quartz the photoelastic tensor p_{ij} is

$$p_{i,j} = \begin{pmatrix} p_{11} & p_{12} & p_{12} & 0 & 0 & 0 \\ p_{12} & p_{11} & p_{12} & 0 & 0 & 0 \\ p_{12} & p_{12} & p_{11} & 0 & 0 & 0 \\ 0 & 0 & 0 & p_{44} & 0 & 0 \\ 0 & 0 & 0 & 0 & p_{44} & 0 \\ 0 & 0 & 0 & 0 & 0 & p_{44} \end{pmatrix} \quad (5.27)$$

Considering 589.3 nm wavelength light traversing through fused quartz the stress-optic coefficients for p_{11} and p_{12} are 0.100 and 0.285 respectively, where $p_{44} = 1/2(p_{11} - p_{12})$ [107], as the refractive index of silica is similar for 589.3 nm and 1550 nm wavelengths only small deviation from these values are expected.

Introducing these specific values into Equation 5.27 gives

$$\frac{\Delta\lambda_2}{\lambda_2} = \epsilon_1 - \frac{n_2^2}{2} [p_{11}\epsilon_2 + p_{12}(\epsilon_1 + \epsilon_3)] + \eta\Delta T \quad (5.28)$$

$$\frac{\Delta\lambda_3}{\lambda_3} = \epsilon_1 - \frac{n_3^2}{2}[p_{11}\epsilon_3 + p_{12}(\epsilon_1 + \epsilon_2)] + \eta\Delta T \quad (5.29)$$

The following section shall compare theoretical wavelength shifts for bending and compression geometries to real mechanical stress tests. For consistency the same device has been used for all of the following mechanical tests. The device consists of a single mode uniform Bragg grating of 535.2 nm period and a length of 9 mm. The total thickness of the chip is 1.06 mm, it has a transverse width of 10 mm and a length of 40 mm. The thermal oxide was 14 μm thick and the thickness of deposited silica was 46 μm . Light was launched into the device via a polarisation-maintaining fibre V-groove. The single mode Bragg grating was measured using a broadband source and an optical spectrum analyser with a resolution of 0.01 nm. The full width at half maximum bandwidth of the grating is 16 GHz. The centre wavelength of the reflection spectra was obtained by a numerical Gaussian fitting algorithm. In the absence of an externally applied force the TE and TM Bragg reflected wavelengths were 1550.43 nm and 1550.61 nm respectively.

5.5 Bending

An effective way of inducing strain on the Bragg grating within our devices is through bending. Depending upon the geometry of the bending, tensile or compressive strain can be achieved at the grating as illustrated in Figure 5.9.

Previous work has considered three-point and four-point bending techniques primarily in fibre based devices [129] [130]. Three-point bending utilises three points of leverage to induce bending and four-point bending uses four points of leverage. This section investigates the effectiveness of these two techniques as mechanisms of strain tuning our fabricated device.

5.5.1 Normal Strains in Bending Beams

The silica-on-silicon devices is an example of a beam, with rectangular cross section of height h and width b . When subject to a bending moment, M , a beam deforms to an assumed circular arc, illustrated in Figure 5.10 (a). Such bending

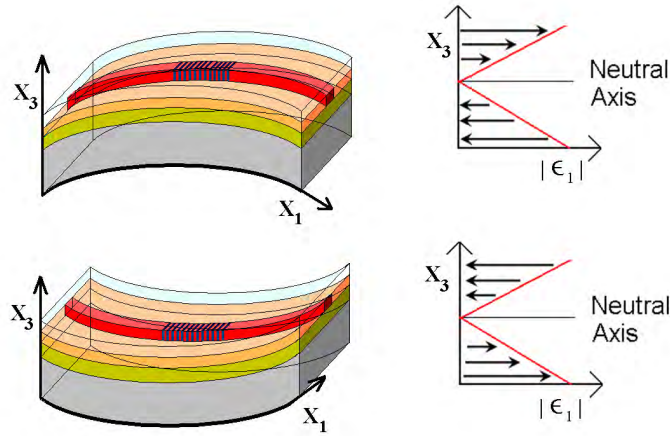


Figure 5.9: Schematic of planar Bragg grating under tensile and compressive strain, showing the strain ϵ_1 along the devices x_3 cross section

results in the top edge of the beam being extended and the bottom shortened, corresponding to tensile and compressive strain respectively. It follows that between these changes there must be a neutral axis, N , within the beam that undergoes no strain, represented by length CD and illustrated in Figure 5.10 (b).

(a)

(b)

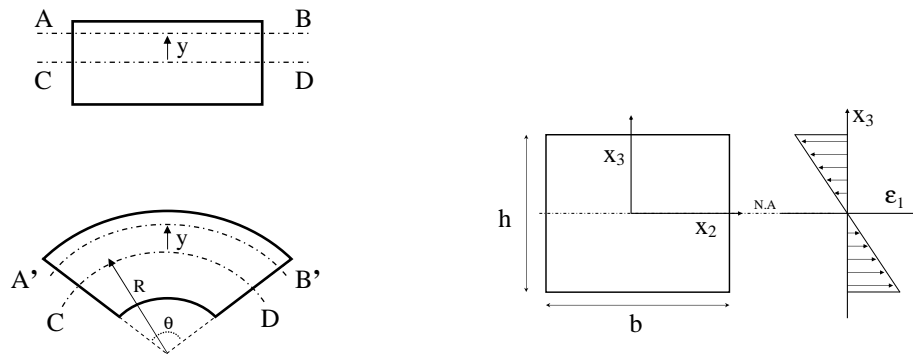


Figure 5.10: Schematic of a rectangular beam undergoing elastic bending depicting (a) deformation of the beam (side view) and (b) varying strains across the beam (cross sectional area)

Considering an arbitrary length AB that is a distance y from the neutral axis. For an applied moment it becomes stretched to $A'B'$, illustrated in Figure 5.10 (a). Mathematically this strain can be expressed as

$$\begin{aligned}
\epsilon_1 &= \frac{A'B' - CD}{CD} = \frac{(R + y)\theta - R\theta}{R\theta} \\
&= \frac{y}{R}
\end{aligned} \tag{5.30}$$

which in terms of stress becomes

$$\sigma_1 = \frac{Ey}{R} \tag{5.31}$$

Considering total force on the cross-sectional area of the beam

$$\Sigma F_1 = \Sigma \sigma_1 dA = \Sigma \frac{Ey}{R} dA \tag{5.32}$$

This has a moment about the neutral axis of

$$\Sigma F_1 y = \frac{E}{R} \Sigma y^2 dA = \frac{E}{R} I \tag{5.33}$$

where I is the second moment of area. Rearranging and inserting Equation 5.33 into Equation 5.30 gives

$$\epsilon_1(x_1, x_3) = \frac{M(x_1)(x_3 - N)}{EI} \tag{5.34}$$

As the device is a composite material it has effective mechanical properties, which for the case of bending requires a moment of area approach [122].

5.5.2 Moment of Area for a Composite

Due to the different mechanical coefficients of the silica and silicon an equivalent cross sectional area technique is required to interpret the moment of area and neutral axis. The equivalent area technique reinterprets the areas of the constituent material parts such that the Young's modulus of each section can be considered equal, as illustrated in Figure 5.11³.

³The following treatment shall assume that all the silica and thermal oxide layers have identical mechanical properties.

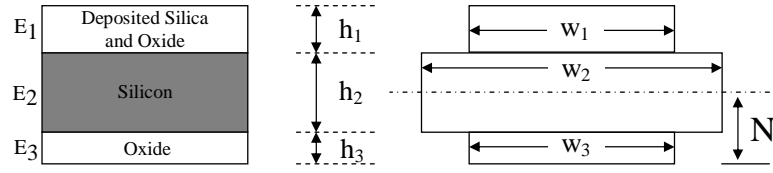


Figure 5.11: A schematic of the equivalent cross section for silica-on silicon composite

The neutral axis can be determined as the average neutral axis of each section weighted by their area, determined by

$$N = \frac{\sum_i w_i h_i N_i}{\sum_i w_i h_i} \quad (5.35)$$

The moment of area is a summation of the individual moment areas of the sections about the centroidal axis. Each layer is understood to have a moment area equal to that of a beam, giving a total moment of area determined by

$$I = \sum_i \left(\frac{w_i h_i^3}{12} + w_i h_i (N - N_i)^2 \right) \quad (5.36)$$

The values for the silica-on-silicon composite used for the following tests gave widths of 10 mm for w_1 and w_3 respectively and 23.14 mm for w_2 . This gives the location of the neutral axis to be at 0.52 mm and the moment of area to be 2.05 mm^{-4} .

This theory can now be applied to three-point and four-point bending techniques.

5.5.3 Three-Point Bending

Three-point bending achieves a moment through a three-point leverage system, illustrated in Figure 5.12 (a).

The strain along the beam is illustrated in Figure 5.12 (b) and can be understood by taking the moment, M , of the system

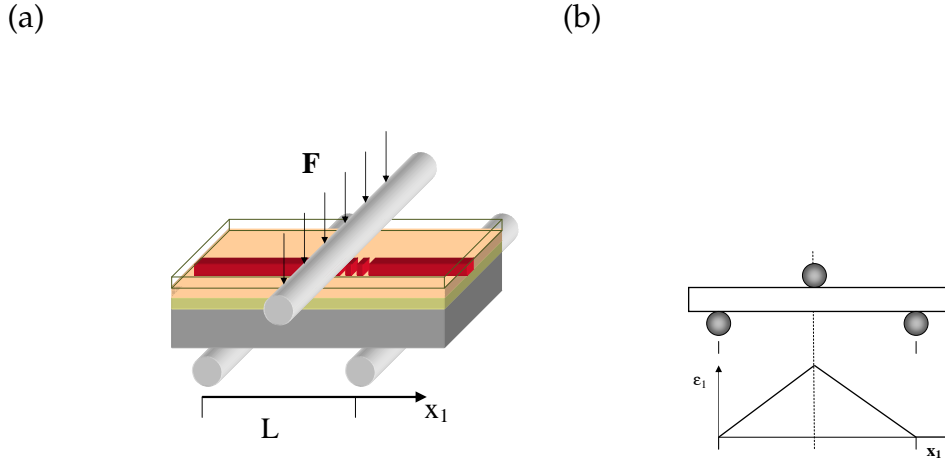


Figure 5.12: Schematic showing (a) planar Bragg grating under compressive strain using 3 point bending (b) the strain distribution involved

$$M(x_2) = \begin{cases} \frac{Fx_2}{2} & x_1 < L_1/2 \\ \frac{F(L_1-x_2)}{2} & x_1 > L_1/2 \end{cases} \quad (5.37)$$

Substituting this moment into Equation 5.34 gives the theoretical strain for an applied force.

$$\epsilon_1(x_1, x_3) = \begin{cases} \frac{Fx_1(x_3-N)}{2EI} & x_1 < L/2 \\ \frac{F(L-x_1)(x_3-N)}{2EI} & x_1 > L/2 \end{cases} \quad (5.38)$$

For the setup used the length L_1 was 30.0 ± 0.1 mm. By placing the silica side up or down compressive or tensile stress was achieved at the grating respectively. A tuning range of ± 43 N was tested as it was found experimentally that for a load of ± 48 N the ultimate shear strength of the device was catastrophically exceeded.

The overall strain tuning performance of the device is depicted in Figure 5.13 (a). The maximum wavelength shift observed for TE polarisation was 2.49 nm, corresponding to 311 GHz of tuning at 1550 nm. Normalising to an equivalent device with transverse width of 1 mm the tuning is 280 pmN^{-1} and 290 pmN^{-1} for TM and TE polarisations respectively. The tuning of the device was linear in terms of applied load as is expected from theory. Any deviation of the tuning from linearity was within the temperature stability of the laboratory and the known $10 \text{ pm}^\circ\text{C}^{-1}$ thermal response of the device.

As the length of the grating is under linear varying strain (dictated by Equation

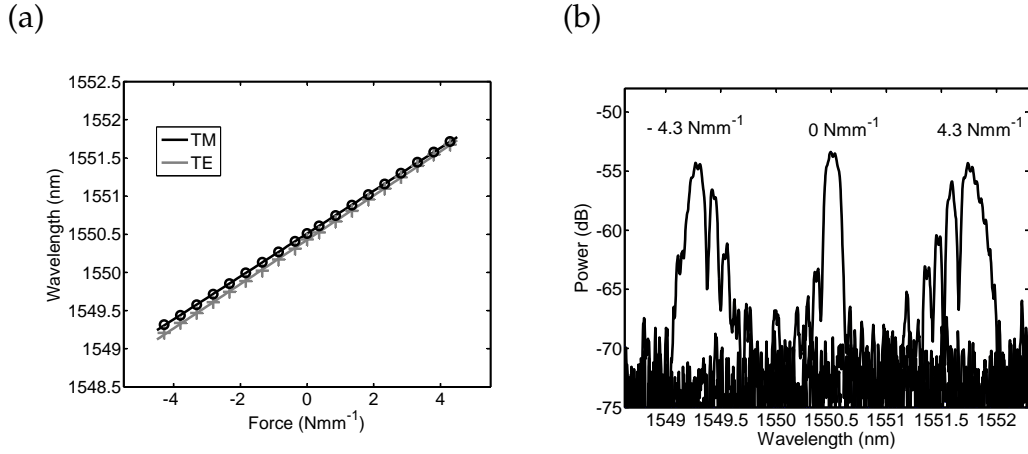


Figure 5.13: The tuning of a direct UV written Bragg grating undergoing three-point bending, displaying (a) the tuning curves for TE and TM polarisations and the (b) reflection spectra with and without load, for TE polarised light

5.38) there is a maximum and minimum spectral response that occurs for any given load. The maximum spectral response occurs at the location along the grating that experiences maximum strain (i.e. $x_1 = L/2$). The minimum spectral response occurs at the location along the grating that has minimum strain (i.e. the start and end of a grating). It must be noted that these maxima and minima occur for one particular load. For the maximum load that can be applied (43 N), the maximum and minimum spectral values have been calculated, listed in Table 5.1. The averaged TE and TM theoretical shifts are 2.48 ± 0.01 nm and 2.44 ± 0.01 nm respectively. The TE and TM shift deviates from the measured value by 0.01 nm and 0.03 nm respectively. The empirical and theoretical tuning of the TE polarisation lies within the accepted error of each other. However, the theoretical tuning for TM polarisation overestimates the empirical response by 0.8 % from accepted error. This discrepancy may be a result of the approximation used for the photoelastic constants, which were approximated for bulk fused quartz at 589.3 nm wavelengths, not direct UV written doped silica waveguides at 1550 nm wavelengths.

The reflection spectra for three different applied forces are shown in Figure 5.13 (b). It is clear from these that gratings with a ± 4.3 Nmm⁻¹ load are considerably less symmetric than the unstressed grating. This can be understood by considering Equation 5.38. The greater the central load the larger the linear variation in strain over the grating. Although such an effect may be desirable for dispersion compensation devices, for OADM filter symmetry is important. Forcing a constant strain over the grating using a four point bending system might remove this

Maximum Spectral Response		Minimum Spectral Response	
ϵ_1	1.13×10^{-3}	ϵ_1	7.89×10^{-4}
ϵ_2	-3.11×10^{-4}	ϵ_2	-2.18×10^{-4}
ϵ_3	-3.89×10^{-4}	ϵ_3	-2.73×10^{-4}
TE	2.92 nm	TE	2.04 nm
TM	2.89 nm	TM	2.01 nm

Table 5.1: Theoretical values for three point bending

phenomenon [129].

5.5.4 Four-Point Bending

Another way of inducing bending is through using a four point leverage system, as illustrated in Figure 5.14. The configuration illustrated induces compressive strain and inverting the orientation induces tensile strain.

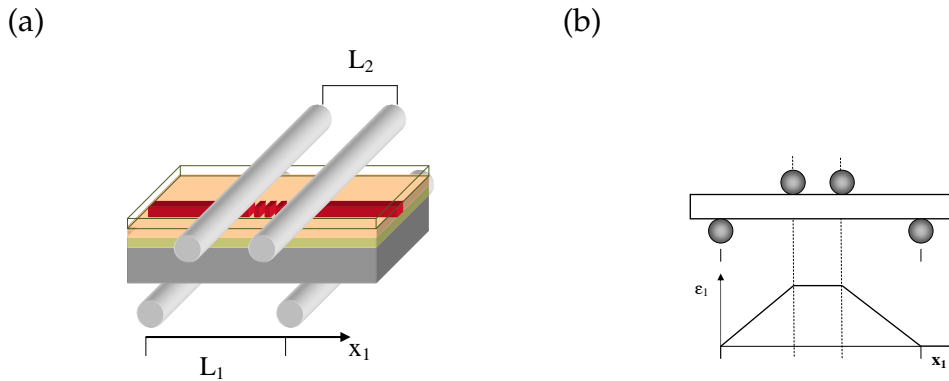


Figure 5.14: Schematic showing (a) planar Bragg grating under compressive strain using four-point bending and (b) its respective stress distribution along a beam undergoing four-point bending)

The moment for such a bending configuration between the smaller of the two pivots is

$$M(x_2) = \frac{F(L_1 - L_2)}{4} \quad (5.39)$$

Substituting the moment into Equation 5.34 gives

$$\epsilon_1(x_3) = \frac{F(L_1 - L_2)(x_3 - N)}{4EI} \quad (5.40)$$

Unlike for three-point bending, four-point bending can induce a constant strain over the grating length. In order to achieve this, the length of L_1 and L_2 were set at 30 ± 0.01 mm and 10 ± 0.01 mm respectively. The Bragg grating was located over the 10 mm length, as this was the location of constant strain.

The maximum magnitude of force that this four-point bending technique can withstand is 5.8 Nmm^{-1} , compared with 4.8 Nmm^{-1} for the three-point bending configuration. This can be understood with reference to Equations 5.38 and 5.40. For four-point bending the load required is greater to achieve the same maximum stress/strain on the device which all relates back to a failing strain/stress of the silica-on-silicon.

As a result of constant strain being applied a symmetric spectral response is predicted when tuned, this can be observed by comparing Figures 5.13 (b) and 5.15 (b). The spectra for the four-point bending is considerably more symmetric than that of three-point bending, however there is still an element of spectral broadening. This is believed to be a result of the stress affecting the defects of the silica and so affecting the distribution of refractive index resulting in spectral broadening.

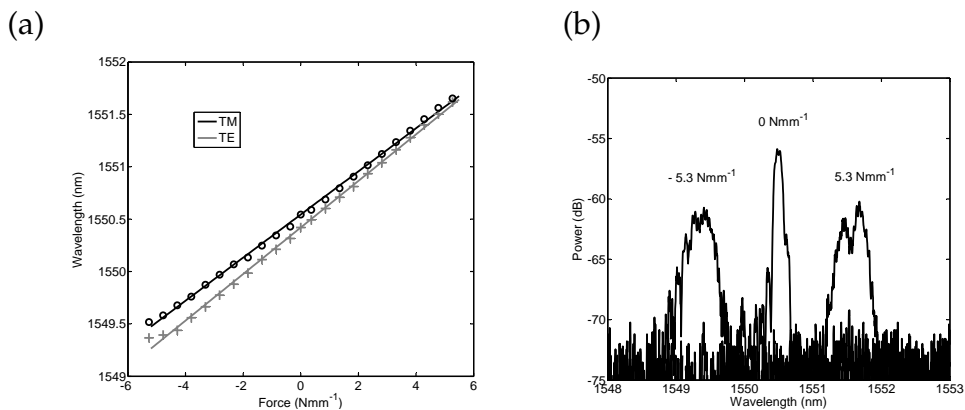


Figure 5.15: The tuning of a Direct UV written Bragg grating undergoing four-point bending, displaying (a) the tuning curves for TE and TM polarisations and the (b) reflection spectra of with and without load (TE polarised light)

The overall strain tuning of the device is depicted in Figure 5.15. The device has maximum TE and TM wavelength shifts of 2.31 nm and 2.14 nm respectively, which is comparable to that achieved with three-point bending. From Figure 5.15, if we normalise the tuning response for a 1 mm thick device the TE and TM mode

ϵ_1	9.26×10^{-4}
ϵ_2	-2.55×10^{-4}
ϵ_3	-3.20×10^{-4}
TE	2.39 nm
TM	2.36 nm

Table 5.2: Theoretical values for four point bending

tuning sensitivities are 218 pmN^{-1} and 202 pmN^{-1} respectively, which is lower than that for three-point bending. This is due to the moments for three-point bending inducing a larger leverage upon the sample.

It is apparent from Table 5.2 and Figure 5.15 that there is discrepancy between theoretical and empirical readings, of 0.08 nm for TE and 0.22 nm for TM polarisations. These discrepancies between theoretical and measured values are greater than those previously calculated for three-point bending. One potential reason for this discrepancy is a result of curve fitting inaccuracies, due to spectral broadening with increasing applied force. The theoretical response of the tuned Bragg grating stipulates a linear trend with applied force. The larger the applied force the greater the spectral broadening and so the greater the deviation from the theoretical linear response, which is apparent in Figure 5.15 (a). It must be noted that the largest deviation between theoretical and measured tuning occurs for TM polarisations. However, the data for TM better approximates a linear fit, as understood from R-squared values. Other potential reasons for deviation are variations of the approximations assumed, such as the photoelastic constants.

To measure the photoelastic constants for silica glass a lateral compression experiment was undertaken. So far the photoelastic approximation for germanium doped silica has been approximated to that of fused silica, which has served as a sufficient approximation. However, deviations may exist for structures experiencing greater strains.

5.6 Lateral Compression

A lateral compression is an effective method of obtaining the photoelastic constants of a material, as it achieves the largest difference between TE and TM polarisations.

sation. Lateral compression refers to a unidirectional force along the x_3 dimension. The corresponding strains of which are

$$\epsilon_{1,2} = -\frac{\nu_{31}\sigma_3}{E_3} \quad (5.41)$$

$$\epsilon_3 = \frac{\sigma_3}{E_A} \quad (5.42)$$

where E_3 is the effective Young's modulus and ν_{31} is the effective Poisson ratio, having values of 74.98 GPa and 0.119 respectively and E_A is the Young's modulus of silica. Inserting the respective strains into Equations 5.28 and 5.29, it is possible to solve the photoelastic constants p_{11} and p_{12} by rearranging the equation into the form.

$$\frac{1}{\lambda_2} \frac{d\lambda_2}{d\sigma_3} = (A - B_2 p_{11} - C_{13} p_{12}) \quad (5.43)$$

$$\frac{1}{\lambda_3} \frac{d\lambda_3}{d\sigma_3} = (A - B_3 p_{11} - C_{12} p_{12}) \quad (5.44)$$

where for convenience

$$A = -\frac{\nu_{31}}{E_3} \quad (5.45)$$

$$B_2 = -\frac{n_2^2 \nu_{31}}{2 E_3} \quad (5.46)$$

$$B_3 = \frac{n_3^2}{2 E_A} \quad (5.47)$$

$$C_{13} = -\frac{n_2^2}{2} \left(\frac{\nu_{31}}{E_3} - \frac{1}{E_A} \right) \quad (5.48)$$

$$C_{12} = -n_3^2 \frac{\nu_{31}}{E_3} \quad (5.49)$$

Equations 5.44 and 5.44 are just simultaneous equations which can be solved.

In order to deliver and monitor the lateral stress/strain an Instron 5569 electromechanical test machine (with a ± 50 kN static load cell) was used, alongside a specially adapted jig machined from mild steel, which applied force to a 30 ± 0.5 mm \times 10 ± 0.5 mm area on the device, illustrated in Figure 5.16. The jig also acted as a thermal reservoir, maintaining the temperature of the sample to within ± 0.5 °C

over the ~ 10 minute test period. This thermal drift was inferred through monitoring the temperature of the jig with a thermocouple during experimentation and assuming jig and sample had sufficient thermal contact. Experiments were undertaken individually for each polarisation.

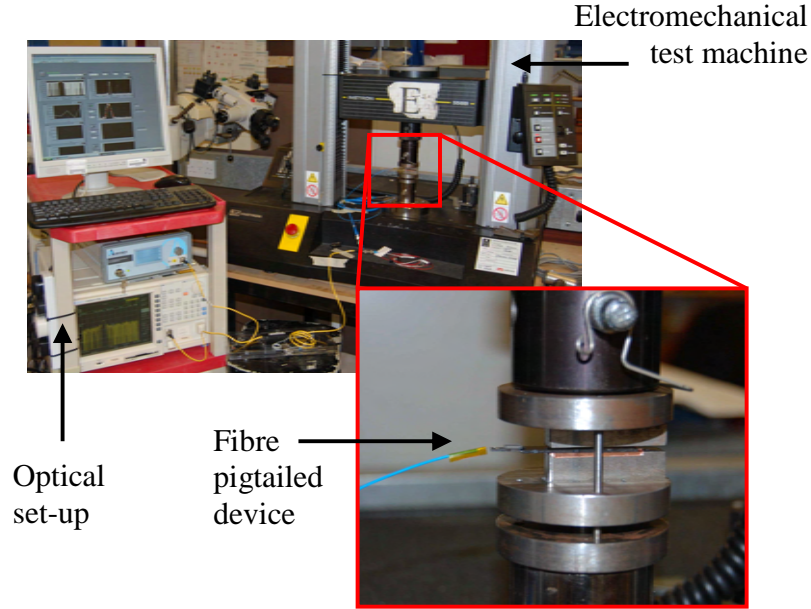


Figure 5.16: Lateral compression experimental set-up

The Bragg wavelength (TE) and strain response to force is shown in Figure 5.17 (a). It can be seen that for forces > 1500 N the relationship is not linear as expected with an elastic composite. Only after 1500 N of applied force does the expected elastic behaviour take place. This is believed to be a result of initial slop in the jig. As such TE and TM measurements were taken for stresses above 1500 N.

The spectral quality as a function of applied lateral force is shown in Figure 5.17 (b). As expected from Equations 5.28 and 5.29 lateral compression results in a positive shift in Bragg condition. What is also noticed from the spectra is broadening, which is thought to be a result of density distribution due to small variations in internal stress. As the fitting quality of a Gaussian to the spectral data diminishes for forces above 4000 N, this shall be considered to be the ceiling force for experimentation.

Figure 5.18 shows the relationship between Bragg wavelength and applied lateral compression for both TE and TM polarisations in the range 2500 N to 3500 N.

The spectral response for compression presented graphically in Figure 5.18 is -0.345 pmN^{-1} and -0.387 pmN^{-1} for TE and TM respectively. Placing these values

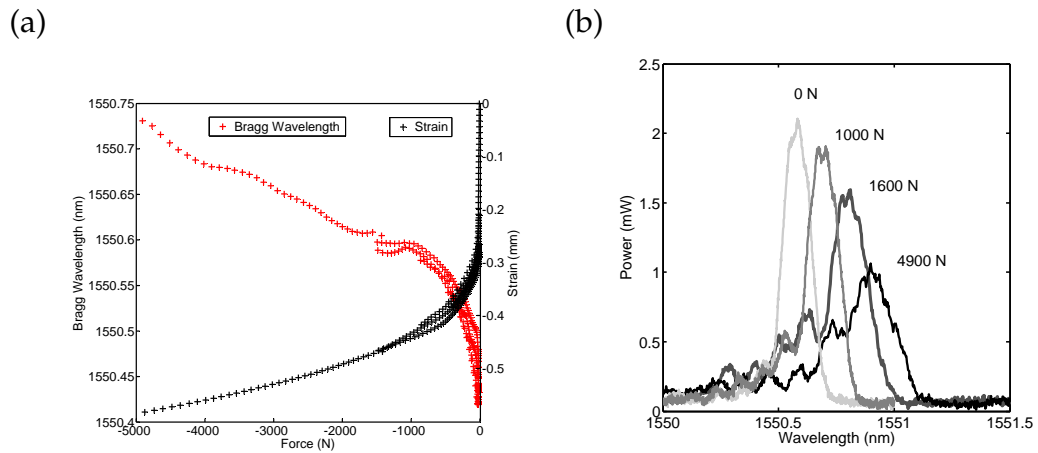


Figure 5.17: The response of a DUW chip under lateral applied force over a 30 mm² area depicting (a) the spectral dependence and strain dependence on applied force (b) the nature of the spectral response for four different applied forces

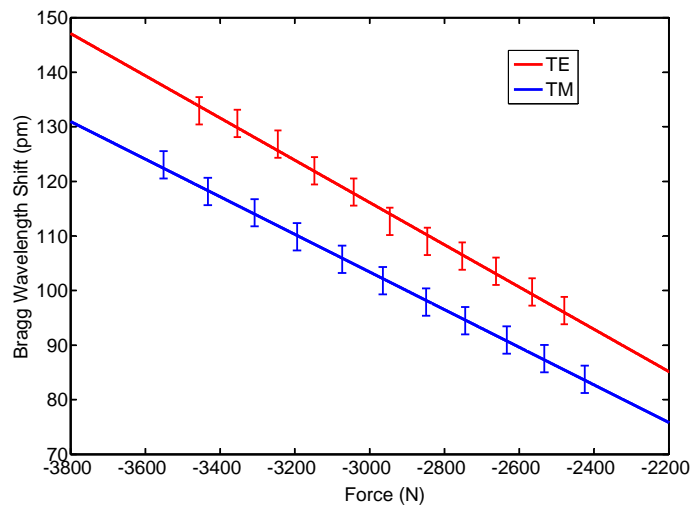


Figure 5.18: Lateral compression experimental set-up

into the simultaneous equations (Equations 5.44 and 5.44) gives the photoelastic constants to be 0.4761 and 0.5272 for p_{11} and p_{12} respectively. These values are much greater than those previously assumed for silica. It is noted that although the mechanical properties of the silicon and silica have been combined such to account for their composite form, the actual stress observed by the grating may be different. This may arise from an inherent curvature of the device and/or inaccuracies in the assumptions made for the composited behaviour, which lead to inferred effective indices.

5.7 Conclusions

We have demonstrated for the first time an applied strain tuning of ~ 311 GHz (corresponding to 2.49 nm of tuning at 1550 nm wavelengths) achieved by three-point and four-point bending a direct UV written silica-on-silicon integrated optical chip. This degree of tuning leads to potential application in optical networks as an OADM. Normalised to a device of a 1 mm width, the grating response to force for three-point bending was 280 pmN^{-1} and 290 pmN^{-1} for TM and TE polarisations respectively. This was in comparison to 202 pmN^{-1} and 218 pmN^{-1} for four-point bending.

For large applied moments the grating spectra in the three-point bending case displayed an apodised response, which can be understood from the variation in strain, predicted by theory, across its length. A four-point bending system did not display the asymmetric response associated with this apodisation. However, spectral broadening was observed, which is believed to be a result of variations in stress in the sample effecting internal densities.

The photoelastic constants for DUW waveguides were measured by applying lateral stress to the device. The measured values at 1550nm were 0.4761 and 0.5272 for p_{11} and p_{12} respectively. These measurements deviate greatly from expected values extrapolated from known values of fused silica. It is believed that the approximation assumed for lateral compression breaks down, especially for the large applied stresses considered. Using the polarisation data from three point bending the p_{11} and p_{12} effective photoelastic constants can be inferred to be 0.099 and 0.292 respectively.

The dynamic range and practicality of the fabricated devices to be used as physical sensors is limited by the devices dimensions, and the silicon wafers having mechanical weakness along their crystal planes. However, altering the dimensions or replacing the silicon could be a way of bridging the gap between these devices and the physical sensor market. A hypothetical future device may consist of an FHD layer deposited onto a silica window, which may be subject to extremes in stress (e.g. viewing window in a deep-sea submarine, jet plane or space shuttle). In such a composite structure, stresses in the window could be monitored in real time using direct UV written Bragg gratings in the FHD deposited layer.

To monitor shifts in a Bragg grating (e.g. for physical sensor applications) characterisation equipment similar to that used to characterise these devices (e.g. an OSA, broadband source and data interpreting software) can be used. However, the expense of this set-up would be significantly large, making the detection method less economically viable. However, the cost per device could be reduced through multiplexing several sensors into one system such that the cost per device would be distributed between many sensors. Another way to reduce cost would be to alter the interrogation set-up. For example, a photodiode and single frequency laser source could be used to replace the OSA and a broadband source respectively. Such a system would require the laser source to be aligned spectrally on top of the Bragg grating, which is to be monitored. The reflected laser light could then be monitored in reflection, transmission or both. As the Bragg grating shifts relative to the spectrally fixed laser light source the reflected power measured at the photodiode would vary and could be interpreted.

Chapter 6

Membrane Transducers

6.1 Introduction

Membranes are a proven means to detect pressure and flow in lab-on-a-chip based devices [115]. A sufficient pressure difference across a membrane will result in its deformation, this physical effect can be monitored using optical [131], [132] or electronic [133], [134], [135] techniques, and can be used to measure pressure and/or flow.

Optical methods for monitoring pressure differentials across a membrane can be categorised into either intensity modulated [136], [137], polarization modulated [138], [139] or phase modulated [140], [141], [142] techniques. Arguably, Bragg gratings fall into this latter category of phase modulation, although they are different to interferometric techniques in that the phase change is seen as a shift in the Bragg reflection wavelength rather than an intensity change, making them more immune to intensity variation of the source.

The majority of Bragg grating based membrane pressure sensors are based upon fibre Bragg gratings attached to a point on a membrane so that they stretch as the membrane deforms [143], [144] rather than being structurally part of the membrane. The following work outlines fabricated devices that consist of a direct UV written Bragg grating contained within a thin silica membrane, for pressure and flow sensing applications. Combined with temperature and chemical sensing capabilities this component will enhance future lab-on-chip realisation of direct UV written waveguide technology.

6.2 Theory

A pressure monitoring device can be realised by placing a Bragg grating within a thin silica membrane, illustrated in Figure 6.1 (a). Applying a sufficient pressure differential, ΔP ($=P_2-P_1$), across the membrane will cause it to buckle inducing strain on the grating within the membrane, illustrated in Figure 6.1 (b).

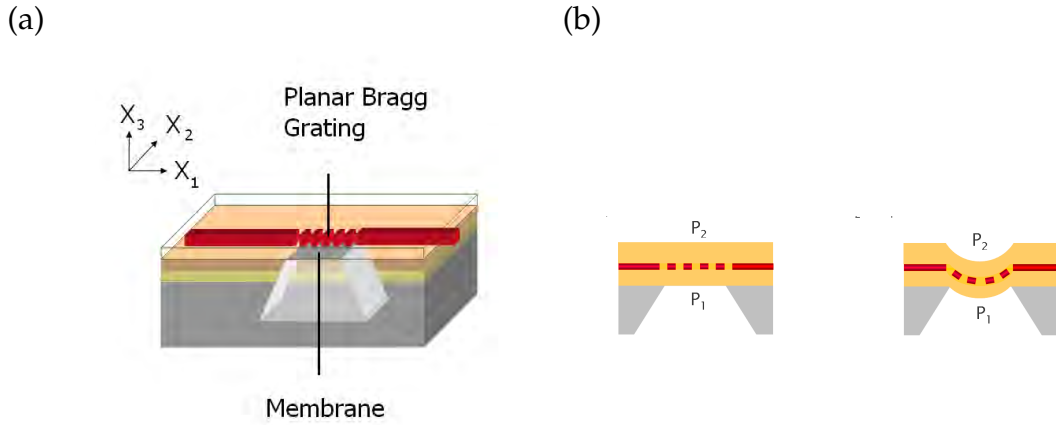


Figure 6.1: Conceptual schematic of (a) the membrane based planar Bragg grating pressure sensor construction (b) the gratings response to a pressure differential, visualised from the membranes cross section

Considering an arbitrary rectangular membrane of x_1 dimension a and x_2 dimension b , with the coordinate system centred on a corner of the membrane, then the first order buckling shape is defined as [145]

$$w(x_1, x_2) = \frac{w_0}{4} \left(1 - \cos\left(\frac{2\pi x_1}{a}\right)\right) \left(1 - \cos\left(\frac{2\pi x_2}{b}\right)\right) \quad (6.1)$$

where w_0 is the maximum buckling located at the centre of the membrane. This strain with respect to the buckling can be derived to be of the form

$$\epsilon_{1,2} = \left(1 + \left(\frac{dw}{dx_{1,2}}\right)^2\right)^{1/2} - 1 \quad (6.2)$$

From Equation 6.2 the strains ϵ_1 and ϵ_2 can be determined. The strain ϵ_3 can be found using the Poisson ratio of silica.

It must be noted that the idealised conceptual membrane response to pressure differentials illustrated in Figure 6.1 (b) is a simplification of the system. As a result of the FHD process the silica layers are under compressive stress. For specific

membrane parameters, this results in the buckling downwards of the membrane [146], [147]. Meaning particular membrane designs will exist is in a buckled state when $P_1 = P_2$.

The inherent (total) compressive stress, σ , the silica layers possess is contributed to by the thermal mismatch stress¹ between the silica and silicon, σ_t , and intrinsic stress, σ_i [148]. By its nature, intrinsic stress is difficult to quantify other than by empirical measurements. Thermal mismatch stress, however, can be analytically quantified. Assuming this is an example of a thin film system, differences in contraction of the film and substrate generate the thermal mismatch stress related as [148].

$$\sigma_t = E(\alpha_{SiO_2} - \alpha_{Si})\Delta T \quad (6.3)$$

where α_{Si} and α_{SiO_2} are the expansion coefficients of silicon and silica, having values of $2.6 \times 10^{-6} \text{ }^\circ\text{C}^{-1}$ and $4.9 \times 10^{-7} \text{ }^\circ\text{C}^{-1}$ respectively, ΔT is the difference between the consolidation temperature and room temperature which is $\sim 1200 \text{ K}$, resulting in a stress of $\sim 180 \text{ MPa}$. If the inherent stress is greater than a critical stress the membrane will buckle.

First order membrane buckling of an arbitrary rectangular membrane is understood to have a calculable critical stress σ_{cr} , defined as [145]

$$\sigma_{cr} = \frac{1}{9} \frac{\pi^2 E h^2 a^2}{1 - \nu^2} \left(\frac{3}{a^4} + \frac{3}{b^4} + \frac{2}{a^2 b^2} \right) \left(1 + \frac{a^2}{b^2} \right)^{-1} \quad (6.4)$$

where E is the Young's modulus and ν the Poisson ratio of the silica. Figure 6.2 indicates the critical stresses for three membrane dimension ratios that have a set thickness of $40 \text{ }\mu\text{m}$.

Values below the thermal mismatch stress line are expected to satisfy the condition $\sigma > \sigma_{cr}$ and hence are expected to buckle, indeed this trend has been observed experimentally for membranes of the respective dimensions.

¹Thermal mismatch stress is often incorrectly shortened to thermal stress. However, it must be noted that thermal stress is the stress that is incurred with a thermal gradient.

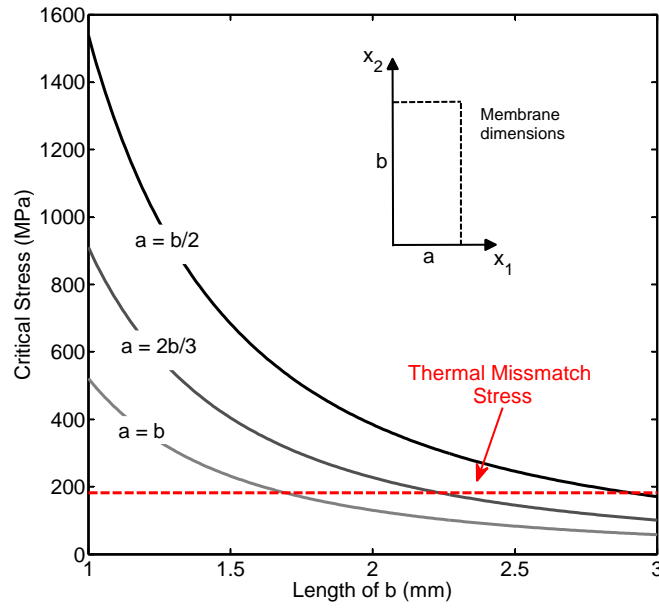


Figure 6.2: The critical stress required for buckling with respect to membrane dimension and the thermal stress mismatch (values are calculated for a $40\mu\text{m}$ thick membrane)

6.3 Fabrication

For membrane fabrication three-layer silica-on-silicon wafers were used as a thin layer of silica was desired. This choice ensures buckling of millimetre dimension membranes, as understood from Equation 6.4. All Bragg gratings were Gaussian apodised and written at a fluence of 20 kJcm^{-2} and duty cycle of 0.5. The fabrication steps post DGW are illustrated in Figure 6.3

To fabricate a membrane an area of the thick thermally grown oxide was selectively removed on the underside of the device. As the remaining thermal oxide is thick it acts as an effective etch mask for the device. Several methods for removing the thermal oxide were attempted. HF etching the oxide required polyimide tape to mask the FHD layers. The oxide could also be physically removed using a diamond scribe or aluminium oxide grinding bit (used in conjunction with a dremel tool), the latter of which can be used to remove a large proportion of silicon ~ 0.5 mm prior to etching. This significantly reduces the total time required for etching.

The exposed silicon was anisotropically etched in 50 % KOH solution for ~ 7 hours at 90°C . This removes all the silicon under the grating such that the three silica

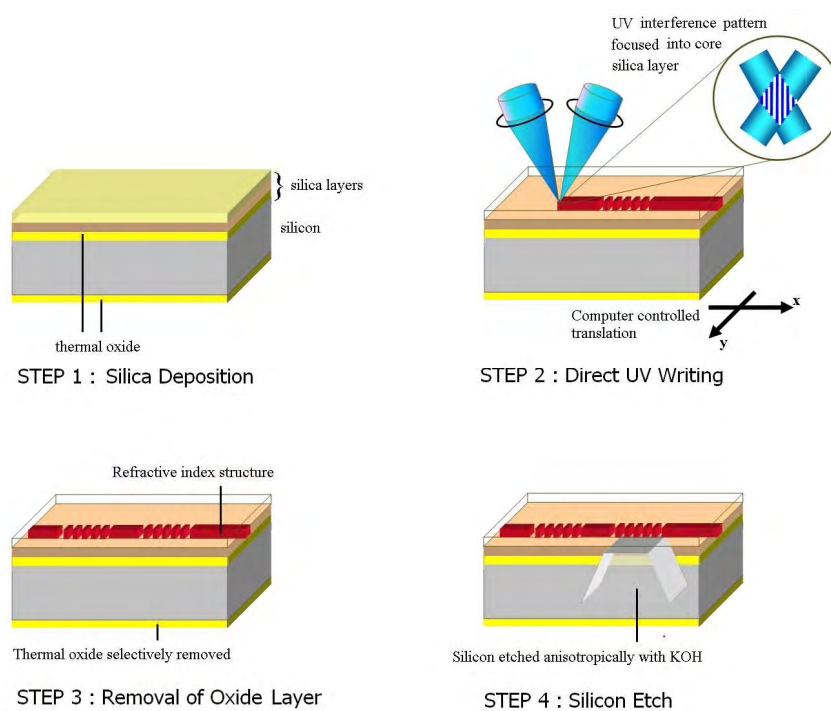


Figure 6.3: Illustration detailing the fabrication process for a direct UV written pressure sensor chip

layers form a thin membrane. As the side of the chips are exposed silicon, they were masked by PTFE tape. At temperatures (above 70°C) this resulted in a white residue being left on the sample, which was could later be removed by flash etching the device in KOH for a further 2 minutes.

To deliver light into the device a fibre optic polarising maintaining V-groove chip was aligned to the input channel waveguide and permanently secured using an epoxy.

6.4 Devices

Using the outlined fabrication procedure three types of membrane based transducer were fabricated: a pressure transducer; membrane strain map; and a flow transducer.

6.4.1 Pressure Transducer

The membrane based pressure transducer exploited the inherent buckling effect (discussed in theory section of this chapter) to distinguish positive and negative pressure differentials.

The fabricated membrane was 2 mm by 3 mm and had a thickness of 40 μm . The critical stress of such a membrane can be calculated to be 101 MPa, which is significantly less than the thermal mismatch stress, observed graphically in Figure 6.2. A Bragg grating resided along the membranes 2 mm width and was centralised along the 3 mm length. To deliver a pressure differential across the membrane the device was glued to an aluminium fixture that could deliver positive or negative pressure to the membrane using the inlet and outlet feeds from a vacuum pump, as illustrated in Figure 6.4.

The fabricated device was observed to have a maximum pressure sensitivity of 20 pm/kPa and by exploiting the inherent buckling of the membrane can distinguish between positive and negative pressure differentials, over a 100 kPa range, as shown in Figure 6.5. Note that when the pressure on top of the membrane, P_2 , is greater than that on the bottom, P_1 , the pressure differential was considered to

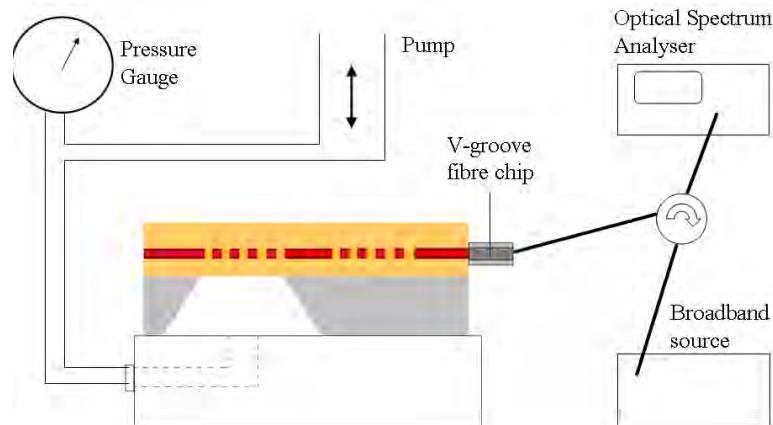


Figure 6.4: Schematic of the pressure delivery and optical interrogation set-up

be positive (see Figure 6.1 (b)). Assuming the minimum resolvable spectral shift is 1 pm, this membrane can resolve pressure differences of 5 Pa.

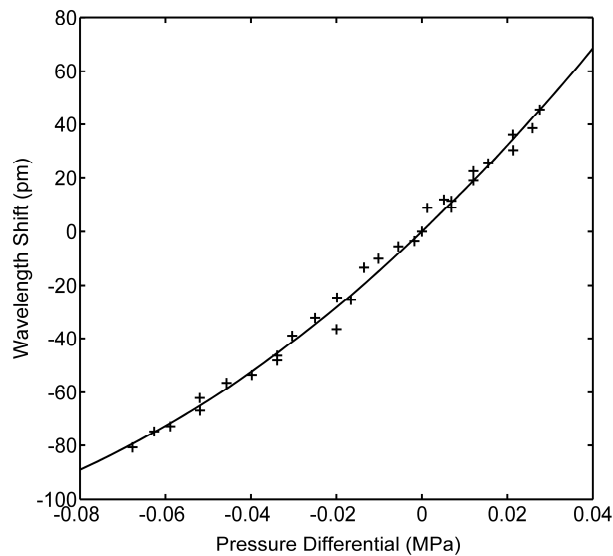


Figure 6.5: The spectral response of the Bragg grating for a range of pressure differentials

It is understood that the relationship between pressure and maximum membrane buckled displacement, w_0 , is linear [147]. As the buckling displacement of the membrane is relatively small with respect to its dimensions it is expected from Equations 6.1 and 6.2 that strain will have an approximate positive quadratic nature. This will mean, from Equations 5.28 and 5.29, that the Bragg wavelength

response is quadratic, which is the form observed in Figure 6.5.

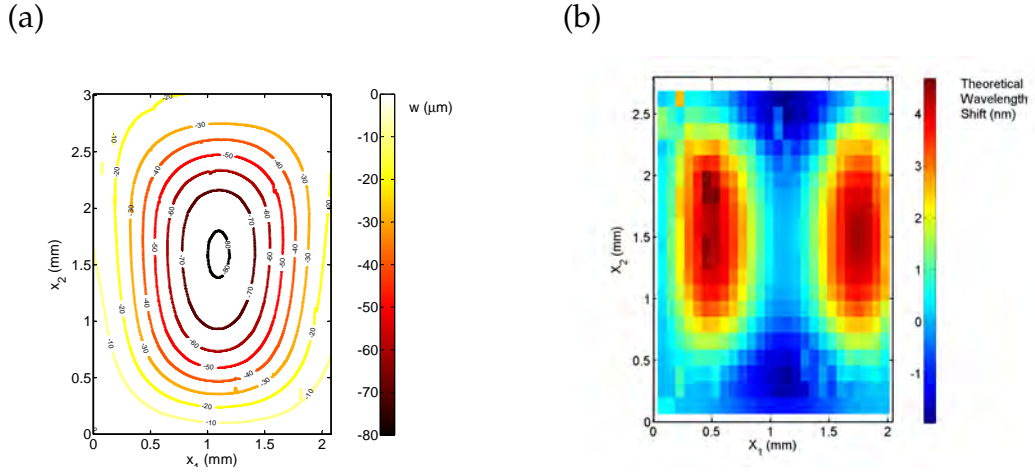


Figure 6.6: Properties of the fabricated membrane depicting the (a) buckling and (b) the spectral response of a horizontal Bragg grating localised at any position along the length of the membrane

Using a step profiler the 3-dimensional topography of the buckling was measured, the data of which is shown in Figure 6.6 (a). This is an example of first order buckling as it fits the characteristics of Equation 6.1. The maximum deflection w_0 for this membrane is $82 \mu\text{m}$. Using the 3-dimensional information from the step profiler (Figure 6.6 (a)) the strain pre-etching and post-etching can be deduced. Using this information and Equations 5.28 and 5.29 the spectral shift was inferred for any grating waveguide along the x_1 direction, as represented in Figure 6.6 (b). For the calculation, that led to this graphical representation the photoelastic constants calculated in Chapter 5 were implemented. The apodised grating measured in this work spans the 2 mm width of the membrane for $x_2 = 1.5 \text{ mm}$. As Figure 6.6 (b) indicates for its size the grating is in the optimum position. However, the size of the grating relative to the membrane results in variation in strain across its length, which results in a variation of pitch and refractive index over the grating, in accordance with Equations 5.28 and 5.29. The result of this can be seen in Figure 6.7 for the gratings spectral response pre and post KOH etching. It must be noted that the reflected power before etching is less than that post etching. This is believed to be a result of coupling losses as a fibre pig-tail was not maintained during the silicon etch step. Due to this strain variation, there is a spectral broadening and an asymmetric form to the response, similar to the effect observed in Chapter 5 for the three-point bending device. However, it must be noted that this effect does not limit the ability to measure grating shifts.

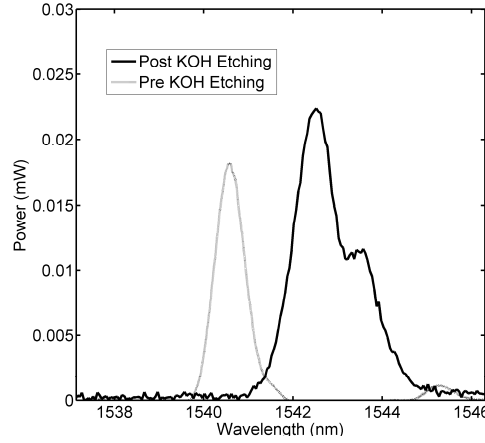


Figure 6.7: The spectral response of the grating located over the membrane pre and post KOH etching

The theoretical maximum spectral shift post-etch compared to pre-etch, can be obtained from Figure 6.6 (b). This maximum theoretical shift is around 4.4 nm, however our grating extends across the whole membrane and so shows a smaller peak shift of around 2.5 nm, Figure 6.7. It must be noted that the increase in power post etching observed in Figure 6.7, is a result of poor coupling into the waveguide prior to the wet etching stage. In fact it has been observed that negligible loss (bend loss, Raleigh loss) results from the removal of the silicon beneath the silica area. It must be noted that to suppress spectral side lobes the written grating has been Gaussian apodised with an optimised spatial standard deviation of 0.35 mm. The nature of the apodisation is understood to reduce the contribution of the higher index variation sites at x_1 equal to 0.5 mm and 1.5 mm. It is also noted that the theoretical calculations used known values for 589.3 nm wavelengths in bulk quartz, not in DUW channels in germanium doped silica at 1550 nm wavelengths, and so more deviations would be expected.

The sensitivity of the developed device to membrane deflection is dependent upon where wavelength shift is measured, since chirping is shown. Reducing the physical length of the Bragg grating could reduce this chirping effect. From Figure 6.6 (b) insights into the optimum location for grating position can be found. The strain on the membrane can be calculated from Equations 6.1 and 6.2. It can be seen from these equations that the maximum strain occurs at the maximum/minimum of the cosine derivative function, of Equations 5.28 and 5.29, meaning the optimum wavelength shift occurs at $x_2 = b/2$ and $x_1 = a/4, 3a/4$ as these are the locations of maximum strain. It must also be noted for future device refinement that it is not

just maximum strain that gives maximum spectral response, but rather the way they each interact described by Equations 5.28 and 5.29, which is also dependent upon the waveguide orientation on the membrane.

So far only a single grating has been placed on the membrane and its response elsewhere inferred through theory. To corroborate with theory a membrane mapping experiment was undertaken. The objective of this task was to map out the spectral shift as a function of gratings position on the membrane.

6.4.2 Membrane Deflection Map

A 100 apodised Bragg grating array was written on a sample in order to map deflections in the membrane, post etching. The array was arranged in a series of 10 parallel channels spaced 1 mm apart, which took over 2 hours to UV write, using a fluence of 20 kJcm⁻¹. Each channel had 10 'array' gratings each one 1 mm in length and placed end-to-end, such that a 10 mm by 10 mm sensing area was blanketed over the membrane. In addition to the 100 gratings placed over the membrane area were temperature reference gratings, placed at a 2 mm distance from the membrane, for each channel. The 10 channels, each containing 11 gratings were characterised individually by scanning a fibre across their length, illustrated in Figure 6.8.

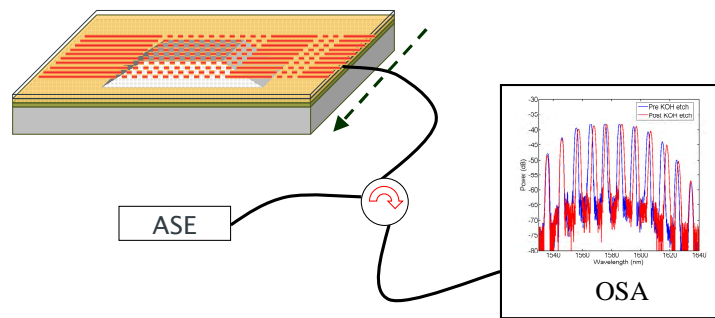


Figure 6.8: Schematic of membrane mapping configuration

The fabricated device used a wafer with silica thickness of $\sim 40 \mu\text{m}$, which was diced to 20 mm x 20 mm chips. This allowed for larger membranes to be tested. It was found experimentally that for silica thickness of $\sim 40 \mu\text{m}$ the largest membrane that could be fabricated is 6 mm x 6 mm. To take advantage of the 100 grating array

a membrane of 10 mm x 10 mm was partially etched, such that some silicon still remained and formed part of the membrane. This partial etch allowed a 10 mm x 10 mm membrane to be fabricated. The thickness of silicon remaining on the underside of the membrane was difficult to quantify as it varied across the length, with the central area of the membrane showing an absence of silicon. This partial etching and subsequent uneven distribution of remaining silicon resulted in an asymmetric buckling nature of the membrane, illustrated in Figure 6.9, which is in contrast to the symmetry possessed in Figure 6.6 (a).

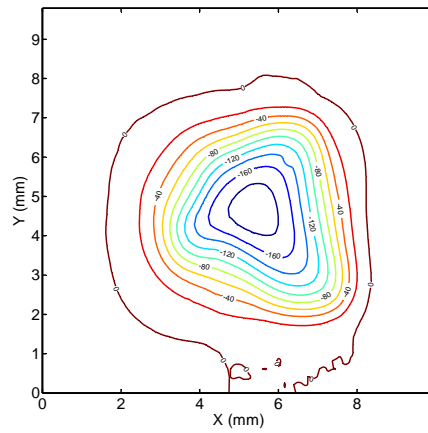


Figure 6.9: Membrane deflection as measured by a surface profiler

Using this deflection data the spectral shift pre-etch and post-etch can be inferred, as was done previously for the case of the pressure transducer, the only difference being is that the theoretical model (Figure 6.10 (a)) can be corroborated directly with spectral measurement (Figure 6.10 (b)).

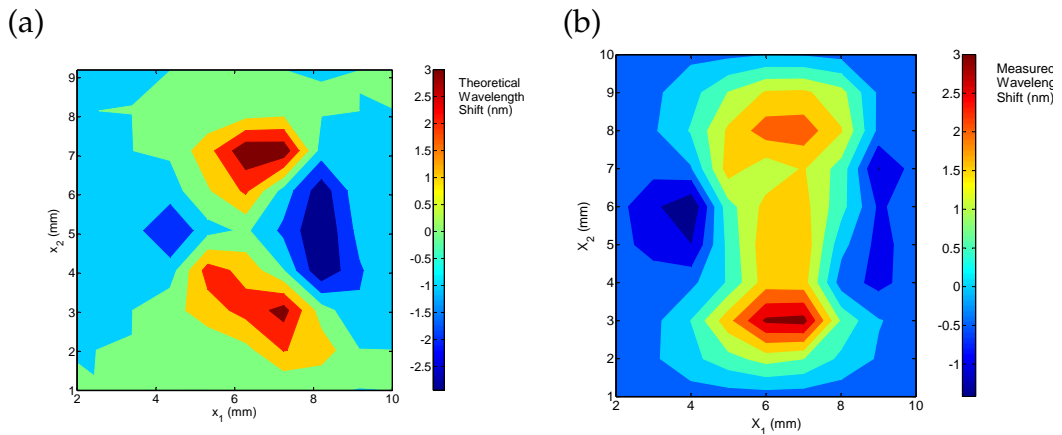


Figure 6.10: The spectral response according to (a) theoretically data inferred from measured deflection (b) empirically measured

The theoretical prediction and the measured spectral shift display similar characteristics. The photoelastic constants calculated in Chapter 5 were again used to calculate the theoretical shift. The accepted photoelastic constants for fused quartz show a similar predicted response, but with a spectral range from -1 nm to 4 nm as a result of a smaller strain-optic contribution. Deviations between theoretical and predicted data may be contributed to by the presence of the partially etched silicon, which is not considered in the model.

6.4.3 Flow Transducer

Mass markets in biotechnology, medical diagnostics, pharmaceutical research and homeland security drive demand for lab on a chip based technology. Flow based sensors form an integral part of these chips for their use as dosing systems and mass flow controllers. A single membrane can monitor pressure, and pressure in turn can be used to monitor flow. However, it is not sufficient to infer flow from a single pressure measurement. If flow, I , is to be quantified one requires a pressure differential, ΔP , and the resistance of flow, R , between the pressure differential. This resistance is dependent upon the viscosity of the fluid and parameters of the channel. The relationship between these terms is analogous to Ohms law in electronics (potential difference \rightarrow pressure difference, electric current \rightarrow flow, electrical resistance \rightarrow flow resistance) and can be formulated as²

$$\Delta P = (P_2 - P_1) = IR \quad (6.5)$$

Membrane techniques can be used to monitor a pressure differential across a channel in one of two ways, either by accessing a single membrane from both sides or by monitoring the pressures of two membranes. Both geometries have advantages and disadvantages for lab-on-a-chip applications. Single membranes can deal with larger pressures, assuming the output pressure is greater than atmospheric pressure, as the back-flow pressure would offset the input pressure. Two separate membranes have the advantage of being more sensitive (again assuming the output pressure is greater than atmospheric pressure) and have the ability to quantify the actual pressure as well as the pressure differential. The reason why

²It is understood that this equation holds for laminar flow conditions. For turbulent flow the resistance of the channel becomes flow rate dependent.

a two membrane system would be more sensitive than one, stems from the fact that the response to pressure differential is quadratic, as observed in Figure 6.5. If both membranes are working at higher pressure differentials they are expected to demonstrate an improved flow resolution.

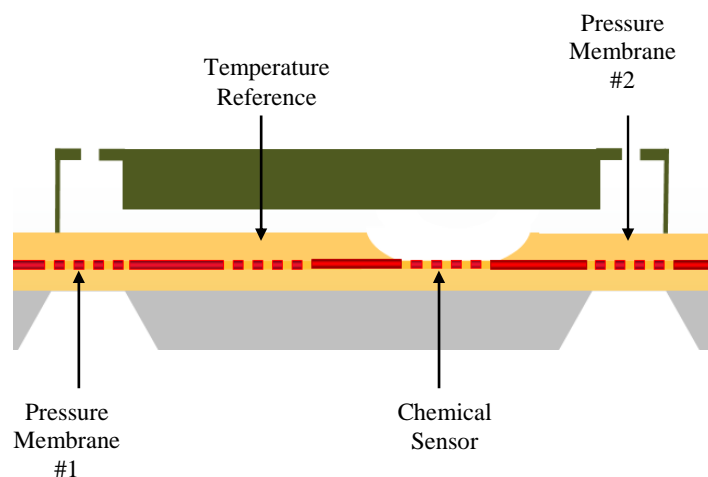


Figure 6.11: A conceptual schematic of a fully integrated chip with chemical, temperature, pressure and flow sensing capability

A two membrane system, illustrated in Figure 6.11, was fabricated to monitor fluid flow. To fully realise the integration capability of a direct UV written chip, the fabricated device consisted of four Bragg gratings, which collectively monitored pressure, flow, chemical and thermal fluctuations, illustrated conceptually in Figure 6.11. This device was realised upon a 10 mm by 20 mm chip. As with the pressure transducer the silica thickness was $39.8\ \mu\text{m}$ and contained two membranes of dimensions 2 mm x 3 mm, illustrated in Figure 6.12. The written gratings were 2 mm long and Gaussian apodised, written with a duty cycle of 0.5 and a fluence of $20\ \text{kJcm}^{-2}$. They were located over the membranes smallest dimension and centered upon its longest length, just as in the case of the previously outlined pressure transducer.

In the fabrication of this device the chemical sensor grating was etched using HF acid, which was sequenced prior to the KOH silicon etch, as the silica was easier to mask prior to membrane fabrication. The fully integrated pressure, flow, chemical and temperature device fabricated is pictured in Figure 6.12.

The reflection spectra of the device pre-etch and post-etch is depicted in Figure 6.13. As well as the reflection spectra indicating a shift in the membrane gratings due to the inherent buckling, a shift was also observed for the chemical grating

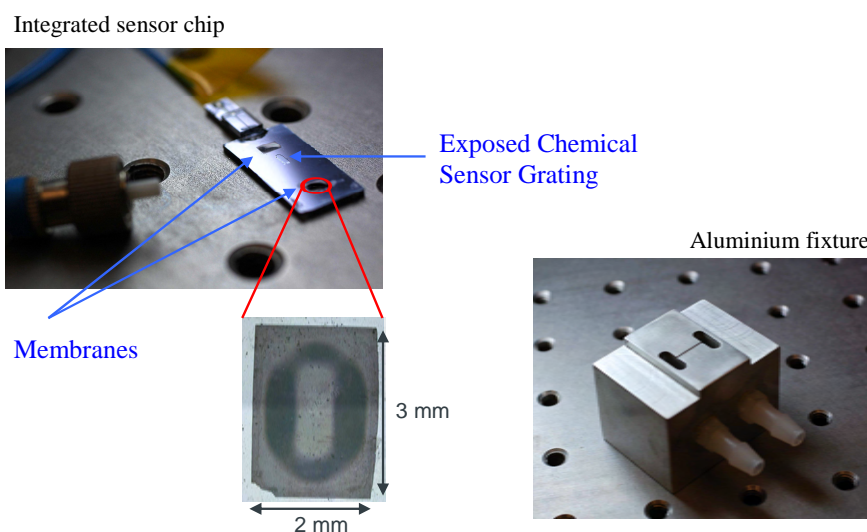


Figure 6.12: A photograph of the fully integrated pressure, flow, temperature and chemical chip

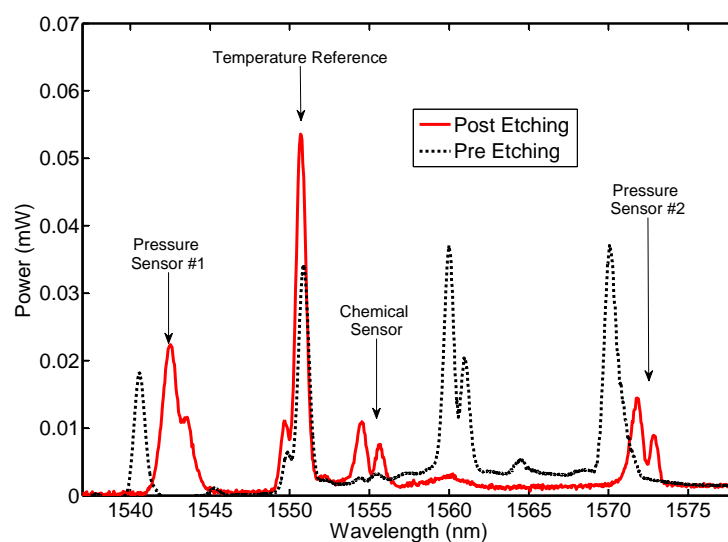


Figure 6.13: The spectral response of a fully integrated pressure, flow, temperature and chemical chip depicting the reflection spectra pre-etch and post-etch

post etching. What is interesting, is that this spectral shift or ~ 5 nm shift, is much greater than the expected spectral shift of ~ 1 nm, observed experimentally in similar devices. It was found that post HF etching the expected ~ 1 nm shift occurs. However, after the KOH etch this reduced by a further ~ 4 nm, which effects the exposed Bragg grating but not the buried gratings (i.e. no response occurs with the temperature reference grating). This effect did not degrade the sensitivity of the exposed grating, but may be suppressed by effectively masking of the grating during the KOH etch.

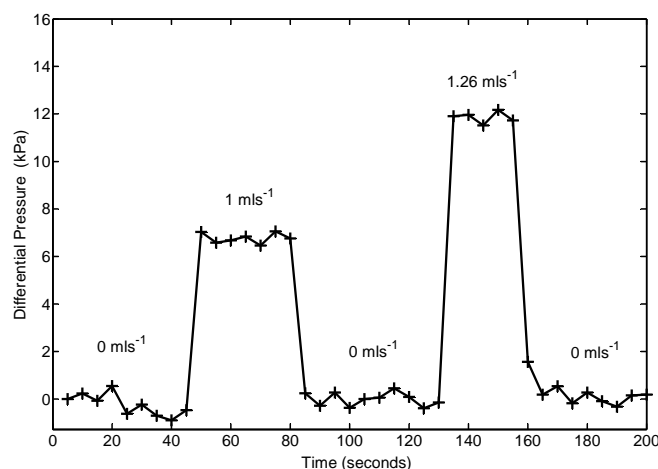


Figure 6.14: The pressure differential calibrated from the gratings pressure response for two different flow rates

To allow flow from one membrane to the other, via the temperature reference and chemical sensor grating an aluminium fixture as illustrated in Figure 6.12 was used. The fixture contained an 8 mm long channel of thickness 1 mm and depth $100 \mu\text{m}$. Figure 6.14 depicts two different flow rates along the channel with respect to the calibrated differential pressure of the membranes. The flow resolution for this device is $\sim 33 \mu\text{ls}^{-1}$, however, it must be noted that this resolution is dependent upon the flow resistance of the channel.

6.5 Conclusions

A differential pressure sensor has been realised by removing a section of the underlying silicon in our silica-on-silicon device, such that a thin silica membrane remains. Integrating the membrane component into the established grating based

sensors allows the realisation of a lab-on-a-chip based device that is capable of monitoring pressure, flow, temperature and have chemical sensitivity.

The maximum pressure resolution demonstrated so far has been 5 Pa, which has been achieved over a 100 kPa range. Fabricating a membrane such that the inherent thermal mismatch stress is greater than the critical stress required for buckling allows for the differentiation between positive and negative pressure differentials.

The spectral response of a grating upon a deformed membrane can be understood through the theoretical strain response the grating undergoes. Using this information has identified optimum locations for grating positioning and can be utilised in future device refinement.

Chapter 7

Thermo-Optic Effects

7.1 Introduction

Thermo-optic effects, which are refractive index changes caused by temperature variations in a material, have been demonstrated in commercial OADM configurations. These devices are of particular interest as their typical tuning speed is millisecond order [149].

Silica-on-silicon devices are ideal platforms for thermo-optic based OADM devices as they are physically and chemically stable. The majority of literature covering thermo-optically tuned Bragg gratings describes devices in fibre [150]. However, fibre based devices do not possess the integration advantages associated with planar technology [112]. Thermo-optic based OADM have also been demonstrated in several material platforms including silica-on-silicon, silicon-on-insulator [151], [152] and polymers [153], [112]. For large thermo-optic tuning ranges in planar devices (2500 GHz, corresponding to 20 nm in the C-band) polymer based substrates are best suited [112]. While polymers offer impressively large tuning ranges, there is an advantage in using silica-on-silicon technology especially as it is well established in telecom networks where it is used for AWG's, splitters and thermo-optic switches [27].

This chapter considers thermo-optic tuning of DGW devices for potential OADM applications.

7.2 Theory

The operational theory of the presented devices uses local heating of a Bragg grating to induce strain and thus tune the grating. Two geometrical configurations are considered, one configuration acts to polarise the input light as well as thermo-optically tuning it whilst the other does not polarise the light. The purpose of this section is to outline the theory of device operation for the two geometries examined.

7.2.1 Thermal Response

The thermo-optic effect is basically a special case of the strain-optic effect, where strain is a result of a temperature change. It is understood that a temperature increase results in thermal expansion, which can be expressed as strain such that

$$\epsilon_i = \alpha \Delta T \quad (7.1)$$

where α is the thermal expansion coefficient. Inserting Equation 7.1 into Equations 5.28 and 5.29 gives

$$\frac{\Delta\lambda}{\lambda} = \left(1 - \frac{n^2}{2}(p_{11} + 2p_{12})\right) \alpha \Delta T \quad (7.2)$$

which has assumed that the thermal expansion is equal along each principle axis. It is noted that the spectral shift resulting from temperature variation is different for each polarisation only as a consequence of the devices initial birefringence. Equation 7.2 is generally put more elegantly as [154].

$$\Delta\lambda_B = \lambda_B(\alpha + \zeta) \Delta T \quad (7.3)$$

where α is the thermal expansion coefficient and ζ is the thermo-optic coefficient. These coefficients correspond to change in grating pitch and effective index respectively. At the 1550 nm telecom wavelengths bulk heating experiments show the summation of these two coefficients to be about $10 \pm 1 \text{ pmK}^{-1}$.

7.2.2 Localised Heating

While bulk temperature monitoring for thermal referencing is a proven tool, bulk temperature manipulation for tuning applications has many disadvantages including a poor response time and low energy efficiency. By locally heating a grating element, one is manipulating a smaller thermal mass thus faster response time and greater energy efficiency is achieved. Local heating also has the advantage of multiple tuning elements being placed on one chip and tuned independently.

The proposed concept, illustrated in Figure 7.1, considers a small heating filament aligned over the top of the Bragg grating element. As the thermal conductivity of silicon is one-hundred times greater than silica's, heat is effectively removed from the local area allowing fast switching.

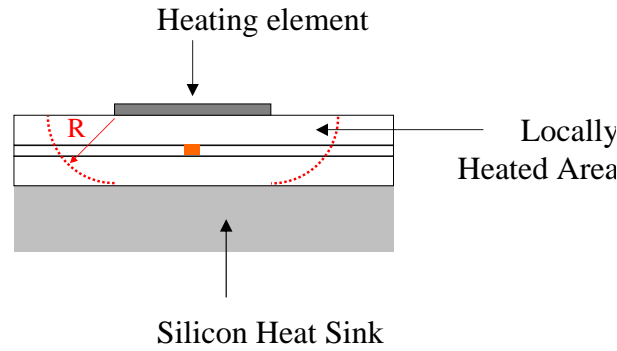


Figure 7.1: Schematic of localised thermal tuning concept

The silicon in turn can be placed in contact with a more effective heat sink. As a loose approximation for low dissipated powers the thermal gradient can be approximated to be within the red perimeter line, indicated in Figure 7.1.

There are two adaptations of the geometry illustrated in Figure 7.1, the basic geometry as shown and an adapted geometry where the overclad is removed, leaving the filament in direct contact with grating. Tuning range, tuning efficiency and response time is expected to be improved through removing the overclad layer. However, due to the large imaginary part of the metal heating filament, the adapted geometry is observed to act as a polariser, whilst the basic geometry does not.

7.2.3 Metal-Clad Polariser

A metal clad polariser is fabricated by depositing a thick metal layer onto the core of a guided mode. As previously discussed in Chapter 4, a plasmon hybrid mode is established for TM but not TE polarisations, as a result of Maxwell's equations. The TE and TM guided modes can be visualised, illustrated in Figure 7.2. These simulations consider a 350 nm thick nichrome layer of refractive index $3.542 + 6.436i$ [7].

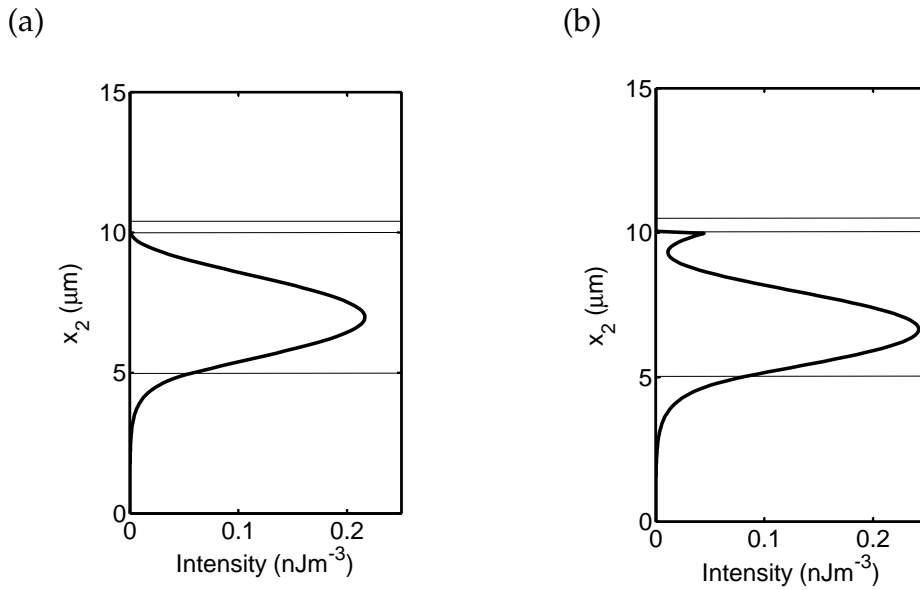


Figure 7.2: The supported modes for a topless sample with a thick NiCr filament overlay for (a) TE polarisation (b) TM polarisation

For such a thickness of nichrome the TE mode has an effective index of $1.4552 + 2.624 \times 10^{-5}i$ and the TM mode has an index of $1.4539 + 8.274 \times 10^{-4}i$. As the imaginary effective index for the TM hybrid mode is greater than the normal supported TE mode, the TM polarisation undergoes greater absorption, thus polarising the input light. This effect is indeed observed in the reflection spectra of the fabricated device for mm lengths.

7.3 Fabrication

In this work local heating was realised through the use of a nichrome filament, which was deposited using a standard photolithographic technique and e-beam

sputtering system. As previously discussed in Chapter 3 photolithography is an optical means for transferring patterns onto a substrate, in this instance a heating filament was aligned over a pre-DUW grating. The fabrication process involved in this lift-off technique is depicted in Figure 7.3.

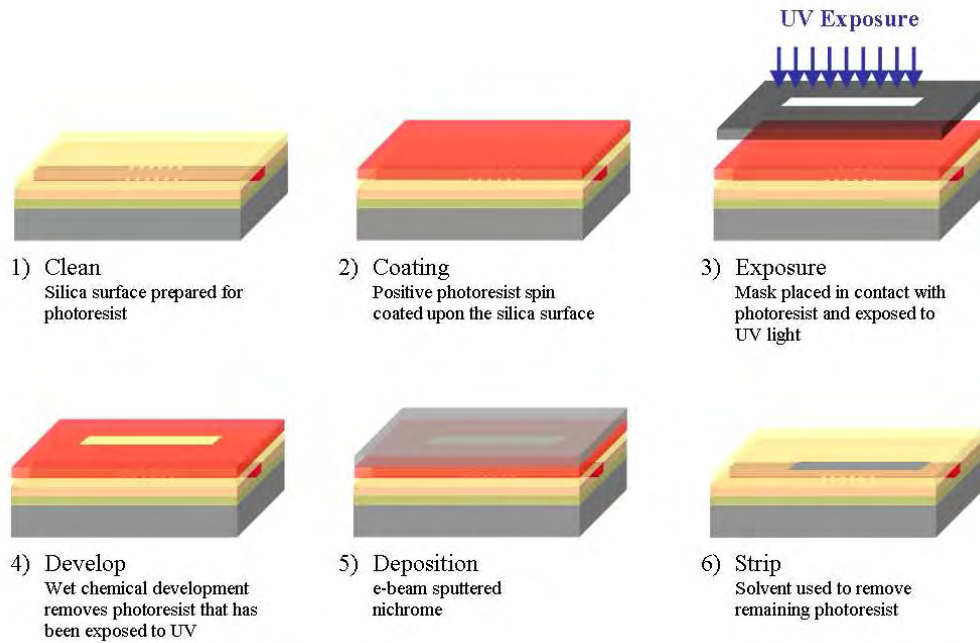


Figure 7.3: The photolithography technique

Firstly the pre-diced wafer was cleaned of contaminants and degreased, using solvents and distilled water. Subsequent to this cleaning a prebake step was required in order to evaporate solvent residue. Prebaking was done in a convection oven at 100°C for 20 minutes. A positive photoresist was spin-coated to an even thickness of $1\mu\text{m}$, upon the wafer.

Using a contact mask aligner the filament design depicted in Figure 7.4 was aligned over the Bragg grating. Subsequent UV exposure of the design resulted in the decomposition of a development inhibitor within the photoresist, such that on exposure to developer solution the photoresist in the exposed area dissolved.

To stabilize and harden the developed resist a post-bake stage was made. The sample was then placed into an e-beam sputterer where nichrome was deposited. Swilling the device after sputtering removed the remaining photoresist and the nichrome which lay upon it, leaving a single heating element remaining.

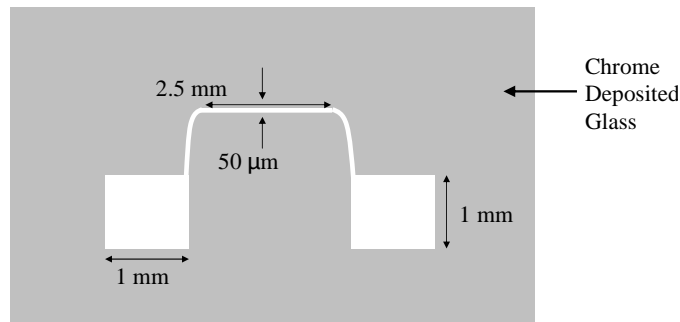


Figure 7.4: The specification of the heating filament

While alternative materials such as gold and chromium could have been used as a heating filament nichrome was chosen as it has a moderately large resistivity for a conductor and less readily oxidises.

The filament widths tested were $25\ \mu\text{m}$, $50\ \mu\text{m}$ and $100\ \mu\text{m}$ wide, with approximate thicknesses of $400\ \text{nm}$. As a thinner filament allows a more localised heat delivery, and the $25\ \mu\text{m}$ filament was observed to burn out before a substantial tuning range could be achieved, a $50\ \mu\text{m}$ filament was used in the following experiments.

The two devices fabricated were taken from two different types of wafer, one with an FHD overlaid layer and one without. Both samples had a transverse width of $10\ \text{mm}$ and length of $20\ \text{mm}$. A set of four Gaussian apodised Bragg gratings of $2\ \text{mm}$ length and separated by $1\ \text{mm}$ intervals were UV written into each device. The bandwidth of the gratings was $1\ \text{nm}$, corresponding to $125\ \text{GHz}$ in the C band. It must be noted that this is too large for DWDM applications, but could be made narrower for future commercial realisation.

The final device, illustrated in Figure 7.5, was V-groove pigtailed and mounted on an aluminium block. Thermal heatsink compound was placed between the silicon wafer and the thermal reservoir (aluminium block) to improve the thermal conductivity. The device also featured a printed circuit board which was glued onto the nichrome terminals using conducting silver epoxy.

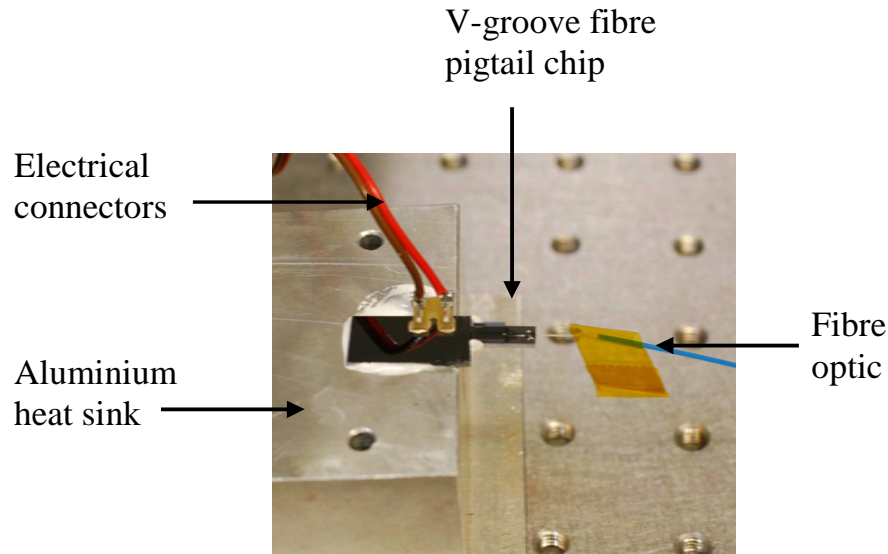


Figure 7.5: The thermal tuning device

7.4 Non-Polarising Filament

For the non-polarising geometry a $16\text{ }\mu\text{m}$ FHD overlaid layer separates the nichrome filament and the grating. The total thickness of the device is 1.04 mm and has a total silica thickness $39\text{ }\mu\text{m}$. The deposited filament has a thickness of 400 nm and a total resistance of $1.16\text{ k}\Omega$.

Maximum tuning of the device occurred when the nichrome filament was dissipating 2.4 W of power. This resulted in a spectral shift of 1.23 nm , illustrated in Figure 7.6. This corresponds to a 154 GHz shift in the C band, which is over three times a typical 50 GHz DWDM channel. The thermal response of the grating is known to be $10\text{ pm}^\circ\text{C}^{-1}$, meaning 154 GHz of tuning is the result of $123\text{ }^\circ\text{C}$ temperature change in the core. To obtain the desired 50 GHz of tuning for DWDM applications only a $40\text{ }^\circ\text{C}$ temperature change is required in the core.

By setting the central wavelength of a tunable laser to the full width half maximum point on the Bragg grating spectra the response time of the device was measured, as illustrated in Figure 7.7. A square wave signal with a peak of 24 V and trough of 0 V was supplied to the filament with a frequency of 1 Hz . The rise time of the supply was $\sim 0.2\text{ }\mu\text{s}$, as measured from a digital oscilloscope. This corresponded to a maximum dissipated supplied power of 0.5 W and spectral shift of 0.26 nm . Figure 7.7 shows an exponential decay in reflected laser power from the grating as the filament is switched on. This is due to the central wavelength of the grating

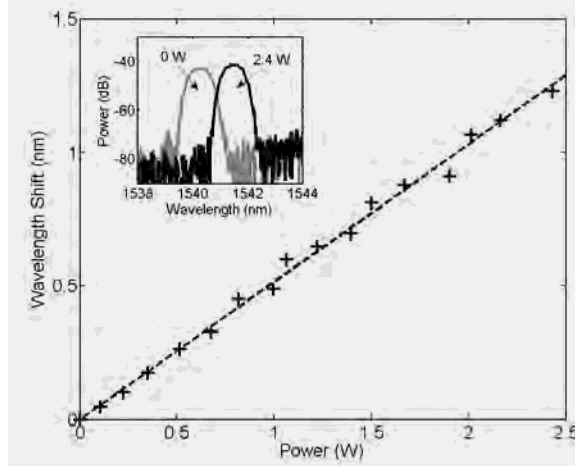


Figure 7.6: Thermo-optic tuning curve in relation to the power supplied to NiCr filament

response being tuned to higher wavelengths. The time response of this effect is 1.02 ms. This value is comparable for both switching the filament on and off.

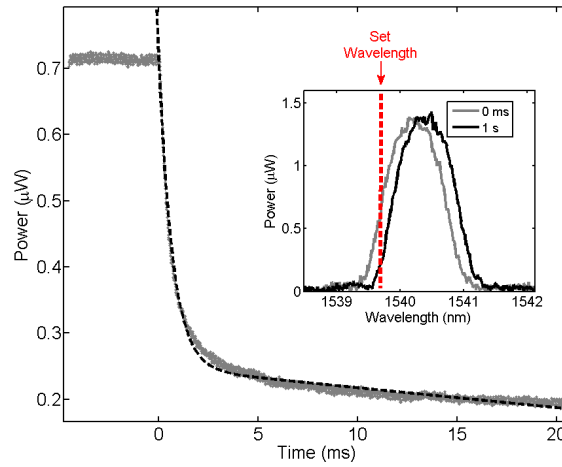


Figure 7.7: Response time for a set wavelength, in a thermo-optic tuned Planar Bragg Grating

Placing a cold plate, set to 10 °C, in contact with the silicon reduced a small bulk heating/cooling effect observed after the initial local heating/cooling took place. The time constant of this effect was 1 s. The tuning efficiency at this temperature was 65 GHzW^{-1} , as compared to 54 GHzW^{-1} without the presence of the cold plate.

Bulk heating can be controlled by placing the device on a cold plate and manipulating the cold plate's temperature. This process reduces bulk heating through

increasing heat flow between the heat sink and the filament, as a result of a larger thermal gradient. Heat flow between the filament and heat sink can also be increased by reducing the thickness of silica and/or silicon. The following section shall reduce bulk heating by altering the geometry of the silica-on-silicon device. The considered device does not reduce the thickness of the silica or silicon but is such that the overclad of the silica is removed and an underclad of equal thickness replaced. This means that filament is in direct contact with the grating and thus more efficiently heats the grating. Due to the improved efficiency a lower temperature gradient between the filament and heat sink is required to achieve the same level of tuning, thus reducing bulk heating effect at higher tuning ranges. It must be noted that the presence of the underclad acts as a control in these experiments (i.e. the effect not being a result of the silica thickness) and future devices can remove this layer.

7.5 Polarising Filament

For the polarising geometry the total thickness of the device was 1.04 mm and a total silica thickness of 40 μm FHD. The deposited filament had a thickness of 350 nm and a total resistance of 1.15 k Ω .

Both polarising and non-polarising devices used a similar filament construction. As a dissipated power of 2.4 W resulted in the burning out of the filament, the following experiments did not exceed a power dissipation range of 1.3 W. At this power the polarising device displayed 1.06 nm of tuning, illustrated in Figure 7.8.

The tuning efficiency of this device is 102 GHzW⁻¹ which is a 60% increase in efficiency compared to the non-polarising device. Potentially the device can be tuned up to 1.96 nm if the maximum operating current is taken.

Tuning of a single 50 GHz channel corresponds to 0.4 nm of tuning at 1550 nm wavelengths. Tuning of over one entire channel is depicted in Figures 7.9 (a) and (b) for a non-polarising and polarising device respectively. The instantaneous tuning of both devices is of the order ~ 1 ms. However, due to the non-polarising geometry having a lower tuning efficiency an additional 0.4 W is required to tune the grating by the same amount. As greater powers are supplied a bulk heating effect is observed, which is absent for the case of the more efficient polarising de-

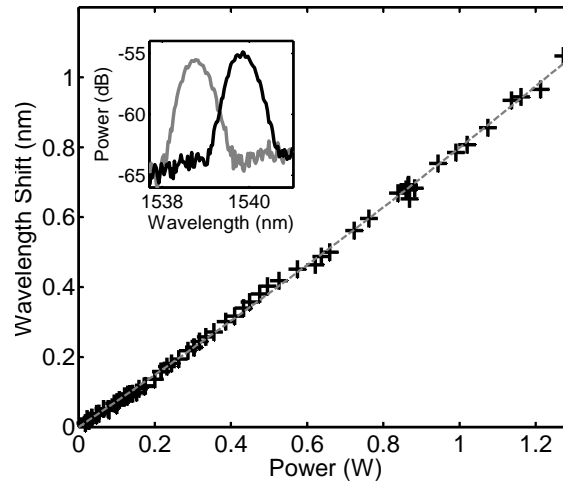
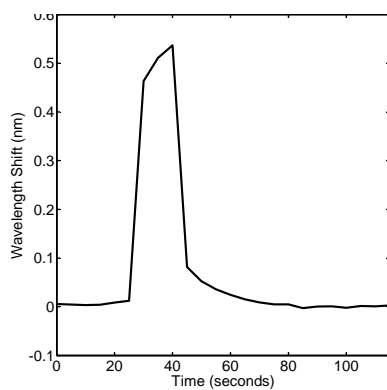


Figure 7.8: The tuning range of a toplless device

vice.

(a)



(b)

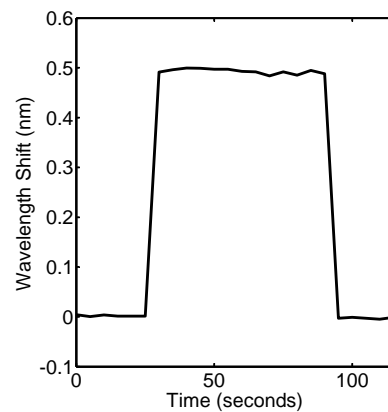


Figure 7.9: The response of thermal tuning chips showing (a) overlaid geometry showing bulk heating and cooling (b) a device without an overlaid showing negligible bulk heating and cooling for a similar tuning range

An interesting effect that was discussed in Chapter 4 is that TE modes, with a metal overlaid, are insensitive to index change. This is illustrated in Figure 7.10 where the tunable grating shows no sensitivity, but the other gratings without a metal clad do. As all of the chip, apart from the locations under the filament are sensitive to the analyte, a specific analyte can be selected to give athermal control on the chip [155]. That is to say, if the refractive index response of the analyte is of opposite magnitude to that of silica and of sufficient magnitude, the intermodal

dispersion can counter-act the fractional change in pitch of the grating. Interestingly, this effect would only affect the areas of the chip that are not covered with a filament. This could potentially allow circuit structures with thermal control to be more tightly packed.

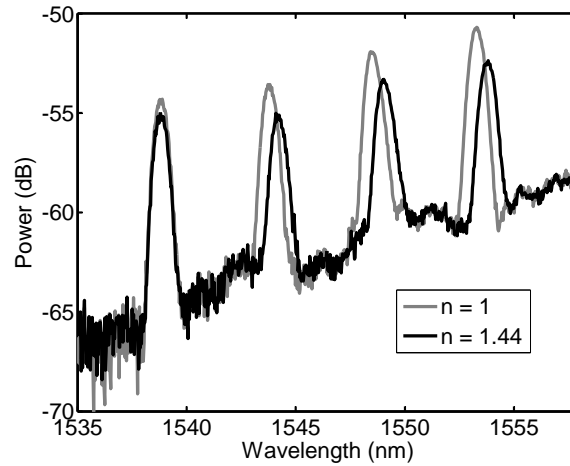


Figure 7.10: The spectral response of four gratings of TE polarisation in a top-less sample under two different refractive index overlays. The lowest wavelength reflection peak has a thick NiCr overlayer between the grating and the exposed index.

7.6 Conclusions

The fabricated devices demonstrated a tuning capability of over two DWDM channels, the degree and speed of tuning indicates potential application in dynamic optical networks, as an optical add-drop multiplexer.

So far the heating elements have been placed parallel to the grating length. However, future devices may consider placing multiple heating elements perpendicular to the grating such that their individual tuning would manipulate the grating chirp.

Future devices may also consider the use of trenches, similar to those considered in Chapter 4, to manipulate heat flow making the devices more effective and efficient. Similar concepts have been previously introduced by Kasahara et al to improve device efficiency of a thermo-optic switch [156].

Chapter 8

Multimode Interference Device

8.1 Introduction

The Multimode Interference (MMI) component is a useful building block in photonic integrated circuits, with many practical applications [157]. These include 3 dB couplers, Mach-Zehnder interferometers (MZI), ring lasers, and optical switches. The advantages they have include superior performance, a small device footprint and an excellent tolerance to polarization and wavelength variations [158].

MMI based components predominantly operate in the index guiding regime, which has been explained in Chapter 2. It has been found that when direct UV writing MMI devices through raster scanning out diffusion [4] and proximity effects [159] become problematic. As discussed in earlier chapters, out diffusion is time dependent. The time taken to fabricate a raster scanned MMI device is entirely dependent upon the dimensions of the MMI device desired and intensity of the laser. Using typical scan speeds of 1 mm/min for a 100 μm by 2.5 mm MMI device would require approximately 100 minutes to fabricate. OH-flooding a sample prior to UV writing or cooling a sample during UV writing can be implemented to reduce the effect of out-diffusion. However, OH-flooding has an associated extrinsic loss increase and cooling a sample has associated complications when applied to a dual beam configuration, as discussed in Chapter 3.

This chapter presents theoretical direct UV written MMI devices that potentially reduce out diffusion and proximity effects acting in the guiding MMI area as well as reducing the level of excess loss. Measurements from proof of principle devices

are presented and fabrication considerations highlighted.

The novel device operates in a leaky mode regime, reducing excess loss by optimising an interference based waveguide concept. To develop the concepts behind this novel device the accepted theory for guided mode based MMI components and interference based waveguides needs to be discussed.

8.2 Theory

The theory of MMI devices is extensively covered in works by Okamoto [27] and Soldano [157], which are considered good foundation stones in MMI literature and shall be summarised in this section.

Generally MMI designs are based on waveguides in the guided mode regime (also known as the TIR regime) [157]. However, interest in making gas and liquid based waveguides has directed some research towards reducing excess loss in leaky modes though interference guiding [160]. The purpose of this section is to outline the theory of MMI devices then apply these concepts to interference based waveguides.

8.2.1 Multimode Interference Coupler

The basic concept of an MMI device is that it is a large waveguide and so can support many modes. MMI devices are three dimensional constructions but for analysis can be reduced to a two dimensional problem, by using the effective index method [27]. To inject and remove light a number of access waveguides are placed at the beginning and end of the MMI device, illustrated in Figure 8.2.1. Such a structure is known as an $n \times m$ MMI device, n being the number of input and m the number of output channels, thus Figure 8.2.1 illustrates a 1×4 MMI.

The MMI section has a Length L_{MMI} and a width W_{MMI} . As treated throughout this thesis the coordinate axes are defined such that propagation is along the x_1 direction. The device operation consists of an input field located at $x_1=0$, which acts to excite each of the guided slab modes by various amounts. Assuming such a slab structure supports J modes numbered $j = 0, 1, 2, \dots, (J-1)$, with propagation constants

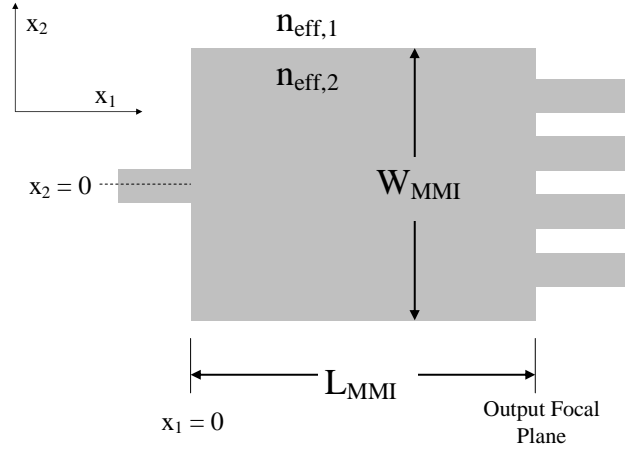


Figure 8.1: The two dimension representation of an MMI device

β , defined as

$$\beta_j = k_0 n_{eff}^{(j)} \quad (8.1)$$

where $n_{eff}^{(j)}$ is the effective index of the j^{th} mode and k_0 is the free space propagation constant. Each mode propagates through the slab in the x_1 direction, with a different velocity. For the case of a $1 \times n$ symmetric MMI coupler, only even modes are excited in the slab. The lateral field profiles of the slab modes thus have the form

$$\psi_j(x_2) = \begin{cases} B_m \exp[q_j(x_2 + W_{MMI}/2)] & x_2 < -W_{MMI}/2 \\ A_m \cos(h_j x_2) & |x_2| < W_{MMI}/2 \\ B_m \exp[q_j(x_2 - W_{MMI}/2)] & x_2 > W_{MMI}/2 \end{cases} \quad (8.2)$$

where for convenience

$$h_j^2 = k_0^2 n_{eff,2}^2 - \beta_j^2 \quad (8.3)$$

$$q_j^2 = \beta_j^2 - k_0^2 n_{eff,2}^2 \quad (8.4)$$

$$h_j = \frac{(j+1)\pi}{W_{eff}} \quad (8.5)$$

here W_{eff} is an effective MMI width which is greater than the fabricated width and arises due to the lateral penetration depth of each mode into the cladding, in

accordance to the Goos-Hänchen shifts at the waveguide boundaries [161]. Equivalently, this can be inferred through BPM simulation.

At specific lengths along the MMI device the input light distribution is found to be self imaged. The location of this self imaging can be calculated by firstly substituting Equations 8.4 and 8.5 into each other

$$\left(\frac{(j+1)\pi}{W_{eff}}\right)^2 = k_0^2 n_{eff,2}^2 - \beta_j^2 \quad (8.6)$$

this can be rearranged and approximated by a binomial expansion to give

$$\beta_j = \left(k_0^2 n_{eff}^2 - \left(\frac{(j+1)\pi}{W_{eff}}\right)^2\right)^{0.5} \quad (8.7)$$

$$\approx k_0 n_{eff} - \frac{(j+1)^2 \pi \lambda}{4 W_{eff}^2 n_{eff}} \quad (8.8)$$

Considering the propagation function and Equation 8.8 it can be shown that self imaging will occur at periodic lengths of [27]

$$L_{MMI} = \frac{n_{eff,2} W_{eff}^2}{\lambda} \quad (8.9)$$

It is understood [27] that N equally spaced images occur at lengths given by

$$x_1 = L_{MMI}/N \quad (8.10)$$

which is true for any integer.

MMI components are currently being realised under leaky mode operation using interference based waveguides. Interference based regimes can use antiresonance reflection [41] [160] [162] or photonic bandgap mechanisms [163] [164] to quasi-guide light. It must be noted, that the formulism derived for guided mode MMI devices hold true for leaky mode MMI devices. The presented MMI device operates using an antiresonance based waveguide structure to quasi-guide light.

8.2.2 Antiresonance Based Waveguides

Antiresonance based waveguides reduce the leakage of energy from a waveguide structure by incorporating high and low refractive index cladding layers of correct thickness as proposed by Duguay et al [162]. The cladding layers behave as Fabry Perot reflectors which can be composed of single or multiple elements. This acts to suppress energy leakage of a certain mode. Such structures are labelled as Antiresonance Reflecting Optical Waveguide (ARROW) components.

To derive the conditions for resonance or antiresonance, it is best to consider geometrical optics. A plane wave characterised by wavevector \mathbf{k} will replace each mode in this instance. The components of which are β and u , as illustrated in Figure 8.2.2.

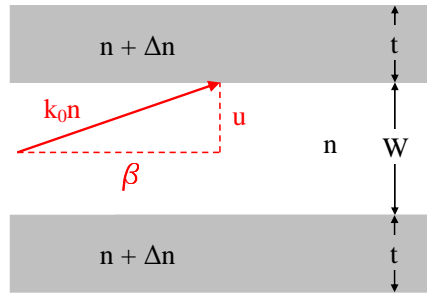


Figure 8.2: Waveguide based upon ARROW principle

If the thickness of the ARROW element (shaded in grey in Figure 8.2.2) is considered, a round trip within it accumulates a phase ϕ expressed as

$$\phi = 2tu + \phi_B \quad (8.11)$$

As illustrated in Figure 8.2.2, t is the thickness of the elements of the waveguide and u is the perpendicular component of a wavevector. ϕ_B is due to the boundary reflections, equal to π , for our single element case. Now, if ϕ is an even multiple of π then the wave interferes constructively with itself and is in resonance with the element. Likewise for an odd multiple of π , the plane wave is in antiresonance. After mathematical derivation from Equation 8.11 the analytical solutions for constructive and destructive resonance become of the form [165]

$$t = \frac{m\lambda}{4(n + \Delta n)} \left[1 - \left(\frac{n}{(n + \Delta n)} \right)^2 + \left(\frac{\lambda}{2(n + \Delta n)W} \right)^2 \right]^{-0.5} \quad (8.12)$$

where m odd corresponds to optimised low loss and m even, high loss.

An issue with the ARROW device is that its antiresonance is optimised for an arbitrary length of waveguide. Considering a $1 \times n$ MMI structure, from the input waveguide the light diffracts out, becoming incident with a wall at varying wavevector components u , dependent upon the distant from the input. The following work develops ideas that manipulate the ARROW structure such to reduce the energy leakage for this diffracting mode.

8.3 Antiresonance DUW MMI Device

Previous work to fabricate MMI devices using DUW has been undertaken by Knappe et al [4] and involved raster scanning the device with the UV laser spot, illustrated in Figure 8.3.

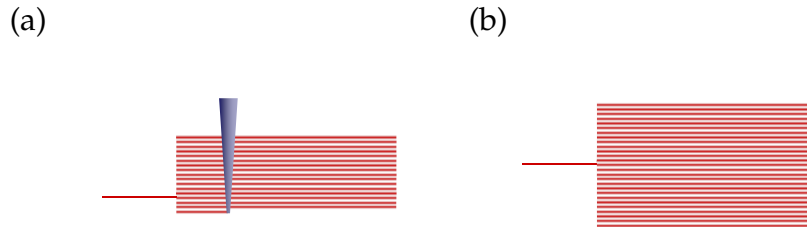


Figure 8.3: Schematic of a raster scanned DUW device illustrating (a) fabrication (b) complete structure used in [4]

Several problems arise as a result of this raster scanning technique, including a significant level of out-diffusion arising from its associated long writing time. As an antiresonant structure only requires side wall definition it has a much reduced writing time and hence reduced level of out diffusion. It is also believed that proximity effects when UV writing produce a non homogenous index structure [159]. Again as the antiresonant structures are outside the main body of the device and not integrally part of it, the effects of proximity writing on the basic MMI operation are reduced.

The simplest way of achieving an antiresonance structure would be to write 'single element' boundaries for the MMI, illustrated in Figure 8.4.

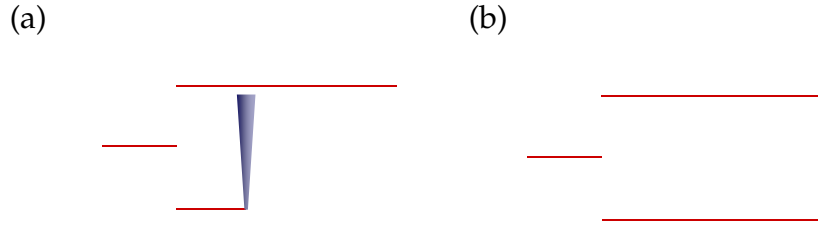


Figure 8.4: Schematic of a single element DUW device illustrating (a) fabrication (b) complete structure

An improvement to the single element construction would be to have multiple elements of constant period illustrated for five elements in Figure 8.5.

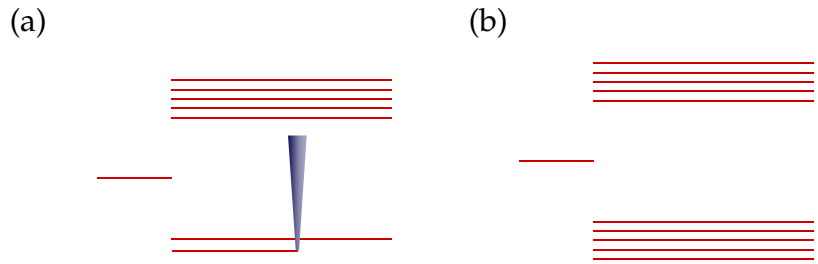


Figure 8.5: Schematic of a five element DUW device illustrating (a) fabrication (b) complete structure

Utilising the 2D control of the translation stages it is possible to fabricate a device with 'locally optimised' period, a concept that is difficult to realise using traditional ARROW fabrication processes. Due to the low index contrast associated with DUW, this local optimisation becomes more essential.

The following work considers the optimisation of a 1×4 MMI device using the BPM algorithm outlined in Appendix A. Optimum designs for single, multiple and locally optimised elements shall be addressed.

8.3.1 Single Element

As the real refractive index profile of the UV written channel is unknown two different constructions for the single element side walls were tested, one was a top-hat index profile and the other a Gaussian index change, as illustrated in Figure

8.6. Both simulations defined an imaginary refractive index, at the boundaries of the simulation, which did not overlap with the MMI structure, such to make the boundary conditions absorbing¹.

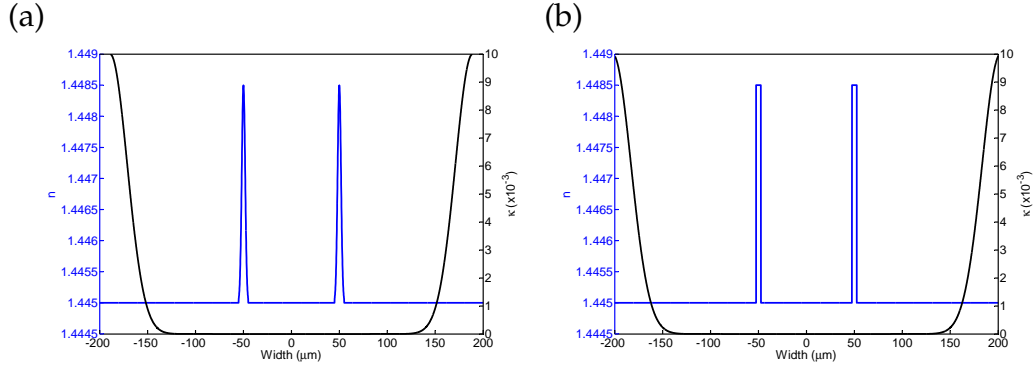


Figure 8.6: The two tested index profiles for single element operation depicting the real n and imaginary κ constructions for, (a) Gaussian elements and (b) top-hat elements

Figure 8.7 depicts the BPM simulation of the index construct in Figure 8.6. Due to the top-hat walls having discrete reflection locations the intensity pattern is sharper. To compare the effectiveness of the simulation, the end face outputs of both the Gaussian and top-hat simulation were compared to a fabricated device.

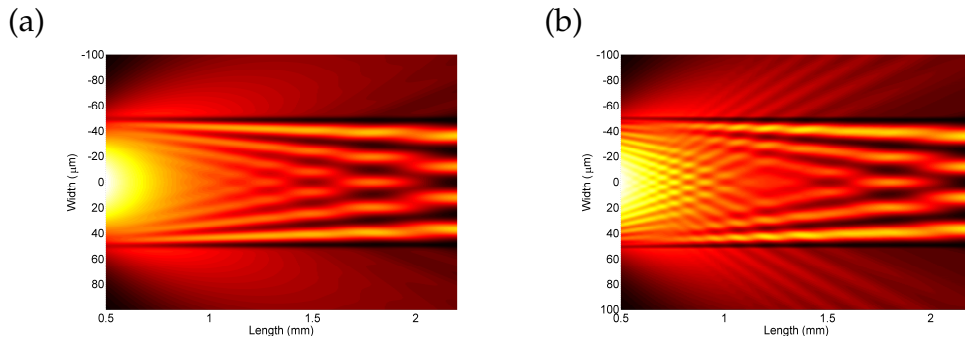


Figure 8.7: The field intensity of a 1 x 4 single element MMI device as simulated by BPM, considering (a) Gaussian and (b) top-hat elements

The device was fabricated into a non index matched silica-on-silicon wafer, which had a high concentration of germanium in the core allowing for single mode confinement in the lateral direction. The dual beam set-up was used to write a 100 μm by 2.2 mm single element MMI structure, with a fluence of 15 kJcm^{-2} . Prior to UV writing the samples were side polished and hydrogen loaded at 120 bar for

¹Technically these should be described as absorbing walls and not absorbing boundary conditions

two weeks. The MMI device was written up to the polished edge and viewed in transmission. To aid characterisation alignment a grating was written in the input waveguide. For alignment of light out of the device a HeNe was launched into the input waveguide and observed in transmission through coupling into a SMF-28 fibre. After HeNe alignment a tuneable laser set at 1550 nm was used to launch light through the device, as illustrated in Figure 8.8.

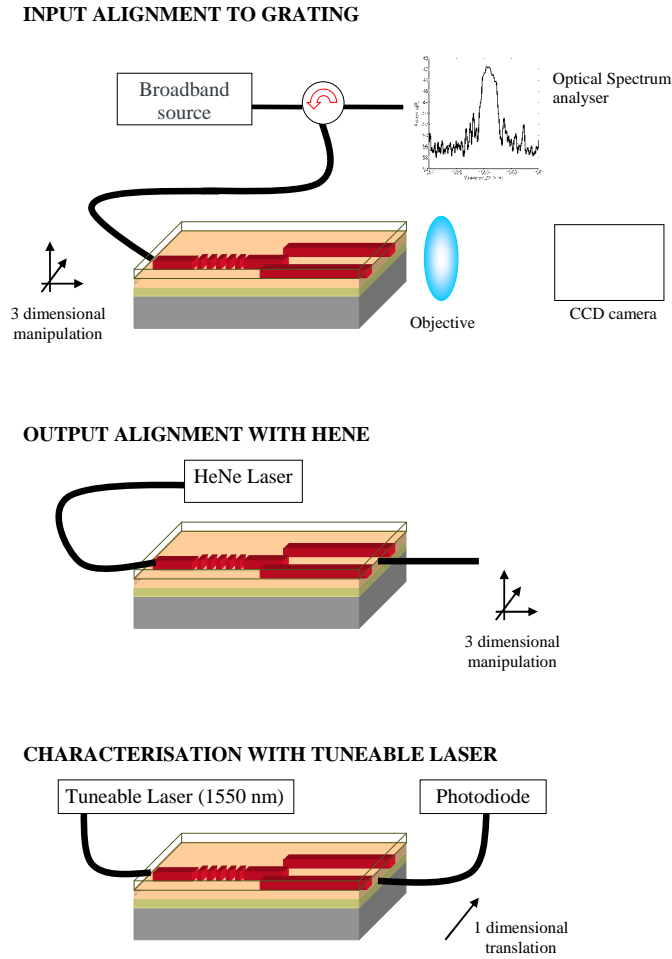


Figure 8.8: Characterisation and alignment set-up of the direct UV written MMI device

The power coupled into the fibre was measured at different lengths along the output face. To compare the simulated and empirical data the simulated data was convoluted with a Gaussian, which represented the scanned fibre in the empirical measurement, illustrated in Figure 8.9.

There are small deviations between the simulated and empirical data sets, illustrated in Figure 8.9. The top-hat elements appear to give an intensity profile that

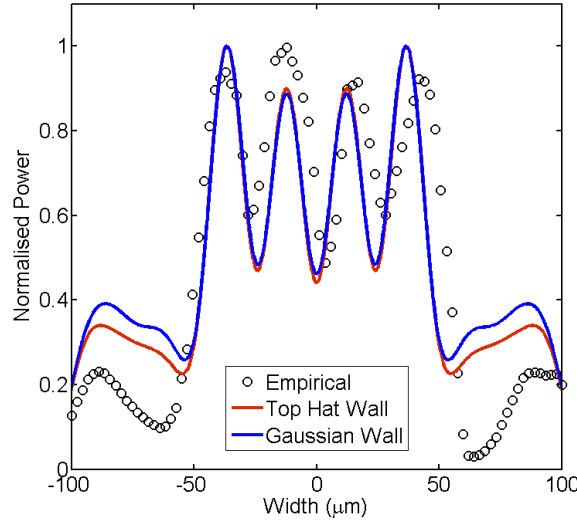


Figure 8.9: An endface scan of a fabricated 1x4 single element MMI device compared with BPM simulation of tophat and Gaussian side walls

is closer to that empirically measured and so justifies use of it as the index profile in the following simulations.

The single element device can minimise excess loss by manipulating the index change² and element width, as simulated in Figure 8.10 (a). The form of this graph can be understood from Equation 8.12, which is plotted graphically in Figure 8.10 (b). Note the maxima and minima of the simulation coincide well with the analytical values. In addition as the index contrast reduces so too does the magnitude of the Fresnel reflections, as seen in Figure 8.10 (a) shows a greater blurring between the resonant and antiresonant conditions at lower index contrasts.

The lowest excess loss indicated from Figure 8.10 (a) is 25% or 1.25 dB. However, it must be noted that these regions of low loss coincide with regions of high index contrast, which are not achievable using the DUW technique. For the purpose of this work an index increase of $<5 \times 10^{-3}$ shall be considered. To optimise element thickness for this index ceiling fabrication practicalities have to again be considered.

The optimum element thickness can be realised by either varying the focus of a single beam set-up, or encoding multiple passes, which can be achieved by the single or dual beam set-up. Defocusing the single-beam setup to achieve optimum

²It must be noted that the element index is considered as the increase in n_{eff} which, although is similar to, is not the same as saying the induced index change of the channel.

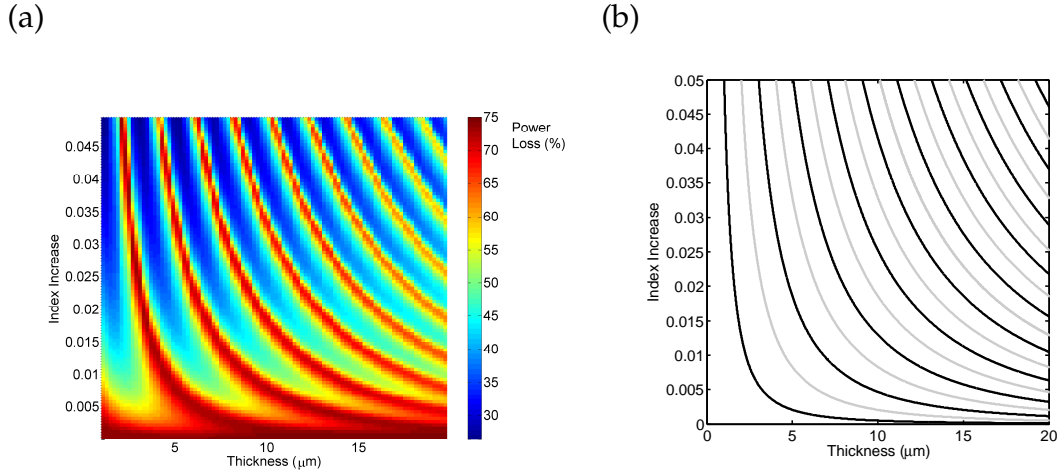


Figure 8.10: Optimum channel width and refractive index contrast as (a) modelled by BPM simulation (b) analytical evaluation from Equation 8.12 where the black lines indicate low loss (antiresonant) and grey lines high loss (resonant)

element thickness has an associated fabrication difficulty, more importantly single-beam operation removes the potential for incorporating Bragg gratings in device design. The use of multiple passes has additional complexities in fabrication due to proximity effects. Assuming the written channel of the cross beam setup has a fixed width of $5 \mu\text{m}$ the optimum index contrast is ~ 0.0035 , which corresponds to a theoretical loss of 4.6 dB.

Considering the two reflection faces of a single element contributing to two effective widths of the MMI the self-imaging lengths as calculated from Equation 8.9 are 9.3 mm 8.4 mm. Figure 8.11 illustrates self imaging occurring between these values.

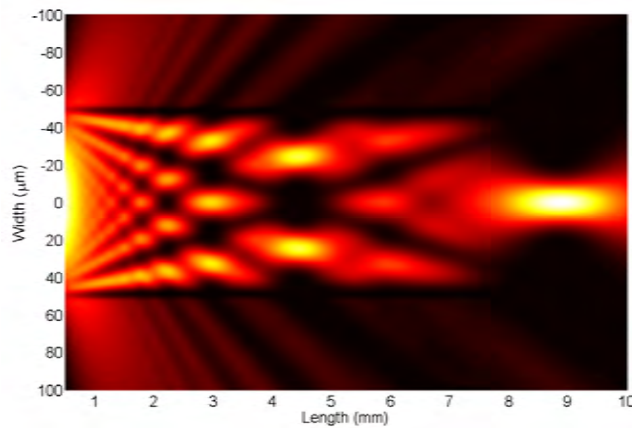


Figure 8.11: A BPM simulation depicting a 1×1 self imaging MMI single element device with index contrast 0.0035 and period $5 \mu\text{m}$

Working with an element width of $5 \mu\text{m}$ and index contrast of 0.0035, multiple elements of constant period will be considered, in order to further reduce loss.

8.3.2 Constant Period

The index profile for a five element constant period device is shown in Figure 8.12 and has an imaginary index part similiar to that in the single element case.

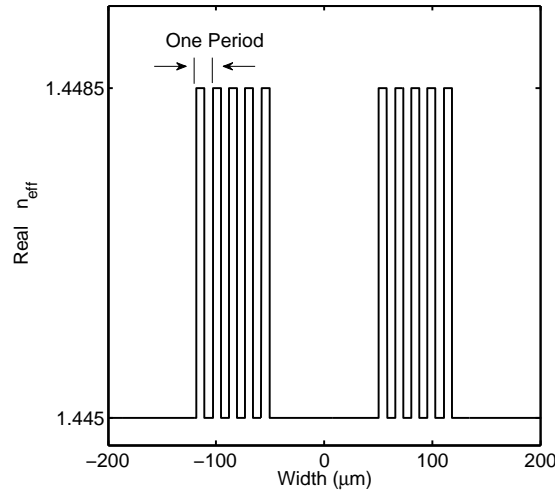


Figure 8.12: The real refractive index construction of a 5 element constant period MMI device

Considering the effect of multiple elements it is observed in Figure 8.13 (a) that as expected further increasing element number can further decrease the excess loss. Due to the fixed length of the device there is little advantage in increasing the period to over 5 elements.

Taking the 5 element device Figure 8.13 (b) illustrates the simulation of loss as a function of period and MMI width such to vary it between 0 and $1/2$ multiples of the period (defined as π). It is observed that there is negligible relation between the phase of the two walls and indeed this is true for a self imaged device.

An optimised and unoptimised five element construct is depicted in Figure 8.3.2, along with the respective losses along the length. For an unoptimised period of $14.3 \mu\text{m}$ (Figure 8.3.2 (b) and (d)) the light can be seen to spill through the elements. In contrast Figure 8.3.2 (a) and shows light filtering back in from the elements as they are under an antiresonance condition. Figure 8.3.2 (c) clearly shows

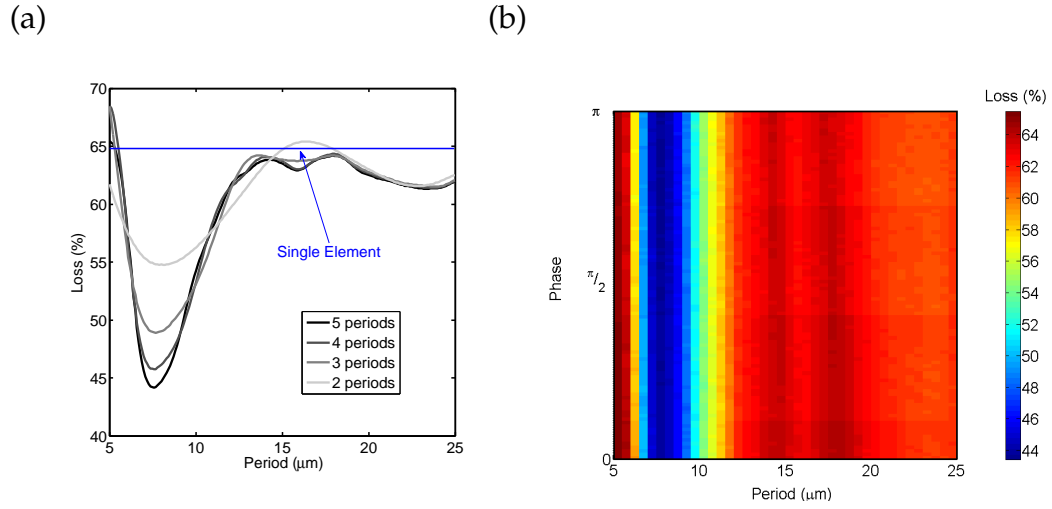


Figure 8.13: The MMI loss dependence for a constant period construct considering (a) different number of periods (the thin blue line representing the loss for a single element) and (b) the relationship between device loss, period and phase for a five element construct

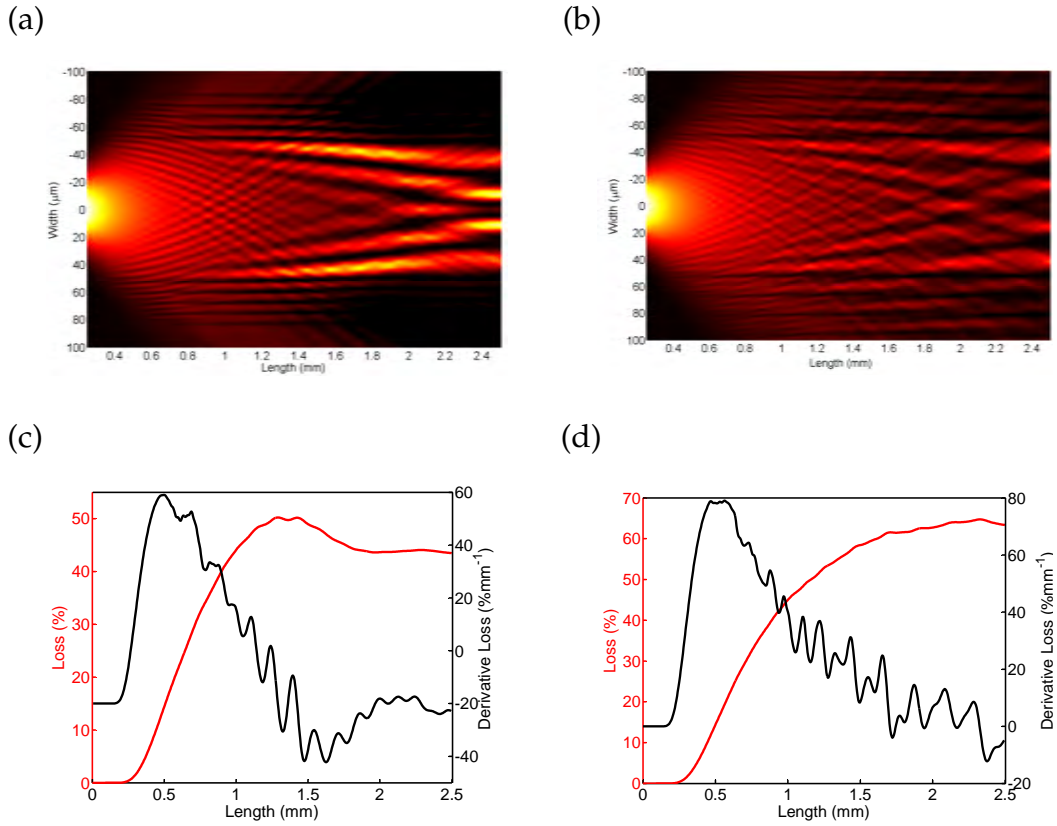


Figure 8.14: BPM simulations showing (a) intensity and (c) loss distribution for optimised five element period of $7.6 \mu\text{m}$ period and (b) intensity and (d) loss distribution for an unoptimised five element period of $14.3 \mu\text{m}$ period

the light filtering back into the device and a reduction in loss. It is also be observed when compared to Figure 8.7 (b) that the multiple element constructs have a larger imaging length. This is due to the multiple elements acting to give a larger effective width of the device. Which in turn makes the self-imaging length greater, as dictated by Equation 8.9.

Considering the five element construct, the optimum period results in a 2.5 dB loss, this is already a significant improvement on the single element device. To further drive down this loss the next construct will be a locally optimised period device.

8.3.3 Adaptive Period

The adaptive period construction was optimised by fitting a third order polynomial equation to the period as a function of the propagation length and a separate third order polynomial to the index contrast. Bounds were set for the period between $5 \mu\text{m}$ and $30 \mu\text{m}$ and for the index contrast between 0 and 5×10^{-3} , such that if the polynomial dictated values higher or lower than these bounds the return value would be the value of the bounds.

The seed values to optimize the polynomial were taken as the optimized constant period and refractive index values previously discussed. The Matlab function `fminsearch`, which uses Nedler-Mead algorithm [166] was then implemented to optimize the polynomial. Table 8.2 indicates the parameters for optimum index contrast, δ , and period, Λ .

$$\begin{pmatrix} \delta \\ \Lambda \end{pmatrix} = \sum_{i=0}^3 \begin{pmatrix} a_i \\ b_i \end{pmatrix} x_1^i \quad (8.13)$$

coefficient \ i	0	1	2	3
a	3.527e-3	1.372e-4	1.205e-4	-2.153e-5
b	2.135e-6	4.840e-3	1.582e-4	-3.639e-3

Table 8.1: The parameters of Equation 8.13, which give minimum excess loss for a 1×4 MMI

The form of the optimisation is given in Figures 8.3.3 (a) and (b).

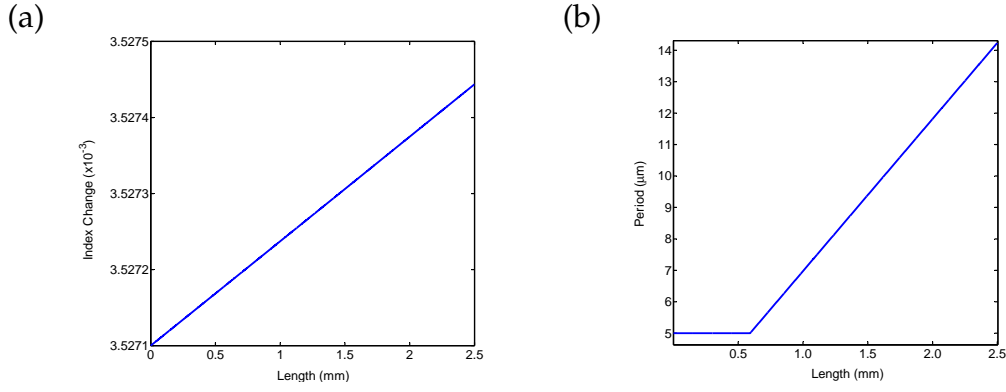


Figure 8.15: The form of the optimised period and index contrast with respect to propagation length along the MMI

The locally optimised period and index is of the form expected from theory. As can be visualised in Figure 8.2.2, for greater propagation lengths the wavevector component, u , is smaller and so the Bragg condition requires a larger period [125]. The picture of this device is more complicated as one obtains subsidiary bounces which also need to be considered. However, it can be appreciated that subsidiary bounces themselves have the same trend. Discrepancy between the optimised period and that suggested by the Bragg condition is believed to be a result of the capped width of the written element, which the period optimises to [125].

Figure 8.3.3 compares the simulated excess loss for a locally optimised MMI device with that of a raster scanned device. The Raster scanned simulation has an index contrast and width equal to the maximum index contrast of the local optimisation and a length of 3.9 mm. The output excess loss for the Raster scanned device is 1.65 dB compared to with 1.61 dB for the locally optimised arrangement. It can be seen that, for the same index contrast the locally optimised device has a lower associated loss! This comes in addition to other benefits such as a reduced writing time and the removal of proximity effects from the functional MMI region.

An interesting observation with the raster scanned device, illustrated in Figure 8.3.3 (d) is that loss appears to increase and decrease along the propagation length of the device, meaning some quantity of light is returning back into the raster scanned section of the MMI. This effect is believed to be the result of the Goos-Hänchen shift, allowing a fraction of the guided light to exist 'outside' the main raster scanned body of the MMI.

Excellent tolerance to wavelength variations is a key feature an MMI device pos-

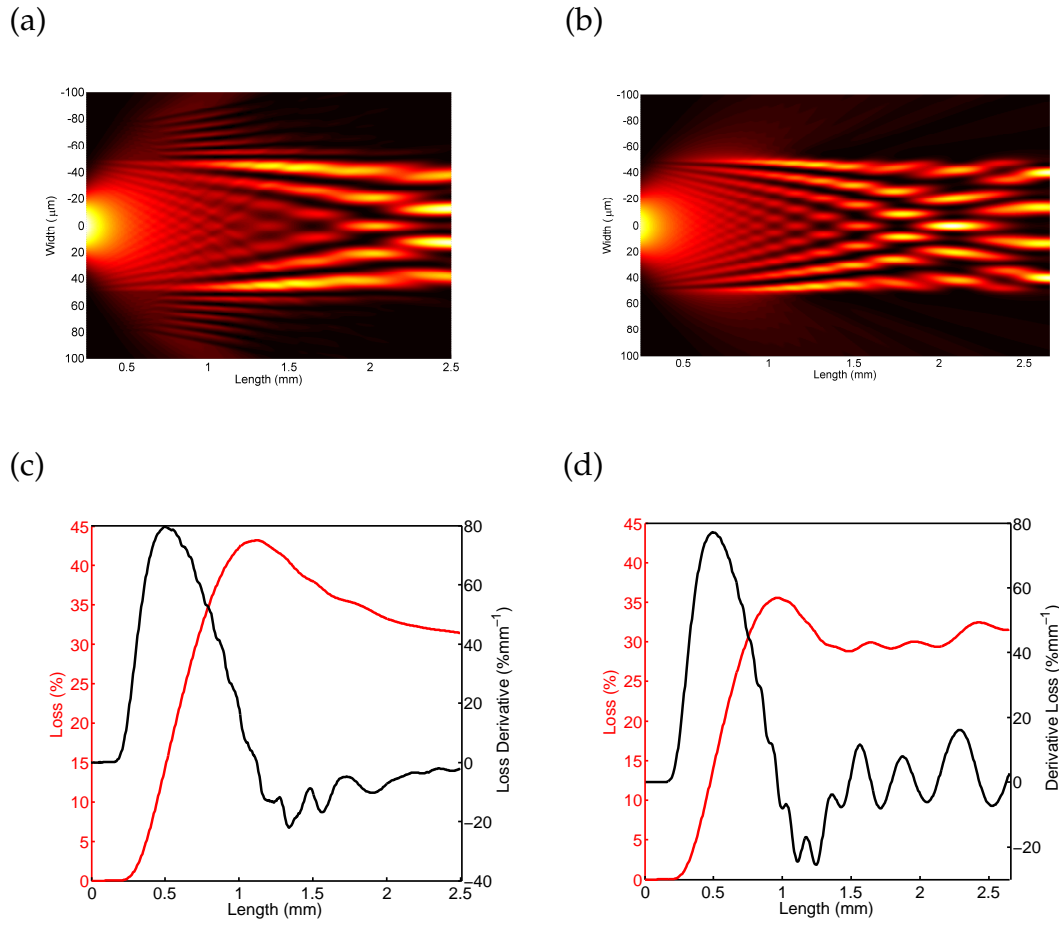


Figure 8.16: BPM simulations showing (a) intensity and (c) loss distribution for a locally optimised device and the (b) intensity and (d) loss distribution for a Raster scanned device

sesses. The adaptive period technique should thus show a comparable spectral loss variation and indeed this was observed through simulations, as illustrated in Figure 8.3.3. The adaptive period device is optimised to 1550 nm wavelengths and as can be seen from Figure 8.3.3 values that deviate from this optimised wavelength have an increased loss.

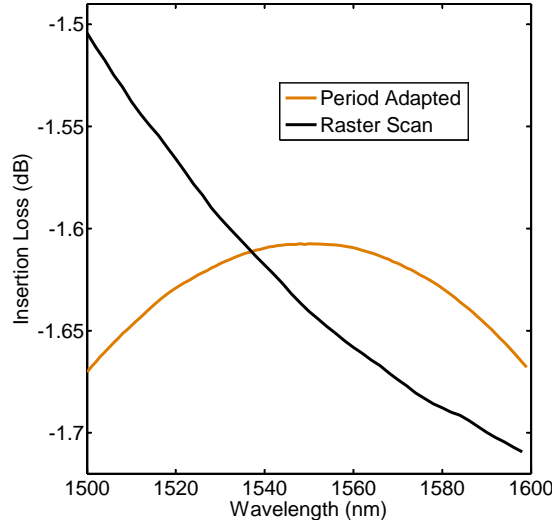


Figure 8.17: A simulation of excess loss with respect to variations in wavelength, for an MMI device optimised about 1550 nm wavelengths

The raster scanned device has a comparable spectral loss variation to the adaptive period, over the 200 nm spectral range simulated. However, the trend of the spectral losses is different. For the raster scanned device higher wavelengths show an increase in loss whilst lower wavelengths show a decrease in loss. This can be understood from Equation 8.9, reducing the wavelength, λ , acts to increase the required length, L_{MMI} , of the MMI device to achieve the same fold symmetry. As the length of the MMI device set is shorter than the length required to achieve the desired fold of symmetry one is effectively sampling the power 'upstream' thus there is less loss. This argument is conversely true for longer wavelengths.

It must be noted that due to the limitation of index contrast the optimised index has only a small influence on optimisation. Having control over the width of the written elements may further reduce the excess loss and widening the improvement it has over the raster scanned device.

8.4 Fabrication Considerations

Single mode confinement in the x_3 dimension of the device is required for optimum coupling between the single mode input and output waveguides. So far it has been assumed that there is single mode confinement in the x_3 dimension, however as the three silica layers in the conventional wafer design are index matched, multimode operation is observed in the x_3 dimension, as all three layers act to form a $40\text{ }\mu\text{m}$ guide. To achieve single mode confinement wafer fabrication requires non index matched layers, the core layer of which having a higher refractive index, as a result of higher germanium concentration. Such wafers have been fabricated, as shown in Figure 8.18, and indeed show single mode confinement in the x_3 dimension, as shown in Figure 8.4.

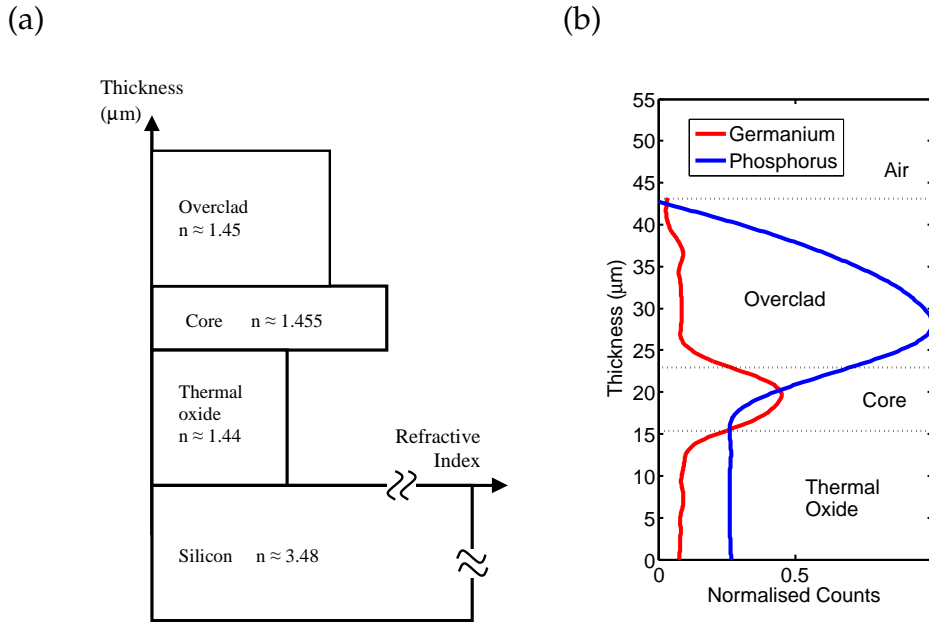


Figure 8.18: (a) Refractive index profile of 0 delta and non 0 delta samples (b) EDX analysis of non 0 delta silica layer composition

For proof of principle device operation single element constructions have been so far fabricated, which corroborate with simulations. Future work shall consider the more complicated multiple element designs, with constant and locally optimised period. It is understood that these designs may have to account for proximity effects that locally alter the refractive index of subsequent written areas, as investigated by Adikan [159].

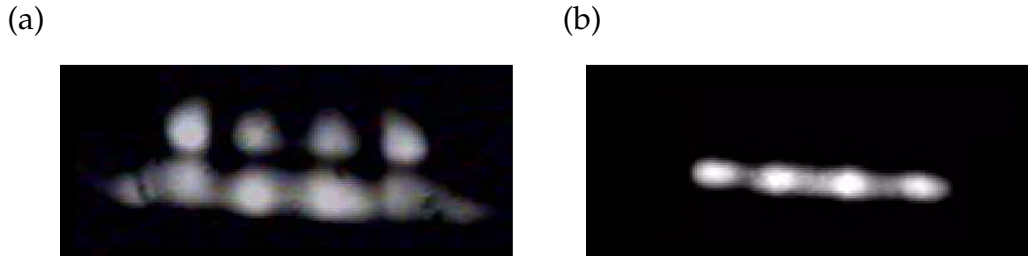


Figure 8.19: Image from a CCD camera of a 1550 nm launch into a polished output face antiresonant DUW MMI (a) index matched layers and (b) high index core layer

8.5 Conclusions

The concept of a locally optimised DUW antiresonant guiding MMI device has been realised. Table 8.2 compares the simulated operation of antiresonance guided structures with a raster scanned device of comparable index contrast.

Design	Device Footprint (mm ²)	Writing Time (Normalised)	Excess Loss (dB)
Raster Scanned	0.265	1	1.65
Single Element	0.231	$\sim 1/50$	4.56
Constant Period	0.374	$\sim 1/10$	2.52
Adaptive Period	0.588	$\sim 1/10$	1.61

Table 8.2: Comparison of three interference based designs with respect to raster scanned device

In addition to the attributes detailed in Table 8.2 these devices have additional degrees of fabrication freedom in that waveguides and gratings can be written within the structures to form new device architectures.

Future work shall implement the theoretical optimum localised designs and consider such devices for sensing applications. Topless indexed matched samples may be best suited for this means as the resulting supported modes are expected to have more power in the measurand.

Chapter 9

Conclusions

This PhD thesis has demonstrated numerous extensions to the potential application of direct UV written structures for OADM applications, novel MMI based power splitters and chemical and physical actuators. Micromachining, etching and sputtering techniques have been implemented to enhance the performance of these devices and realise the implementation of new geometries. The following sections shall summarise the developed devices into telecommunication and sensing categories.

9.1 Telecommunication Devices

The actuation of direct UV written Bragg gratings have been demonstrated, as a potential means for optical add/drop multiplexing in telecommunication networks. Bragg grating actuation was achieved using thermo-optic and strain-optic means.

Through applying localized thermal and mechanical strain maximum tuning ranges of 154 GHz and 311 GHz at 1550 nm wavelengths were respectively demonstrated, which is in excess of a typical 50 GHz DWDM spacing. Although the mechanically tuned devices demonstrate a larger tuning range they also displayed spectral broadening/asymmetry for larger tuning amounts, as a consequence of the mechanical bending and the composite nature of the silica-on-silicon platform. Comparatively, the thermo-optic device did not depict this trend over its tuning range.

Removing the overclad of a locally optimised thermo-optic device, such that the heating filament was in closer proximity to the Bragg grating, gave a tuning efficiency of 102 GHzW^{-1} which is a 60% increase in efficiency compared to a device with a $15 \text{ }\mu\text{m}$ cladding layer. Tuning ranges may be enhanced through the use of grooves to better guide the flow of heat energy in the thermo-optic device, which may allow for a higher efficiency thus giving a higher overall tuning capability.

The mechanically tuned Bragg grating had a stress efficiency of 0.29 nm/N , modifications of the design could utilise piezo-electric actuation. The limit to tuning range for the thermal device is oxidation of the filament. The limit to tuning range for bending was applied the bending moment's position with respect to the crystal planes of the silicon. Mechanically stressing the device such that it is not in line with the planes of the silicon structure may increase the tuning range of the device.

A novel leaky mode MMI power splitter was demonstrated, which used a period adaptive Bragg mirrors to minimise excess loss. The excess loss of the optimised device was modelled to be 1.61 dB , which is an improvement upon a comparable raster scanned device (loss 1.65 dB). More importantly the UV writing time is only $1/10$ th that of a raster scanned device, so can overcome issues of out-diffusion and internal device proximity effects. In addition these devices have a unique degree of freedom as waveguide gratings and structures can be written within the body of the MMI device to form new device architectures.

Sensing devices optimised the chemical as well as physical transduction of a Bragg grating to monitor environmental variations.

9.2 Sensing Devices

Both physical and chemical sensors have been investigated in this PhD thesis. The chemical sensors are based upon refractive index evanescent field sensing techniques. Exposure of the evanescent field has been investigated using top access and a novel side access geometry. The side access geometry is achieved using micromachined groove structures, which form an inherent platform for microfluidic manipulation.

Enhancement layers can be used to increase the sensitivity of a native sensor. The

greatest bulk sensitivity around a refractive index of water can be achieved for TE polarisation. Considering a 50 nm titania overlay the corresponding sensitivity is $1 \times 10^5 \text{ pmRIU}^{-1}$. The surface sensitivity of a 10 nm surface change is an order of magnitude less than this value.

The monitoring of differential pressure and flow has been realised through the use of thin ($\sim 40 \mu\text{m}$) silica membranes, in which Bragg gratings are inherently defined. It was demonstrated that an integrated device containing temperature, chemical, pressure and flow sensing Bragg gratings can be integrated upon a single chip. This gives a greater dynamic range for future lab-on-a-chip based devices.

Chapter 10

Future Work

10.1 Plasmon Enhanced Sensing

In Chapter 4 it was found that dielectric and metallic enhancement layers can improve the sensitivity of a native device. An optimised thickness of metal enhancement was computationally observed to display a lower potential sensitivity than an optimised dielectric enhancement for both bulk and surface sensitivity. It has been theoretically posed by Nemova and Kashyap [100] that a pure plasmon mode can be coupled using a Bragg gratings wavevector and a plasmon-hybrid mode. It is believed that such a pure plasmon will give a significant improvement of surface sensitivity as opposed to the plasmon-hybrid mode and more importantly enhancements made by dielectric overlayers.

10.2 Low-Mass Transducers

The membrane based Bragg grating devices have proven to be an effective tool in monitoring pressure differentials. Theoretical treatment of the membranes response to buckling and pressure differentials has been understood.

Scope exists to interpret the spectral response of a Bragg gratings and other direct UV written structures inherently defined in alternative membrane constructions, such as bossed membranes for accelerometer based applications [115].

Cantilevers are another low mass structure used in physical sensing. Using the

saw machining technique, detailed in Chapter 4 it is possible to remove sections of silica through to the silicon. Combined with the KOH etching technique detailed in Chapter 6 it is possible for a very small cantilever to be fabricated, illustrated in Figure 10.1.

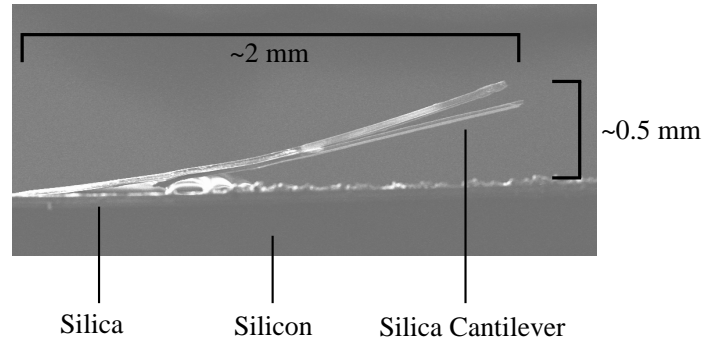


Figure 10.1: A prototype DGW cantilever SEM image from the side of the device

The fabricated cantilever has direct UV written Bragg gratings written along its length. The inserted image in Figure 10.2 depicts the locations of gratings A and B on the cantilever. As the different silica layers have different consolidation temperatures, there are different levels of stresses between them. This results in the cantilever curling up, away from the silicon, thus resulting in a spectral shift of grating's A and B (Figure 10.2).

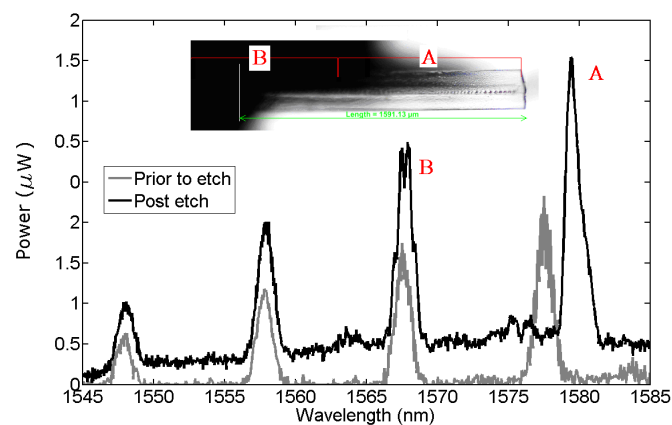


Figure 10.2: A prototype DGW cantilever spectral response of the stress release, a comparison of pre-etch to post-etch

Cantilever-based sensors have received increasing interest over recent years, as they offer a completely new type of miniaturised transducer with both chemical

and physical monitoring capabilities [167]. If the cantilever is mechanically resonated, quantitative and qualitative measurements can be monitored which can be enhanced to monitor a particular measurand through surface manipulation.

10.3 Ultra-Precision Machining

During this PhD the ultra-precision machining of grooves features have been investigated. The authour has demonstrated that surface roughness can be greatly reduced through using rapid thermal annealing processing.

Future devices, machining micron order features into silica-on-silicon wafers, may be viable using. A proof of concept device using a 50 μm saw blade has already been demonstrated, illustrated in Figure 10.3.

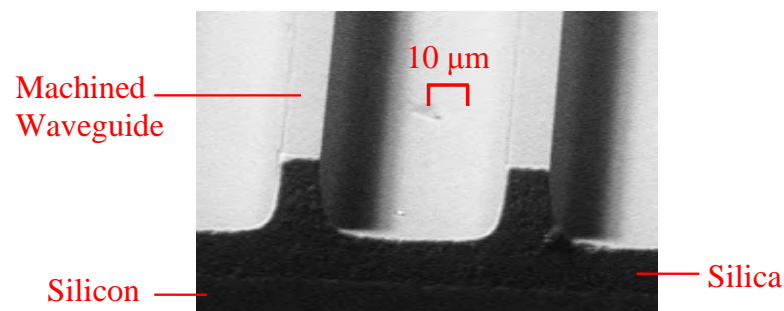


Figure 10.3: Waveguide fabricated using ultra-precision machining technique

The current issues with this process include surface roughness, size and being limited to straight channels. Using precision stages, similar to those applied to the DUW process and air-bearing spindles, practical 2D integrated optical devices may be machined.

The novelty of this approach is that it removes expensive and time consuming cleanroom process such as the use of photoresist and etching. This approach is flexible and creates devices with a quick turn around time for rapid prototyping.

Appendix A

Publication List

The journal and conference proceeding publications arisen from this work.

C. Holmes, J.C. Gates, C.B.E. Gawith, P.G.R. Smith, 'Strain tuning of a composite silica-on-silicon direct ultraviolet written planar Bragg grating', *Optical Engineering*, 49 (4), (in press), 2009.

C. Holmes, D. O. Kundys, J. C. Gates, C. B. E. Gawith, P. G. R. Smith, '150 GHz of thermo-optic tuning in direct UV written silica-on-silicon planar Bragg gratings', *Electronic Letters*, 45 (18), pp.954-956, 2009.

C. Holmes, H. E. Major, J. C. Gates, C. B. E. Gawith, P. G. R. Smith, 'Period Adapted Bragg Mirror Multimode Interference Device', *CLEO/QELS 2009*, Baltimore, 1-7 June 2009.

C. Holmes, H. E. Major, J. C. Gates, C. B. E. Gawith, P. G. R. Smith, 'Flow Monitoring in Optofluidic Channels Using Planar Bragg Gratings', *CLEO/QELS 2009*, Baltimore, 1-7 June 2009.

C. Holmes, J. C. Gates, C. B. E. Gawith, P. G. R. Smith, 'Optical Differential Pressure Transducer using Planar Bragg Gratings in an Etched Membrane', *CLEO 2009*, Munich, 13-21 June 2009.

C. Holmes, M.F.R.Adikan, A.S.Webb, J.C.Gates, C.B.E.Gawith, J.K.Sahu, P.G.R.Smith, D.N.Payne, 'Evanescent field sensing in novel flat fiber', *CLEO/QELS 2008*, San Jose, 4-9 May 2008.

J.C.Gates, **C. Holmes**, B.D.Snow, C.B.E.Gawith, P.G.R.Smith, 'UV written evanes-

cent devices fabricated in micro-structured substrates for optofluidics', CLEO/QELS 2008, San Jose, 4-9 May 2008.

J.C.Gates, **C. Holmes**, A.Webb, M.F.R.Adikan, C.B.E.Gawith, J.K.Sahu, P.G.R.Smith, 'Direct UV written waveguides and Bragg gratings in novel substrates', Photonex 07, Coventry, 17 Oct 2007.

M.F.R.Adikan, **C. Holmes**, H.Major, C.B.E.Gawith, J.C.Gates, P.G.R.Smith, 'Direct UV written optical planar devices', Malaysian Research Group International Conference 2006 (MRG-IC2006) Manchester 19-21 Jun 2006.

J.C.Gates, **C. Holmes**, M.F.R.Adikan, C.B.E.Gawith, P.G.R.Smith, 'New geometry for planar UV written refractive index sensors', SPIE Europe Optics and Optoelectronics, Prague, 16-20 Apr 2007.

J.C.Gates, F.R.M.Adikan, **C. Holmes**, C.B.E.Gawith, P.G.R.Smith, 'Lateral groove geometry for planar UV written evanescent devices - new flexibility new devices', CLEO-Europe/IQEC Munich, 17-22 Jun 2007, CE4-4-TUE

P.G.R.Smith, C.B.E.Gawith, J.C.Gates, **C. Holmes**, B.D.Snow, F.R.M.Adikan, 'UV written planar Bragg grating sensors - geometries and applications', Photon '08 Edinburgh, 26-29 Aug 2008.

P.G.R.Smith, C.B.E.Gawith, J.C.Gates, D.M.Kundys, M.F.R.Adikan, **C. Holmes**, H.E.Major, M.Garcia-Ramirez, B.D.Snow, 'UV written waveguide devices - Bragg gratings and applications in sensors', ICAMN 2007 Langkawi, Malaysia 29 May - 1 Jun 2007 (Invited)

M.F.R.Adikan, J.C.Gates, A.S.Webb, H.E.Major, **C. Holmes**, M.A.G.Ramirez, B.D.Snow, D.O.Kundys, C.B.E.Gawith, P.G.R.Smith, 'Recent developments in direct-UV-written planar waveguides, gratings, sensors and substrates', ECIO 2007, Copenhagen, 25-27 Apr 2007.

F.R.M.Adikan, A.S.Webb, R.J.Standish, J.K.Sahu, **C. Holmes**, H.E.Major, D.Kundys, J.C.Gates, C.B.E.Gawith, P.G.R.Smith, D.N.Payne, 'Sense and fibreility: Next generation optical biosensors', House of Commons Engineering Reception, (Poster) London 12 Dec 2006.

The following are titles of papers that are being drafted for publication, which stem from the work directly undertaken as part of this PhD thesis:

C. Holmes, J.C.Gates, P.G.R.Smith, 'Mapping the Stress Distribution in a Square Silica Membrane using Direct UV Written Planar Bragg Gratings', (2010)

C. Holmes, J.C.Gates, P.G.R.Smith, 'The Response of Direct UV written Planar Bragg Gratings in a Thin Silica Membrane to Differential Pressure', (2010)

Appendix B

FFT-BPM Algorithim

```
1 function ENDLOSS = MMI(Wavelength,Neff,Delta,UVthick,Period)
2 %The following is a function in which can be fed Wavelength, effective refractive
3 %index, index contrast, Thickness of UV written channel and period of MMI side walls

4 k0 = 2*pi/Wavelength;

5 % Fundamental Constants: permittivi of free space, the spped of light
6 epsilon0 = 8.85E-12; c = 3e8;

7 % MMI Device Paramters (Width, Length and Offset. Offset marks the location of the
8 % launch wavguide, i.e. 0.5 is a symmetric centre launch)
9 Wmmi=100E-6; Lmmi = 2.2*1e-3; Offset = 0.5; spotX = 2.5E-6;

10 % Modelling Paramters
11 StepSize = 0.1E-5; TransverseSamplesX = 2^ 12 ; XWidth = 6*Wmmi;
12 XStep = XWidth/(TransverseSamplesX-1); x = ((1:TransverseSamplesX)-1)*XStep - XWidth/2;
13 sx = mod( 1/2 + (0:(TransverseSamplesX-1))/TransverseSamplesX ,1 ) - 1/2; sx = sx*(2*pi/XStep);

14 % Refractive index
15 N = [No No+Delta]; Damped = 0.01;
16 IndexFUN = RefractiveIndex(Damped,length(x),x,UVthick,Wmmi,Offset,N,XWidth,Period);

17 % Precursors for Fourier loop
18 psi = exp( -(x.^ 2) / (spotX^ 2));
19 A = exp( (i.*StepSize.*sx.^ 2) ./ (2*no*k0));
20 Z(1) = 0; kk=1; tennor = 0;
```

```

21 % Fourier loops
22 for ii=1:floor(MMIdicelength/StepSize)
23     if (ii>1)
24         Z(ii) = Z(ii-1) + StepSize;
25     end
26     B = exp( (-i.* ( IndexFUN - n0 ) .*k0 ) .*StepSize);
27     psi = ifft( fft(psi) .* A ) .* B ;
28     tennor = tennor +1;
29     if tennor == tennorCapture
30         tennor=0;
31         XSection(kk,:) = abs((IndexFUN(1,DisplayBoxX1:DisplayBoxX2).*c.*epsilon0./2)...
32             .*psi(1,DisplayBoxX1:DisplayBoxX2)).^ 2;
33         NewZ(kk) = Z(:,ii);
34         [ending , rr] = size(XSection);
35         Remain = 100* IntegrateMatrix(XSection(ending,:),1,rr,StepSize)/...
36             IntegrateMatrix(XSection(1,:),1,rr,StepSize) ;
37         ENDLOSS=100-Remain;
38         Loss(kk) = ENDLOSS;
39         kk = kk+1;
40     end
41 end

42 % Crop and Plot
43 NewX = x(DisplayBoxX1:DisplayBoxX2); NewerZ = NewZ(Zdecapitate:NostepsZ); NewXSec-
tion = XSection(Zdecapitate:NostepsZ,:);
44 figure(1);surf(NewX*1e6, NewerZ*1e3,NewXSection,'edgecolor','none'); axis tight; view(90,90)

45 end

```

Appendix C

Kramers-Kronig Algorithm

restart;

The following algorithm converts extinction coefficient represented by a lorentzian curve to dispersion information

$p := \text{evalf}(\text{Pi})$; $c := 3e8$; These are the preliminary constants that need to be defined.

Variables defining the Lorentzian form of the extinction coefficient, in terms of wavelength.

$\text{wavFWHM} := 75e-9$;

$\text{wavcentred} := 1200e-9$;

$\text{extamplitude} := 1.6e-9$;

Converting variables to frequency domain

$\text{FWHM} := c^2 * p * ((1 / (\text{wavcentred} - (\text{wavFWHM} / 2))) - (1 / (\text{wavcentred} + (\text{wavFWHM} / 2))))$;

$\text{centred} := 2 * p * c / \text{wavcentred}$;

$\text{Lorencon} := (\text{FWHM}^2) * p * \text{extamplitude} / \text{wavcentred}$;

$\text{samplesz} := 350$;

$\text{sampleszPlus} := \text{samplesz} + 1$;

$\text{last} := 2 * p * c / 1000e-9$; $\text{begin} := 2 * p * c / 1600e-9$; $\text{change} := (\text{last} - \text{begin}) / \text{samplesz}$;

$i := 1$; $\text{dn} := \text{array}(1..\text{sampleszPlus}, 1..3)$; Precursor of matrix definition

Principle integral, Note constants are absent from the Lorentzian

for varx from begin by change to last do; $\text{integ} := \text{int}((1 / ((x - \text{centred})^2 + (\text{FWHM} / 2)^2)) * (x^2 - \text{varx}^2))$, $x=0, \text{infinity}$, 'CauchyPrincipalValue');

From calculated principle integral, the real part of the refractive index difference can be obtained.

$\text{dnreal} := \text{Lorencon} * \text{integ} * c / p$;

$\text{dnalpha} := (\text{Lorencon} / ((\text{varx} - \text{centred})^2 + (\text{FWHM} / 2)^2))$;

$\text{dn}[i,1] := \text{varx}$;

$\text{dn}[i,2] := \text{dnreal}$;

$\text{dn}[i,3] := \text{dnalpha}$;

```
i := i + 1;  
end do;
```

```
writedata('c:/maple data/X.txt',dn,float);  
plot( dn[ ((angFreq-begin+change)/change) ,3] , angFreq = begin..last) ;  
plot(dn[ ((angFreq-begin+change)/change) ,2] , angFreq = begin..last) ;
```

References

- [1] G. A. Thomas, B. I. Shraiman, P. F. Glodis, and M. J. Stephen. "Towards the clarity limit in optical fibre". *Nature*, 404(6775):262–264, 2000.
- [2] M. Svalgaard. "Effect of D₂ outdiffusion on direct UV writing of optical waveguides". *Electronics Letters*, 35(21):1840–1842, 1999.
- [3] G. M. Hale and M. R. Querry. "Optical Constants of Water in the 200-nm to 200-μm Wavelength Region". *Applied Optics*, 12(3):555–563, 1973.
- [4] F. Knappe, J. Voigt, H. Renner, and E. Brinkmeyer. "Direct UV writing of multimode-interference couplers". In *Bragg Gratings, Photosensitivity, and Poling in Glass Waveguides*, Technical Digest, page TuA4. Optical Society of America, 2003.
- [5] M. Marz. *Integrated Optics: Design and Modeling*. Artech House, 1994.
- [6] L. Eldada. "Advances in telecom and datacom optical components". *Optical Engineering*, 40(7):1165–1178, 2001.
- [7] E. D. Palik. *Handbook of Optical Constants of Solids*. New York : Academic, 1985.
- [8] S. E. Miller. "Integrated optics: an introduction". *Bell Syst. Tech. J.*, 48:205969, 1969.
- [9] G. D. Emmerson. *Novel Direct UV Written Devices*. PhD thesis, Southampton University, 2003.
- [10] I. J. G. Sparrow. *Development and Applications of UV Written Waveguide Structures*. PhD thesis, Southampton University, 2005.
- [11] L. Eldada. "Optical communication components". *Review of Scientific Instruments*, 75(3):575–593, 2004.
- [12] J. Aldred. *Iceland's energy answer comes naturally*. Guardian newspaper (online article www.guardian.co.uk), London, 2008.
- [13] J. E. Midwinter and Y. L. Guo. *Optoelectronics and lightwave technology*. Wiley, 1992.
- [14] T. Erdogan. "Fiber grating spectra". *Lightwave Technology, Journal of*, 15(8):1277–1294, 1997.
- [15] C. Riziotis and M. N. Zervas. "Performance comparison of Bragg grating-based optical add-drop multiplexers in WDM transmission systems". *Circuits, Devices and Systems, IEE Proceedings*, 149(3):179–186, 2002.

- [16] C. Nylander. "Chemical and biological sensors". *Journal of Physics E: Scientific Instruments*, (9):736, 1985.
- [17] R. Lucklum, C. Behling, and P. Hauptmann. "Role of Mass Accumulation and Viscoelastic Film Properties for the Response of Acoustic-Wave-Based Chemical Sensors". *Analytical Chemistry*, 71(13):2488–2496, 1999.
- [18] F. M. Battiston, J. P. Ramseyer, H. P. Lang, M. K. Baller, Ch Gerber, J. K. Gimzewski, E. Meyer, and H. J. Gntherodt. "A chemical sensor based on a microfabricated cantilever array with simultaneous resonance-frequency and bending readout". *Sensors and Actuators B: Chemical*, 77(1-2):122–131, 2001.
- [19] E. Bakker and M. Telting-Diaz. "Electrochemical Sensors". *Analytical Chemistry*, 74(12):2781–2800, 2002.
- [20] X. T. Zhou, J. Q. Hu, C. P. Li, D. Ma, C. S. Lee, and S. T. Lee. "Silicon nanowires as chemical sensors". *Chemical Physics Letters*, 369(1-2):220–224, 2003.
- [21] A. D. Kersey, M. A. Davis, H. J. Patrick, M. LeBlanc, K. P. Koo, C. G. Askins, M. A. Putnam, and E. J. Friebele. "Fiber grating sensors". *Lightwave Technology, Journal of*, 15(8):1442–1463, 1997.
- [22] P. V. Lambeck. "Integrated optical sensors for the chemical domain". *Measurement Science and Technology*, 17(8):R93–116, 2006.
- [23] S. Balslev, A. M. Jorgensen, B. Bilenberg, K. B. Mogensen, D. Snakenborg, O. Geschke, Kutter J. P., and A. Kristensen. "Lab-on-a-chip with integrated optical transducers". *Lab on a Chip*, 6:213–217, 2006.
- [24] R. Daw and J. Finkelstein. "Lab on a chip". *Nature*, 442(7101):367–367, 2006.
- [25] K. Kincade. "Fiber sensors lay groundwork for structural health monitoring". *Laser Focus World*, 42(2):63–67, Feb. 2006 2006.
- [26] X. Fan, I. White, S. Shopova, H. Zhu, J. Suter, and Y. Sun. "Sensitive optical biosensors for unlabeled targets: A review". *Analytica Chimica Acta*, 620(1-2):8–26, 2008.
- [27] K. Okamoto. *Fundamentals of Optical Waveguides*. Elsevier, 2nd edition, 2006.
- [28] K. Kawano and T. Kitoh. *Introduction to Optical Waveguide Analysis: Solving Maxwell's Equations and Schrodinger Equation*. John Wiley and Sons., 2001.
- [29] A. Ghatak and K. Thyagarajan. *Introduction to Fibre Optics*. Cambridge University Press, 2000.
- [30] S. O. Kasap. *Optoelectronics and Photonics: Principles and Practices*. Prentice Hall, New Jersey, 2001.
- [31] R. P. Feynman, R. B. Leighton, and M. Sands. *Feynman Lectures of Physics*, volume 2. Boni Samuel, 2005.
- [32] B. E. A. Saleh and M. C. Teich. *Fundamentals of Photonics*. John Wiley and Sons Inc., New York, 1991.

- [33] H. Nishihara, H. Masamitsu, and T. Suhara. *Optical Integrated Circuits*. McGraw-Hill, 1989.
- [34] J. Hu and C. R. Menyuk. "Understanding leaky modes: slab waveguide revisited". *Advances in Optics and Photonics*, 1(1):58–106, 2009.
- [35] N. S. Kapany and J. J. Burke. *Optical Waveguides*. Academic Press, New York, 1972.
- [36] P. Hammond and J. K. Sykulski. *Engineering Electromagnetism: Physical Process and Computation*. Oxford University Press, Oxford, 1999.
- [37] M.V.K Chari and S.J Salon. *Numerical Methods in Electromagnetism*. Academic Press, New York, 2000.
- [38] E. Schweig and W. B. Bridges. "Computer Analysis of Dielectric Waveguides: A Finite-Difference Method". *Microwave Theory and Techniques, IEEE Transactions on*, 32(5):531–541, 1984.
- [39] M. S. Stern. "Semivectorial polarised finite difference method for optical waveguides with arbitrary index profiles". *Optoelectronics, IEE Proceedings J*, 135(1):56–63, 1988.
- [40] K. Bierwirth, N. Schulz, and F. Arndt. "Finite-Difference Analysis of Rectangular Dielectric Waveguide Structures". *Microwave Theory and Techniques, IEEE Transactions on*, 34(11):1104–1114, 1986.
- [41] C. Yeh, S. B. Dong, and W. Oliver. "Arbitrarily Shaped Inhomogeneous Optical Fiber or Integrated Optical-Waveguides". *Journal of Applied Physics*, 46(5):2125–2129, 1975.
- [42] A. S. Sudbo. "Film mode matching: a versatile numerical method for vector mode field calculations in dielectric waveguides". *Pure and Applied Optics: Journal of the European Optical Society Part A*, (3):211, 1993.
- [43] A. S. Sudbo. "Numerically Stable Formulation of the Transverse Resonance Method for Vector Mode-Field Calculations in Dielectric Wave-Guides". *IEEE Photonics Technology Letters*, 5(3):342–344, 1993.
- [44] C. Kittel. *Introduction to Solid State Physics*. Wiley, 8th edition, 2004.
- [45] S. W. James and R. P. Tatam. "Optical fibre long-period grating sensors: Characteristics and application". *Measurement Science and Technology*, 14(5):R49–R61, 2003.
- [46] Y. J. Rao. "Recent progress in applications of in-fibre Bragg grating sensors". *Optics and Lasers in Engineering*, 31(4):297–324, 1999.
- [47] A. Yariv. *Optical Electronics*. Holt-Saunders, Japan, third edition, 1985.
- [48] M. Yamada and K. Sakuda. "Analysis of almost-periodic distributed feedback slab waveguides via a fundamental matrix approach". *Applied Optics*, 26(16):3474–3478, 1987.
- [49] A. Othonos and K. Kalli. *Fiber Bragg Gratings: Fundamentals and Applications in Telecommunications and Sensing*. Artech House Publishers, 1999.
- [50] R. A. Soref. "Silicon-based optoelectronics". *Proceedings of the IEEE*, 81(12):1687–1706, 1993.
- [51] Y. P. Li and C. H. Henry. "Silica-based optical integrated circuits". *IEE Proceedings-Optoelectronics*, 143(5):263–280, 1996.

- [52] A. Himeno, K. Kato, and T. Miya. "Silica-based planar lightwave circuits". *IEEE Journal of Selected Topics in Quantum Electronics*, 4(6):913–924, 1998.
- [53] M. R. Poulsen, P. I. Borel, J. Fage-Pedersen, J. Hubner, M. Kristensen, J. H. Povlsen, K. Rot-twitt, M. Svalgaard, and W. Svendsen. "Advances in silica-based integrated optics". *Optical Engineering*, 42(10):2821–2834, 2003.
- [54] S. P. Watts. *Flame Hydrolysis Deposition of Photosensitive Silicate Layers Suitable for the Definition of Waveguiding Structures through Direct Ultraviolet Writing*. PhD thesis, Southampton University, 2002.
- [55] M. Kawachi, M. Yasu, and T. Eda-iro. "Fabrication of SiO₂ TiO₂ glass planar optical waveguides by flame hydrolysis deposition". *Electronics Letters*, 19(15):583–584, 1983.
- [56] P. Tandon and H. Boek. "Experimental and theoretical studies of flame hydrolysis deposition process for making glasses for optical planar devices". *Journal of Non-Crystalline Solids*, 317(3):275–289, 2003.
- [57] M. Svalgaard. *Ultraviolet light induced refractive index structures in germanosilica*. PhD thesis, Technical University of Denmark, 1997.
- [58] R. F. Bunshah. "Critical issues in plasma-assisted vapor deposition processes". *Plasma Science, IEEE Transactions on*, 18(6):846–854, 1990.
- [59] G. Grand, J. P. Jadot, H. Denis, S. Valette, A. Fournier, and A. M. Grouillet. "Low-loss PECVD silica channel waveguides for optical communications". *Electronics Letters*, 26(25):2135–2137, 1990.
- [60] C. H. Henry, R. F. Kazarinov, H. J. Lee, K. J. Orlowsky, and L. E. Katz. "Low loss Si₃N₄-SiO₂ optical waveguides on Si". *Applied Optics*, 26(13):2621–2624, 1987.
- [61] M. V. Bazylenko, M. Gross, P. M. Allen, and P. L. Chu. "Fabrication of low-temperature PECVD channel waveguides with significantly improved loss in the 1.50-1.55 μm wavelength range". *Photonics Technology Letters, IEEE*, 7(7):774–776, 1995.
- [62] K. O. Hill, Y. Fujii, D. C. Johnson, and B. S. Kawasaki. "Photosensitivity in optical fiber waveguides: Application to reflection filter fabrication". *Applied Physics Letters*, 32(10):647–649, 1978.
- [63] B. S. Kawasaki, K. O. Hill, D. C. Johnson, and Y. Fujii. "Narrow-band Bragg reflectors in optical fibers". *Optics Letters*, 3(2):66–68, 1978.
- [64] D. K. W. Lam and B. K. Garside. "Characterization of single-mode optical fiber filters". *Applied Optics*, 20(3):440–445, 1981.
- [65] D. P. Hand and P. St J. Russell. "Photoinduced refractive-index changes in germanosilicate fibers". *Optics Letters*, 15(2):102, 1990.
- [66] G. Meltz, W. W. Morey, and W. H. Glenn. "Formation of Bragg gratings in optical fibers by a transverse holographic method". *Optics Letters*, 14(15):823–825, 1989.
- [67] M. Josephine Yuen. "Ultraviolet absorption studies of germanium silicate glasses". *Applied Optics*, 21(1):136–140, 1982.

- [68] R. Kashyap, G. D. Maxwell, and D. L. Williams. "Photoconduction in germanium and phosphorus doped silica waveguides". *Applied Physics Letters*, 62(3):214–216, 1993.
- [69] D. L. Williams, S. T. Davey, R. Kashyap, J. R. Armitage, and B. J. Ainslie. "Direct observation of UV induced bleaching of 240 nm absorption band in photosensitive germanosilicate glass fibres". *Electronics Letters*, 28(4):369–371, 1992.
- [70] T. E. Tsai and D. L. Griscom. "Defect centers and photoinduced self-organization in Ge-doped silica core fiber". volume 1516, pages 14–28. SPIE, 1991.
- [71] M. Douay, W. X. Xie, T. Taunay, P. Bernage, P. Niay, P. Cordier, B. Poumellec, L. Dong, J. F. Bayon, H. Poignant, and E. Delevaque. "Densification involved in the UV-based photosensitivity of silica glasses and optical fibers". *Lightwave Technology, Journal of*, 15(8):1329–1342, 1997.
- [72] A. Wootton, B. Thomas, and P. Harrowell. "Radiation-induced densification in amorphous silica: A computer simulation study". *The Journal of Chemical Physics*, 115(7):3336–3341, 2001.
- [73] L. Zheng, J. C. Lambropoulos, and A. W. Schmid. "UV-laser-induced densification of fused silica: a molecular dynamics study". *Journal of Non-Crystalline Solids*, 347(1-3):144–152, 2004.
- [74] P. J. Lemaire, R. M. Atkins, V. Mizrahi, and W. A. Reed. "High pressure H₂ loading as a technique for achieving ultrahigh UV photosensitivity and thermal sensitivity in GeO₂ doped optical fibres". *Electronics Letters*, 29(13):1191–1193, 1993.
- [75] J. Stone. "Interactions of hydrogen and deuterium with silica optical fibers: A review". *Lightwave Technology, Journal of*, 5(5):712–733, 1987.
- [76] P. J. Lemaire. "Reliability of optical fibers exposed to hydrogen: prediction of long-term loss increases". *Optical Engineering*, 30(6):780–789, 1991.
- [77] M. Svalgaard and M. Kristensen. "Directly UV written silica-on-silicon planar waveguides with low loss". *Electronics Letters*, 33(10):861–863, 1997.
- [78] K. M. Davis, K. Miura, N. Sugimoto, and K. Hirao. "Writing waveguides in glass with a femtosecond laser". *Optics Letters*, 21(21):1729–1731, 1996.
- [79] G. D. Marshall, M. Ams, and M. J. Withford. "Direct laser written waveguide-Bragg gratings in bulk fused silica". *Optics Letters*, 31(18):2690–2691, 2006.
- [80] S. Nolte, M. Will, J. Burghoff, and A. Tuennermann. "Femtosecond waveguide writing: a new avenue to three-dimensional integrated optics". *Applied Physics A: Materials Science and Processing*, 77(1):109, 2003.
- [81] G. D. Emmerson, S. P. Watts, C. B. E. Gawith, V. Albanis, M. Ibsen, R. B. Williams, and P. G. R. Smith. "Fabrication of directly UV-written channel waveguides with simultaneously defined integral Bragg gratings". *Electronics Letters*, 38(24):1531–1532, 2002.
- [82] G. D. Emmerson, C. B. E. Gawith, S. P. Watts, R. B. Williams, P. G. R. Smith, S. G. McMeekin, J. R. Bonar, and R. I. Laming. "All-UV-written integrated planar Bragg gratings and channel waveguides through single-step direct grating writing". *Optoelectronics, IEE Proceedings -*, 151(2):119–122, 2004.

- [83] C. R. Giles. "Lightwave applications of fiber Bragg gratings". *Lightwave Technology, Journal of*, 15(8):1391–1404, 1997.
- [84] H. Srensen, J. Canning, and M. Kristensen. "Thermal hypersensitisation and grating evolution in Ge-doped optical fibre". *Optics Express*, 13(7):2276–2281, 2005.
- [85] M. Lancry, P. Niay, and M. Douay. "Comparing the properties of various sensitization methods in H₂-loaded, UV hypersensitized or OH-flooded standard germanosilicate fibers". *Optics Express*, 13(11):4037–4043, 2005.
- [86] J. Canning, A. Canagasabey, and N. Groothoff. "Hypersensitisation of optical fibres with 355nm". In *Microwave and Optoelectronics Conference, 2003. IMOC 2003. Proceedings of the 2003 SBMO/IEEE MTT-S International*, volume 2, pages 973–976 vol.972, 2003.
- [87] M. Fokine and W. Margulis. "Large Increase in Photosensitivity through Massive Hydroxyl Formation". In *Bragg Gratings, Photosensitivity, and Poling in Glass Waveguides*, volume 33 of *OSA Trends in Optics and Photonics Series*, page CA4. Optical Society of America, 1999.
- [88] A. Canagasabey and J. Canning. "UV lamp hypersensitisation of hydrogen-loaded optical fibres". *Optics Express*, 11(13):1585–1589, 2003.
- [89] C. Riziotis, A. Fu, S. Watts, R. Williams, and P.G.R. Smith. "Rapid heat treatment for photosensitivity locking in deuterium-loaded planar optical waveguides". In *Bragg Gratings, Photosensitivity and Poling in Glass Waveguides (BGPP) 01*, 2001.
- [90] M Svalgaard. "Zero birefringence UV written optical waveguides". In *Bragg Gratings, Photosensitivity, and Poling in Glass Waveguides*, volume 33 of *OSA Trends in Optics and Photonics Series*, page CB3. Optical Society of America, 1999.
- [91] F. Baldini, A. N. Chester, J. Homola, and S. Martellucci. *Optical Chemical Sensors*. Springer, Dordrecht, 2004.
- [92] C. McDonagh, C. S. Burke, and B. D. MacCraith. "ChemInform Abstract: Optical Chemical Sensors". *ChemInform*, 39(18), 2008.
- [93] P. V. Lambeck, J. van Lith, and H. J. W. M. Hoekstra. "Three novel integrated optical sensing structures for the chemical domain". *Sensors and Actuators B: Chemical*, 113(2):718–729, 2006.
- [94] R. G. Heideman and P. V. Lambeck. "Remote opto-chemical sensing with extreme sensitivity: design, fabrication and performance of a pigtailed integrated optical phase-modulated Mach-Zehnder interferometer system". *Sensors and Actuators B: Chemical*, 61(1-3):100–127, 1999.
- [95] H. J. Patrick, A. D. Kersey, and F. Bucholtz. "Analysis of the Response of Long Period Fiber Gratings to External Index of Refraction". *Journal of Lightwave Technology*, 16(9):1606, 1998.
- [96] H. J. Patrick, G. M. Williams, A. D. Kersey, J. R. Pedrazzani, and A. M. Vengsarkar. "Hybrid fiber Bragg grating/long period fiber grating sensor for strain/temperature discrimination". *Photonics Technology Letters, IEEE*, 8(9):1223–1225, 1996.
- [97] J. Homola, S. S. Yee, and G. Gauglitz. "Surface plasmon resonance sensors: review". *Sensors and Actuators B: Chemical*, 54(1-2):3–15, 1999.

- [98] M. Piliarik and J. Homola. "Surface plasmon resonance (SPR) sensors: approaching their limits?". *Optics Express*, 17(19):16505–16517, 2009.
- [99] W. L. Barnes. "Surface plasmon-polariton length scales: a route to sub-wavelength optics". *Journal of Optics A: Pure and Applied Optics*, (4):S87, 2006.
- [100] G. Nemova and R. Kashyap. "Theoretical model of a planar integrated refractive index sensor based on surface plasmon-polariton excitation". *Optics Communications*, 275(1):76–82, 2007.
- [101] J.D. Jackson. *Classical Electrodynamics Third Edition*. Hamilton Printing Co., 1998.
- [102] L. Ward. *The Optical Constants of Bulk Materials and Films*. IOP Publishing Ltd, Bristol, second edition, 1994.
- [103] F. Wooten. *Optical Properties of Solids*. Academic Press, New York, 1972.
- [104] L. H. Donnell. *Beams, Plates and Shells*. McGraw-hill, New York, 1976.
- [105] G.W.C Kaye and T.H. Laby. *Tables of Physical and Chemical Constants*. Harlow Longman, 16th edition, 1995.
- [106] T. S. Narasimhamurty. *Photoelastic and Electrooptic Properties of Crystals*. Plenum, New York, 1981.
- [107] K. Vedam. "The Elastic and Photoelastic Constants of Fused Quartz". *Physical Review*, 78(4):472–473, 1950.
- [108] K. Schmitt, K. Oehse, G. Sulz, and C. Hoffmann. "Evanescent field Sensors Based on Tantalum Pentoxide Waveguides: A Review". *Sensors*, 8(2):711–738, 2008.
- [109] S. Mo and W. Y. Ching. "Electronic and optical properties of three phases of titanium dioxide: Rutile, anatase, and brookite". *Physical Review B*, 51(19):13023, 1995.
- [110] W. Wang and S. Chao. "Annealing effect on ion-beam-sputtered titanium dioxide film". *Optics Letters*, 23(18):1417–1419, 1998.
- [111] Z. Zhao, B. K. Tay, and G. Yu. "Room-Temperature Deposition of Amorphous Titanium Dioxide Thin Film with High Refractive Index by a Filtered Cathodic Vacuum Arc Technique". *Applied Optics*, 43(6):1281–1285, 2004.
- [112] L. Eldada, R. Blomquist, M. Maxfield, D. Pant, G. Boudoughian, C. Poga, and R. A. Norwood. "Thermooptic planar polymer Bragg grating OADM's with broad tuning range". *IEEE Photonics Technology Letters*, 11(4):448–450, 1999.
- [113] R. M. Measures, M. M. Ohn, S. Y. Huang, J. Bigue, and N. Y. Fan. "Tunable laser demodulation of various fiber Bragg grating sensing modalities". *Smart Materials and Structures*, (2):237, 1998.
- [114] Y. J. Rao. "In-fibre Bragg grating sensors". *Measurement Science and Technology*, 8(4):355–375, 1997.
- [115] S. Beeby, G. Ensell, M. Kraft, and N. White. *MEMS: Mechanical Sensors*. Artech House, Massachusetts, 2004.

- [116] P. V. Lambeck and H. Hoekstra. "Integrated optical sensors". In *Lasers and Electro-Optics Society, 2003. LEOS 2003. The 16th Annual Meeting of the IEEE*, volume 2, pages 967–968 vol.962, 2003.
- [117] T. A. Dawood, R. A. Sheno, and M. Sahin. "A procedure to embed fibre Bragg grating strain sensors into GFRP sandwich structures". *Composites Part A: Applied Science and Manufacturing*, 38(1):217–226, 2007.
- [118] Y. Okabe, S. Yashiro, R. Tsuji, T. Mizutani, and N. Takeda. "Effect of thermal residual stress on the reflection spectrum from fiber Bragg grating sensors embedded in CFRP laminates". *Composites Part A: Applied Science and Manufacturing*, 33(7):991–999, 2002.
- [119] C. Riziotis and M. N. Zervas. "Design Considerations in Optical Add/Drop Multiplexers Based on Grating-Assisted Null Couplers". *Journal of Lightwave Technology*, 19(1):92, 2001.
- [120] C. Riziotis and M. N. Zervas. "Novel Full-Cycle-Coupler-Based Optical Add-Drop Multiplexer and Performance Characteristics at 40-Gb/s WDM Networks". *Journal of Lightwave Technology*, 21(8):1828, 2003.
- [121] T. Chu, H. Yamada, S. Ishida, and Y. Arakawa. "Tunable optical add-drop multiplexer based on silicon photonic wire waveguides". In *Optical Fiber Communication Conference, 2006 and the 2006 National Fiber Optic Engineers Conference. OFC 2006*, pages 1409–1411, 2006.
- [122] W. C. Young and R. G. Budynas. *Roarks Formulas for Stress and Strain*. McGraw-Hill, seventh edition, 2005.
- [123] R. M. Jones. *Mechanics of Composite Materials*. Hemisphere Publishin Corporation, New York, 1975.
- [124] N. Maluf. *An Introduction to Microelectromechanical Systems Engineering*. Arctech, Boston, first edition, 2000.
- [125] J. R. Hook and H. E. Hall. *Solid State Physics*. The Manchester Physics Series. Wiley, second edition edition, 2000.
- [126] J. J. Wortman and R. A. Evans. "Young's Modulus, Shear Modulus, and Poisson's Ratio in Silicon and Germanium". *Journal of Applied Physics*, 36(1):153–156, 1965.
- [127] W. P. Mason. *Physical Acoustics and the Properties of Solids*. D Van Nostrand Company Inc., New Jersey, 1958.
- [128] R.M. Christensen. *Mechanics of Composite Materials*. Wiley, 1979.
- [129] S. Takahashi, J. Z. Hao, Y. W. A. Lee, Z. Cai, T. T. Do, and B. Y. R. Ng. "Effect of bending methods on FBG lateral force sensor". *Electronics Letters*, 41(23):1270–1271, 2005.
- [130] S. Magne, S. Rougeault, M. Vilela, and P. Ferdinand. "State-of-strain evaluation with fiber Bragg grating rosettes: application to discrimination between strain and temperature effects in fiber sensors". *Applied Optics*, 36(36):9437–9447, 1997.
- [131] C. Holmes, J. C. Gates, C. B. E. Gawith, and P. G. R. Smith. "Optical differential pressure transducer using planar Bragg gratings in an etched membrane". In *CLEO Europe - EQEC*, Munich, 2009.

- [132] C. Holmes, J. C. Gates, C. B. E. Gawith, and P. G. R. Smith. "Flow monitoring in optofluidic channels using planar Bragg gratings". In *CLEO IQEC*, Baltimore, 2009.
- [133] R. E. Oosterbroek, T. S. J. Lammerink, J. W. Berenschot, G. J. M. Krijnen, M. C. Elwenspoek, and A. van den Berg. "A micromachined pressure/flow-sensor". *Sensors and Actuators A: Physical*, 77(3):167–177, 1999.
- [134] R. E. Oosterbroek, T. S. J. Lammerink, J. W. Berenschot, A. van den Berg, and M. C. Elwenspoek. "Designing, realization and characterization of a novel capacitive pressure/flow sensor". In *Solid State Sensors and Actuators, 1997. TRANSDUCERS '97 Chicago., 1997 International Conference on*, volume 1, pages 151–154 vol.151, 1997.
- [135] P. Norlin, O. Ohman, B. Ekstrom, and L. Forssen. "A chemical micro analysis system for measurement of pressure, flow rate, temperature, conductivity, UV-absorption and fluorescence". In *Solid State Sensors and Actuators, 1997. TRANSDUCERS '97 Chicago., 1997 International Conference on*, volume 1, pages 507–510 vol.501, 1997.
- [136] M. J. Kohl, S. I. Abdel-Khalik, S. M. Jeter, and D. L. Sadowski. "A microfluidic experimental platform with internal pressure measurements". *Sensors and Actuators A: Physical*, 118(2):212–221, 2005.
- [137] J. Song and S. Lee. "Photonic microphone based on a dual-core multimode fiber head combined with a micromirror diaphragm". *Microwave and Optical Technology Letters*, 49(1):135–137, 2007.
- [138] M. Ohkawa, M. Hayashi, H. Nikkuni, N. Watanabe, and T. Sato. "Feasibility of a silicon-based guided-wave optical microphone". In *IPNRA*, Boston, 2008.
- [139] W. Lukosz and P. Pilska. "Integrated optical nanomechanical light modulators and microphones". *Sensors and Materials*, 3:261–280, 2008.
- [140] L. Mohanty, L. M. Koh, and S. C. Tjin. "Fiber Bragg grating microphone system". *Applied Physics Letters*, 89(16):161109, 2006.
- [141] K. Hosokawa and R. Maeda. "In-line pressure monitoring for microfluidic devices using a deformable diffraction grating". In *Micro Electro Mechanical Systems, 2001. MEMS 2001. The 14th IEEE International Conference on*, pages 174–177, 2001.
- [142] C. W. Wong, Y. Jeon, G. Barbastathis, and S. Kim. "Analog tunable gratings driven by thin-film piezoelectric microelectromechanical actuators". *Applied Optics*, 42(4):621–626, 2003.
- [143] H. Sheng, W. F. Liu, K. Lin, S. Bor, and M. Fu. "High-sensitivity temperature-independent differential pressure sensor using fiber Bragg gratings". *Optics Express*, 16(20):16013–16018, 2008.
- [144] W. Zhang, F. Li, and Y. Liu. "Fiber Bragg grating pressure sensor with ultrahigh sensitivity and reduced temperature sensitivity". *Optical Engineering*, 48(2):024402, 2009.
- [145] S. P. Timoshenko. *Theory of Elastic Stability*. McGraw-Hill, New York and London, first edition, 1936.

- [146] D. S. Popescu, T. S. J. Lammerink, and M. Elwenspoek. "Buckled membranes for microstructures". In *Micro Electro Mechanical Systems, 1994, MEMS '94, Proceedings, IEEE Workshop on*, pages 188–192, 1994.
- [147] D. S. Popescu, D. C. Dascalu, M. Elwenspoek, and T. Lammerink. "Silicon Active Microvalves Using Buckled Membranes For Actuation". In *Solid-State Sensors and Actuators, 1995 and Eurosensors IX.. Transducers '95. The 8th International Conference on*, volume 2, pages 305–308, 1995.
- [148] L. Eckertova. *Physics of Thin Films*. Plenum, second edition, 1986.
- [149] K. Iga and Y. Kokubun. *Encyclopedia of Integrated Optics*. Taylor and Francis, Boca Raton, 2006.
- [150] F. Bilodeau, D. C. Johnson, S. Theriault, B. Malo, J. Albert, and K. O. Hill. "An all-fiber dense wavelength-division multiplexer/demultiplexer using photoimprinted Bragg gratings". *Photonics Technology Letters, IEEE*, 7(4):388–390, 1995.
- [151] T. Watanabe, T. Goh, M. Okuno, S. Sohma, T. Shibata, M. Itoh, M. Kobayashi, M. Ishii, A. Sugita, and Y. Hibino. "Silica-based PLC 1x128 thermo-optic switch". In *Optical Communication, 2001. ECOC '01. 27th European Conference on*, volume 2, pages 134–135 vol.132, 2001.
- [152] S. Honda, Z. Wu, J. Matsui, K. Utaoka, T. Eura, M. Tokuda, K. Tsutsui, and Y. Wada. "Largely-tunable wideband Bragg gratings fabricated on SOI rib waveguides employed by deep-RIE". *Electronics Letters*, 43(11):630–631, 2007.
- [153] S. Homampour, M. P. Bulk, P. E. Jessop, and A. P. Knights. "Thermal tuning of planar Bragg gratings in silicon-on-insulator rib waveguides". *physica status solidi (c)*, 6(S1):S240–S243, 2009.
- [154] A. Othonos. "Fibre Bragg gratings". *Rev. Sci. Instrum.*, 68(12):4309–4341, 1997.
- [155] K. Okamoto. "Recent progress of integrated optics planar lightwave circuits". *Optical and Quantum Electronics*, 31(2):107–129, 1999.
- [156] R. Kasahara, M. Yanagisawa, A. Sugita, T. Goh, M. Yasu, A. Himeno, and S. Matsui. "Low-power consumption silica-based 2x2 thermooptic switch using trenched silicon substrate". *Photonics Technology Letters, IEEE*, 11(9):1132–1134, 1999.
- [157] L. B. Soldano and E. C. M. Pennings. "Optical multi-mode interference devices based on self-imaging: principles and applications". *Lightwave Technology, Journal of*, 13(4):615–627, 1995.
- [158] J. Porque, P. Coudray, R. Charters, K. Kribich, P. Etienne, and Y. Moreau. "WDM based on multimode interference-coupler built in an organic-inorganic material". *Optics Communications*, 183(1-4):45–49, 2000.
- [159] F. R. Mahamd Adikan, J. C. Gates, C. B. E. Gawith, and P. G. R. Smith. "Quantitative Determination of Photosensitivity Proximity Effects in Multi Exposure Direct UV Writing for High Density Integrated Optics". In *CLEO/Europe and IQEC 2007 Conference Digest*, pages CE4–3. Optical Society of America, 2007.

- [160] R. Bernini, E. De Nuccio, A. Minardo, L. Zeni, and P. M. Sarro. "2D MMI devices based on integrated hollow ARROW waveguides". *Selected Topics in Quantum Electronics, IEEE Journal of*, 13(2):194–201, 2007.
- [161] R. Ulrich and G. Ankele. "Self-imaging in homogeneous planar optical waveguides". *Applied Physics Letters*, 27(6):337–339, 1975.
- [162] M. A. Duguay, Y. Kokubun, T. L. Koch, and Pfeiffer Loren. "Antiresonant reflecting optical waveguides in SiO₂-Si multilayer structures". *Applied Physics Letters*, 49(1):13–15, 1986.
- [163] H. Kim, I. Park, B. O. S. Park, E. Lee, and S. M. Lee. "Self-imaging phenomena in multi-mode photonic crystal line-defect waveguides: application to wavelength de-multiplexing". *Optics Express*, 12(23):5625–5633, 2004.
- [164] H. Schmidt and A. R. Hawkins. "Optofluidic waveguides: I. Concepts and implementations". *Microfluidics and Nanofluidics*, 4(1-2):3–16, 2008.
- [165] J. L. Archambault, R. J. Black, S. Lacroix, and J. Bures. "Loss calculations for antiresonant waveguides". *Journal Lightwave Technology*, 11:416423, 1993.
- [166] C. Lagarias Jeffrey, A. Reeds James, H. Wright Margaret, and E. Wright Paul. "Convergence Properties of the Nelder–Mead Simplex Method in Low Dimensions". *SIAM J. on Optimization*, 9(1):112–147, 1998.
- [167] N. V. Lavrik. "Cantilever transducers as a platform for chemical and biological sensors". *Review of Scientific Instruments*, 75(7):2229–2253, 2004.